Bifurcations in Kolmogorov and Taylor-Vortex Flows

Philip Love

CRPC-TR99807-S
September 1999

Center for Research on Parallel Computation
Rice University
6100 South Main Street
CRPC - MS 41
Houston, TX 77005

Submitted November 1999

Bifurcations in Kolmogorov and Taylor-Vortex Flows

Thesis by

Philip Love

In Partial Fulfillment of the Requirements

for the Degree of

Doctor of Philosophy

California Institute of Technology

Pasadena, California

1999

(Submitted September 2, 1998)

© 1999
Philip Love
All Rights Reserved

Acknowledgements

I would like to take this opportunity to thank my advisor Herb Keller, for all his guidance during my time here at Caltech. I also wish to thank Professor Saffman and Dale Pullin for their insight into the fluid dynamics of the numerical results that I obtained. Additionally I would like to thank Sebius Doedel for helping me to understand how to use his AUTO code.

I also want to thank my friends Paul LeMahieu, Vincent Bohossian, Mark Meloon and Heather Lawless for making the years at Caltech enjoyable.

Additionally I would like to thank my parents, and my brother Martin, for all their support through my many years at University.

Lastly, thanks to my friends in the United Kingdom: Matt Stewart, Nick Craig, Brett Taylor, Simon Cox, and Pam Westgate.

Also I wish to thank the CRPC for funding this research.

Abstract

The bifurcation structure of Kolmogorov and Taylor-Vortex flows was computed with the aid of the Recursive Projection Method; see Schroff and Keller [32]. It was shown that RPM significantly improves the convergence of our numerical method while calculating steady state solutions. Moreover we use RPM to detect bifurcation points while continuing along solution branches, and to provide the required augmentation when continuing around a fold, or along a travelling wave branch.

The bifurcations to two and three-dimensional solutions from the shear flow solution of Kolmogorov flow are calculated both numerically, by solving an ordinary differential equation, and analytically, using an approximation method. Our results for the two-dimensional bifurcations agree with the work of Meshalkin and Sinai [26].

We also explain how the branches of Kolmogorov flows observed by Platt and Sirovich [29] are connected together, and observe that our solutions have worm like structures even at relatively low Reynolds numbers. Various statistics of our flows are calculated and compare with those from isotropic trubulence calculations.

Additionally various solution branches of the Taylor Vortex flow were computed, including spiral vortices. Furthermore, it was discovered that the Wavy Taylor Vortex branches arise from sub-critical Hopf bifurcations, and they undergo a fold close to their bifurcation point.

Contents

List of Figures

List of Tables

Chapter 1 Introduction

The objective of his research is to study in detail some of the bifurcations that occur in Kolmogorov and Taylor-Vortex flows. As the Reynolds number is increased we show the different flows that occur to aid in the understanding of how stable flows become turbulent.

Naturally occuring turbulent flows, like jets and mixing layers, are typically anisotropic; however, most theoretical turbulence work has concentrated on isotropic flows. Kolmogorov flow was initially introduced as a simple example of a linear stability problem. We define Kolmogorov flow to be any steady-state, periodic or quasi-periodic solution of the incompressible Navier-Stokes equations with the forcing suggested by Kolmogorov, see equation (2.1). Meshalkin and Sinai [26] analytically found the locations of the two-dimensional bifurcations from the shear flow solution of Kolmogorov flow using a continued fractions approach. This result was also obtained by Green [17]. Later we find both the two and three-dimensional bifurcations using an approximation method. Additionally we check our results by numerically solving the linear stability problem.

It is shown that the wavelength in the x-direction of an unstable mode is greater than the wavelength of the forcing. Yakhot and Sivashinsky [36] showed that the instability of a flow to long-wavelength disturbances may be interpreted in terms of a negative effective viscosity of the corresponding large-scale flow.

The long-wavelength instability has also been analyzed by Libin and Sivashinsky [22] for a more general variant of Kolmogorov flow called Arnold-Beltrami-Childress (ABC) flow. They show that for a certain class of long-wave, perturbations the ABC flow is always unstable.

A brief overview of the work of related to Kolmogorov flow was given by Arnold [3]. Arnold mentions that in a finite parameter region it has been proved, for the two-dimensional case, that there cannot be an infinite number of bifurcations. It is believed that this result is also true for the three-dimensional case. However experiments are unable to establish whether observed turbulent solutions have a large finite number of modes or an infinite number of modes.

As the Reynolds number of these flows is increased, we observe numerous bifurcations.

When the Reynolds number is sufficiently large, the flow is in a turbulent state. We believe that the transition from the shear flow to turbulent flow is due to the many bifurcations that exist. Platt et al. [29] computed various different Kolmogorov flows; however, they did not explain how one flow bifurcates from another.

An intriguing problem of hydrodynamic turbulence is the presence of large scale structures in a fluid that is turbulent at small scales. These large scale structure where observed by Platt et al. [29]; however, they do not explain how they originate.

Kolmogorov flow has been studied numerically at high Reynolds numbers by Borue and Orszag [7]. To achieve high Reynolds numbers they replace the normal Laplacian viscosity term with the hyperviscosity term $(-1)^{h+1}\Delta^h$. This gives the solution a larger inertial range, enabling them to show that the energy spectrum obeys Kolmogorov's 5/3 scaling law. Additionally they demostrate that the anisotropic large-scale flow may be considered locally isotropic at scales approximately ten time smaller than the scale of the flow.

Extensive calculations of isotropic turbulent flow have been performed by Jiménez et al. [18]. They compute various distribution and probability density functions of flow properies, such as velocity gradients, stress and strain.

Many previous numerical and experimental studies have concentrated on Taylor-Vortex Flow. From experimental work we know that when the outer cylinder is stationary, the flow bifurcates from Couette flow to Vortex flow, through wavy vortex flow to modulated vortex flow. A diagram showing the stability regions of the various types of flows can be found in Andereck, Liu and Swinney [1]. Interesting flows, such as spiral vortices, occur when the cylinders are counter-rotating, while for co-rotating flows, twists have been observed.

An important study of wavy vortex flow was the experimental work by Coles [9], in which he showed the transition between wavy Taylor vortices of different azimuthal and axial wavenumbers. Additionally he found a hysteresis loop in which the axial wavelength remains constant while the number of waves around the cylinder changes.

Meyer-Spasche and Keller [27], and Dinar and Keller [11], numerically studied how changing the aspect ratio effected the location of the bifurcation points from Taylor-Couette flow to Taylor-Vortex flow. Additionally Meyer-Spasche and Keller examined the solutions around the point where two branches of solutions of different wavenumbers bifurcated from the same point. In this case they found additional branches with flow patterns different from the usual Taylor-Vortex flow configuration.

Most numerical work has focused on using periodic boundary conditions in the axial direction; however, Dinar and Keller studied Taylor-vortex flow on finite length cylinders for which they found anomalous mode solutions. These are solutions which have an odd number of vortices or additional small vortices adjacent to the end plates.

Numerical results have often concentrated on determining the wave speed of the Wavy Taylor Vortices, and how this speed varies as the Reynolds number and aspect ratios are altered. As noted by Marcus [25] the wave speed is sensitive to numerical inaccuracies. We show later that our computed wavespeeds agree with those computed by King et al. [20], and Schröder and Keller [30]. Additionally we show that the eigenvalues at the Hopf bifurcation point give an accurate prediction of the wavespeed on the bifurcating branch, and we study the behaviour of the wavy Taylor vortex flows near their bifurcation points.

Spiral vortices have been observed in experiments for counter-rotating cylinders, by Andereck et al. [1], but they are unstable when the outer cylinder is stationary. They have been computed in this case by Moulic and Yao [28], who also find that these flows have a net mass of fluid moving in the axial direction.

In computing these solutions we make extensive use of the Recursive Projection Method, see Schroff and Keller [32], to accelerate the convergence and to detect bifurcation points. The idea of RPM is to accelerate the convergence of a fixed point iteration by using Newton's method on the unstable and slowly convergent subspace. Although RPM can maintain the convergence of any fixed point itertion it is important, for efficiency reasons, to use an iteration with a small unstable subspace, and well seperated eigenvalues.

Davidson [10] suggested preconditioning the RPM iteration to improve the performance; however, the same result can be achieved by using a better numerical method to which RPM is applied.

The Recursive Projection Method was also used effectively by Keller and Von Sosen [19] to aid in the convergence of Taylor-Vortex solutions. We extend this research to higher resolution three-dimensional calculations. In particular we are interested in how the performance of RPM is effected by higher resolution calculations. Also we use RPM to detect bifucation points during numerically continuation. This inherent bifurcation detection property allows us to cheaply estimate the eigenvalues of the Jacobian during continuation, whereas when other iterative method extensive additional calculations are normally required.

Variants of the Recursive Projection Method have been proposed by Lust et al. [24],

and Lust and Roose [23]. Instead of thinking of RPM as a way to stabilize a fixed point iteration, they derive it by using a Picard iteration to approximate Newton's method. This approach allows them to derive Gauss-Seidel style variants which have better convergence properties. However, they do not explain how to determine the unstable subspace for their methods.

Chapter 2 Kolmogorov Flow

2.1 Derivation of Equations

The dimensional incompressible Navier-Stokes equations with the specific forcing, of strength χ, suggested by Kolmogorov are:

$$\begin{aligned} \frac{\partial \mathbf{u}'}{\partial t'} + \mathbf{u}'.\nabla'\mathbf{u}' &= -\frac{\nabla' p'}{\rho} + \nu \nabla'^2 \mathbf{u}' + \chi \sin(ky')\mathbf{e}_{x'}, \\ \nabla'.\mathbf{u}' &= 0 \end{aligned} \tag{2.1}$$

Solutions of these equations subject to periodic boundary conditions on a box are known as Kolmogorov flows. We consider these equations on a domain of length L in the x direction, M in the y direction, and N in the z direction. Since the flow is defined to be periodic it is necessary that $k = 2\pi m/M$, where $m \in \mathbb{N}$.

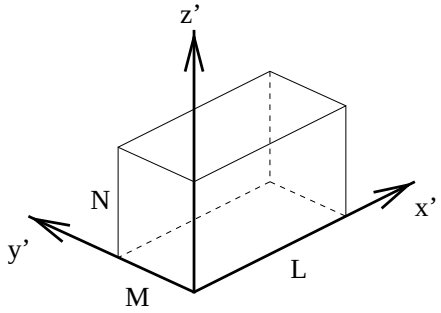

Figure 2.1: Domain of the Dimensional Equations for Kolmogorov Flow

An exact steady state solution of this system is the shear flow:

$$\mathbf{u}' = \frac{\chi}{\nu k^2} \sin(ky')\mathbf{e}_{x'}, \qquad p' = const. \tag{2.2}$$

Our formulation of the non-dimensionalized equations is the same as used by Platt and Sirovich [29]. We define a Reynolds Number for this system by using the maximum speed of the shear flow $\chi/(\nu k^2)$, and k^{-1} as a length scale, so that $Re = \frac{\chi}{\nu^2 k^3}$.

To obtain the non-dimensionalized Navier-Stokes equations, we use following scalings, for any arbitrary $c > 0$:

$$\begin{aligned} x &= \frac{x'c}{L}, & y &= \frac{y'c}{M}, & z &= \frac{z'c}{N}, \\ t &= \frac{t'\chi c}{\nu k^2 M}, & \mathbf{u} &= \frac{\mathbf{u}'\nu k^2}{\chi}, & p &= \frac{p'\nu^2 k^4}{\rho\chi^2}, \\ Re &= \frac{\chi}{\nu^2 k^3}, & n &= \frac{Mk}{c}, & \Omega &= nRe. \end{aligned} \tag{2.3}$$

To simplify the non-dimensionalized momentum equations, we introduce two aspect ratios $A = M/L$ and $B = M/N$. This yields the x-momentum equation:

$$\frac{\partial u}{\partial t} + Au\frac{\partial u}{\partial x} + v\frac{\partial u}{\partial y} + Bw\frac{\partial u}{\partial z} = -A\frac{\partial p}{\partial x} + \frac{1}{\Omega}\left(A^2\frac{\partial^2 u}{\partial x^2} + \frac{\partial^2 u}{\partial y^2} + B^2\frac{\partial^2 u}{\partial z^2}\right) + \frac{n^2}{\Omega}\sin(ny). \tag{2.4}$$

Similarly the y and z-momentum equations become

$$\frac{\partial v}{\partial t} + Au\frac{\partial v}{\partial x} + v\frac{\partial v}{\partial y} + Bw\frac{\partial v}{\partial z} = -\frac{\partial p}{\partial y} + \frac{1}{\Omega}\left(A^2\frac{\partial^2 v}{\partial x^2} + \frac{\partial^2 v}{\partial y^2} + B^2\frac{\partial^2 v}{\partial z^2}\right), \tag{2.5}$$

$$\frac{\partial w}{\partial t} + Au\frac{\partial w}{\partial x} + v\frac{\partial w}{\partial y} + Bw\frac{\partial w}{\partial z} = -B\frac{\partial p}{\partial z} + \frac{1}{\Omega}\left(A^2\frac{\partial^2 w}{\partial x^2} + \frac{\partial^2 w}{\partial y^2} + B^2\frac{\partial^2 w}{\partial z^2}\right); \tag{2.6}$$

and the continuity equation becomes

$$A\frac{\partial u}{\partial x} + \frac{\partial v}{\partial y} + B\frac{\partial w}{\partial z} = 0. \tag{2.7}$$

In this thesis we study both the steady state and time periodic solutions of the system (2.4)-(2.7). This system has the following steady state shear flow solutions, for arbitrary choices of u_0,v_0,w_0, and p_0:

$$\begin{aligned} u &= u_c\cos(ny) + u_s\sin(ny) + u_0, \\ v &= v_0, \qquad w = w_0, \qquad p = p_0. \end{aligned} \tag{2.8}$$

The scalars u_c and u_s are obtained by using the above in (2.4) to get

$$u_c = \frac{nv_0\Omega}{v_0^2\Omega^2 + n^2}, \qquad u_s = \frac{n^2}{v_0^2\Omega^2 + n^2}. \tag{2.9}$$

We choose to study Kolmogorov flow in a frame of reference that has no net flow:

$$\iiint_{BOX} u(x,y,z)dxdydz = 0, \quad \iiint_{BOX} v(x,y,z)dxdydz = 0, \quad \iiint_{BOX} w(x,y,z)dxdydz = 0. \tag{2.10}$$

Here BOX is the periodic domain: $0 \leq x, y, z \leq 2\pi$. This implies that in the shear flow $u_0, v_0, w_0 \equiv 0$. Additionally we choose the mean pressure to be equal zero.

We now show that the momentum equations do not impose a forcing that causes a net flow. Hence if the initial condition has no net flow of fluid, then there will be no net flow at any future time.

We consider the conservation form of the Navier-Stokes equations, and define

$$\begin{aligned} F^c(u,v,w,p) \equiv & \frac{1}{\Omega}\left(A^2\frac{\partial^2 u}{\partial x^2} + \frac{\partial^2 u}{\partial y^2} + B^2\frac{\partial^2 u}{\partial z^2}\right) + \frac{n^2}{\Omega}\sin(ny) \\ & - A\frac{\partial}{\partial x}(u^2) - \frac{\partial}{\partial y}(uv) - B\frac{\partial}{\partial z}(uw) - A\frac{\partial p}{\partial x}, \end{aligned} \tag{2.11}$$

$$G^c(u,v,w,p) \equiv \frac{1}{\Omega}\left(A^2\frac{\partial^2 v}{\partial x^2} + \frac{\partial^2 v}{\partial y^2} + B^2\frac{\partial^2 v}{\partial z^2}\right) - A\frac{\partial}{\partial x}(uv) - \frac{\partial}{\partial y}(v^2) - B\frac{\partial}{\partial z}(vw) - \frac{\partial p}{\partial y}, \tag{2.12}$$

$$H^c(u,v,w,p) \equiv \frac{1}{\Omega}\left(A^2\frac{\partial^2 w}{\partial x^2} + \frac{\partial^2 w}{\partial y^2} + B^2\frac{\partial^2 w}{\partial z^2}\right) - A\frac{\partial}{\partial x}(uw) - \frac{\partial}{\partial y}(vw) - B\frac{\partial}{\partial z}(w^2) - B\frac{\partial p}{\partial z}. \tag{2.13}$$

These functions are defined on a Hilbert space, $\mathbb{H}$ of 2π periodic smooth functions with the standard inner product.

Theorem 2.1 *Given $u, v, w, p \in \mathbb{H}$ which satisfy the continuity equation, we have*

$$\iiint_{BOX} F^c(u,v,w,p)dxdydz = 0, \tag{2.14}$$

$$\iiint_{BOX} G^c(u,v,w,p)dxdydz = 0, \tag{2.15}$$

$$\iiint_{BOX} H^c(u,v,w,p)dxdydz = 0. \tag{2.16}$$

Proof: We note that the terms in functions F^c, G^c, and H^c are derivatives, except for the $\sin(ny)$ term. It is easily shown that:

$$\iiint_{BOX} \sin(ny)dxdydz = 0. \tag{2.17}$$

Given any 2π periodic function $f(x)$, we have that

$$\int_0^{2\pi} \frac{df}{dx}dx = 0. \tag{2.18}$$

Consider the term $\frac{\partial}{\partial x}(u^2)$. Integrating over the y and z directions gives a function, say $g(x)$, that is periodic in the x direction.

$$g(x) \equiv \int_0^{2\pi}\int_0^{2\pi} \frac{\partial}{\partial x}(u^2)dydz. \tag{2.19}$$

Hence the integration of $\frac{\partial}{\partial x}(u^2)$ over the entire cube is equal to zero. The same argument applies to the other terms with x derivatives. Similar arguments give the results for the terms with y and z derivatives.

□

2.2 Bifurcations from Shear Flow

The "first" bifurcation from the shear flow was evaluated by Meshalkin and Sinai [26] for the two-dimensional case of an infinite plane. We determine the bifurcations from the shear flow on a periodic cube rather than an infinite plane. A major difference is in the evaluation of the bifurcation curves; whereas Meshalkin and Sinai use continued fractions we require that a sequence of minors of an infinite matrix be singular to get a sequence of approximations to the bifurcation points. We solve the minors computationally to obtain a curve of bifurcation points. Additionally we solve an ordinary differential equation numerically to get an independent check on the approximation method.

2.2.1 Derivation of Linearized Equations

To determine the possible bifurcations points from the shear flow $u = \sin(ny)$, $v = 0$, $w = 0$, and $p = 0$, we examine the steady state linearized problem about this flow and find

the parameter values for which this system is singular (i.e., has nontrivial solutions.) The linearized equations are

$$A\sin(ny)\frac{\partial \tilde{u}}{\partial x} + \tilde{v}n\cos(ny) = -A\frac{\partial \tilde{p}}{\partial x} + \frac{1}{\Omega}\left(A^2\frac{\partial^2 \tilde{u}}{\partial x^2} + \frac{\partial^2 \tilde{u}}{\partial y^2} + B^2\frac{\partial^2 \tilde{u}}{\partial z^2}\right), \tag{2.20}$$

$$A\sin(ny)\frac{\partial \tilde{v}}{\partial x} = -\frac{\partial \tilde{p}}{\partial y} + \frac{1}{\Omega}\left(A^2\frac{\partial^2 \tilde{v}}{\partial x^2} + \frac{\partial^2 \tilde{v}}{\partial y^2} + B^2\frac{\partial^2 \tilde{v}}{\partial z^2}\right), \tag{2.21}$$

$$A\sin(ny)\frac{\partial \tilde{w}}{\partial x} = -B\frac{\partial \tilde{p}}{\partial z} + \frac{1}{\Omega}\left(A^2\frac{\partial^2 \tilde{w}}{\partial x^2} + \frac{\partial^2 \tilde{w}}{\partial y^2} + B^2\frac{\partial^2 \tilde{w}}{\partial z^2}\right), \tag{2.22}$$

$$A\frac{\partial \tilde{u}}{\partial x} + \frac{\partial \tilde{v}}{\partial y} + B\frac{\partial \tilde{w}}{\partial z} = 0. \tag{2.23}$$

To carry out the analysis, we reduce the above system to a single partial differential equation. Later we assume a particular form of the solution to further reduce it to an ordinary differential equation.

The first stage is to eliminate the pressure terms from (2.20) and (2.21) by cross differentiation to get

$$\begin{aligned} &An\cos(ny)\frac{\partial \tilde{u}}{\partial x} + A\sin(ny)\frac{\partial^2 \tilde{u}}{\partial x \partial y} + \frac{\partial \tilde{v}}{\partial y}n\cos(ny) - \tilde{v}n^2\sin(ny) - A^2\sin(ny)\frac{\partial^2 \tilde{v}}{\partial x^2} \\ &\quad = \frac{1}{\Omega}\left(A^2\frac{\partial^3 \tilde{u}}{\partial x^2 \partial y} + \frac{\partial^3 \tilde{u}}{\partial y^3} + B^2\frac{\partial^3 \tilde{u}}{\partial y \partial z^2} - A^3\frac{\partial^3 \tilde{v}}{\partial x^3} - A\frac{\partial^3 \tilde{v}}{\partial x \partial y^2} - AB^2\frac{\partial^3 \tilde{v}}{\partial x \partial z^2}\right). \end{aligned} \tag{2.24}$$

We now differentiate with respect to x, multiply by A, and use the linearized continuity equation (2.23) to eliminate $\tilde{u}$. After simplification we get

$$\begin{aligned} &A\sin(ny)\left(A^2\frac{\partial^3 \tilde{v}}{\partial x^3} + \frac{\partial^3 \tilde{v}}{\partial x \partial y^2} + n^2\frac{\partial \tilde{v}}{\partial x}\right) + ABn\cos(ny)\frac{\partial^2 \tilde{w}}{\partial x \partial z} + AB\sin(ny)\frac{\partial^3 \tilde{w}}{\partial x \partial y \partial z} \\ &= \frac{1}{\Omega}\left(A^2\frac{\partial^2}{\partial x^2} + \frac{\partial^2}{\partial y^2}\right)\left(A^2\frac{\partial^2}{\partial x^2} + \frac{\partial^2}{\partial y^2} + B^2\frac{\partial^2}{\partial z^2}\right)\tilde{v} + \frac{B}{\Omega}\frac{\partial^2}{\partial y \partial z}\left(A^2\frac{\partial^2}{\partial x^2} + \frac{\partial^2}{\partial y^2} + B^2\frac{\partial^2}{\partial z^2}\right)\tilde{w}. \end{aligned} \tag{2.25}$$

Similarly we eliminate the pressure terms from (2.21) and (2.22) to get

$$\begin{aligned} &AB^2\sin(ny)\frac{\partial^2 \tilde{v}}{\partial x \partial z^2} - AB\sin(ny)\frac{\partial^2 \tilde{w}}{\partial x \partial y \partial z} - ABn\cos(ny)\frac{\partial^2 \tilde{w}}{\partial x \partial z} \\ &\quad = \frac{B^2}{\Omega}\frac{\partial^2}{\partial z^2}\left(A^2\frac{\partial^2}{\partial x^2} + \frac{\partial^2}{\partial y^2} + B^2\frac{\partial^2}{\partial z^2}\right)\tilde{v} - \frac{B}{\Omega}\frac{\partial^2}{\partial y \partial z}\left(A^2\frac{\partial^2}{\partial x^2} + \frac{\partial^2}{\partial y^2} + B^2\frac{\partial^2}{\partial z^2}\right)\tilde{w}. \end{aligned} \tag{2.26}$$

Finally we add (2.25) and (2.26) to get the linearized equation for $\tilde{v}$:

$$A\sin(ny)\left(A^2\frac{\partial^3\tilde{v}}{\partial x^3}+\frac{\partial^3\tilde{v}}{\partial x\partial y^2}+B^2\frac{\partial^3\tilde{v}}{\partial x\partial z^2}+n^2\frac{\partial\tilde{v}}{\partial x}\right)=\frac{1}{\Omega}\left(A^2\frac{\partial^2}{\partial x^2}+\frac{\partial^2}{\partial y^2}+B^2\frac{\partial^2}{\partial z^2}\right)^2\tilde{v}. \tag{2.27}$$

Given the above partial differential equation, we approximate $\tilde{v}(x,y,z)$ by using the assumption that the periodicity in the x and z directions is of a simple form, specifically $\tilde{v}(x,y,z)=e^{irx}e^{isz}\tilde{V}(y)$. We set $\alpha\equiv Ar$ and $\beta\equiv Bs$, which reduces (2.27) to

$$i\alpha\sin(ny)\left(\frac{d^2\tilde{V}}{dy^2}+[n^2-\alpha^2-\beta^2]\tilde{V}\right)=\frac{1}{\Omega}\left(\frac{d^2}{dy^2}-[\alpha^2+\beta^2]\right)^2\tilde{V}. \tag{2.28}$$

Now we use this ordinary differential equation both numerically and analytically to get the curve of bifurcation points from shear flow.

2.2.2 Numerical Calculation

To determine the bifurcation curves numerically we use the AUTO package by Doedel, which requires that we formulate our ordinary differential equation as an autonomous first order system of ordinary differential equations. Furthermore, since AUTO calculates the solution to ordinary differential equations on the domain $[0,1]$, we assume that we had set $c=1$ in the previous analysis, section 2.1, where we non-dimensionalized the Navier-Stokes equations.

To numerically solve this bifurcation problem using real variables, we substitute $\tilde{V}(y)\equiv\sigma(y)+i\tau(y)$, to get the pair of differential equations:

$$\begin{aligned}\alpha\sin(ny)\left(\frac{d^2\tau}{dy^2}+n^2\tau-\alpha^2\tau-\beta^2\tau\right)&=\frac{1}{\Omega}\left((\alpha^2+\beta^2)^2\sigma-2(\alpha^2+\beta^2)\frac{d^2\sigma}{dy^2}+\frac{d^4\sigma}{dy^4}\right),\\ \alpha\sin(ny)\left(-\frac{d^2\sigma}{dy^2}-n^2\sigma+\alpha^2\sigma+\beta^2\sigma\right)&=\frac{1}{\Omega}\left((\alpha^2+\beta^2)^2\tau-2(\alpha^2+\beta^2)\frac{d^2\tau}{dy^2}+\frac{d^4\tau}{dy^4}\right).\end{aligned} \tag{2.29}$$

We rewrite this in the form of an autonomous system of first order differential equations:

$$\begin{gathered}
\frac{d\sigma_1}{dy} = \sigma_2, \qquad \frac{d\sigma_2}{dy} = \sigma_3, \qquad \frac{d\sigma_3}{dy} = \sigma_4, \\
\frac{d\sigma_4}{dy} = 2(\alpha^2+\beta^2)\sigma_3 - (\alpha^2+\beta^2)^2\sigma_1 + \Omega\alpha\sin(nv)(\tau_3 + (n^2-\alpha^2-\beta^2)\tau_1), \\
\frac{d\tau_1}{dy} = \tau_2, \qquad \frac{d\tau_2}{dy} = \tau_3, \qquad \frac{d\tau_3}{dy} = \tau_4, \\
\frac{d\tau_4}{dy} = 2(\alpha^2+\beta^2)\tau_3 - (\alpha^2+\beta^2)^2\tau_1 - \Omega\alpha\sin(nv)(\sigma_3 + (n^2-\alpha^2-\beta^2)\sigma_1), \\
\frac{dv}{dy} = 1.
\end{gathered} \tag{2.30}$$

With boundary conditions

$$\begin{gathered}
\sigma_1(0) = \sigma_1(1), \qquad \sigma_2(0) = \sigma_2(1), \qquad \sigma_3(0) = \sigma_3(1), \qquad \sigma_4(0) = \sigma_4(1), \\
\tau_1(0) = \tau_1(1), \qquad \tau_2(0) = \tau_2(1), \qquad \tau_3(0) = \tau_3(1), \qquad \tau_4(0) = \tau_4(1), \\
v(0) = 0.
\end{gathered} \tag{2.31}$$

This system inherits two degrees of freedom from the magnitude and phase of $\tilde{V}(y)$. These are resolved by adding constraints to the system; an integral condition on the norm resolves the degeneracy in the magnitude:

$$\int_0^1 \sum_{i=1}^{4} (\sigma_i^2 + \tau_i^2)\,dy = \eta. \tag{2.32}$$

To remove degeneracy due to the phase, we introduce an unfolding parameter μ, and add the term $\mu\sin(2\pi v)$ to (2.30), which yields:

$$\frac{d\sigma_4}{dy} = 2(\alpha^2+\beta^2)\sigma_3 - (\alpha^2+\beta^2)^2\sigma_1 + \Omega\alpha\sin(nv)(\tau_3 + (n^2-\alpha^2-\beta^2)\tau_1) + \mu\sin(2\pi v). \tag{2.33}$$

We have nine ordinary differential equations, and nine boundary conditions as well as one integral condition, which requires that we have an additional free parameter during continuation.

We compute the bifurcation curves using the same method that Dinar and Keller performed to compute the bifurcation curves on Taylor-Couette flow. First we start with $\alpha = 1$, $\beta = 0$, $\eta = 0$ and $\mu = 0.001$, and continue in Ω with η as a free parameter. We cannot continue with $\alpha = 0$ since the system has no solution, and when $\mu = 0$ the system is singular. Also choosing $\mu \neq 0$ breaks apart the bifurcation points so that when Ω approaches a value at which the Navier-Stokes equations have a bifurcation, the free parameter η increases.

At this point we reduce the size of μ by continuing in μ with α as the free parameter. As mentioned before the system is singular when $\mu = 0$ so we typically reduce μ to approximately 10^{-5}. We did not use this smaller value of μ in the first continuation to ensure that AUTO switched branches.

Finally we continue in α, with Ω as a free parameter, to trace out the bifurcation curve. Figure 2.2 shows the curves obtained when $\beta = 0$. From this calculation we find that the smallest parameter value at which bifurcation occurs is when $\Omega = n\sqrt{2}$. We define Ω_c to be this value.

The curves obtained for $\beta = 1$ and $\beta = 2$ are shown in figures 2.3 and 2.4 respectively. To get the curves for $\beta \neq 0$, either we can perform the whole continuation process again starting with a different value of β, or we can start from a solution where $\beta = 0$ and continue in β with Ω as the free parameter.

2.2.3 Analytic Calculation

To analytically determine the bifurcations points of the shear flow, we expand $\tilde{V}(y)$ in (2.28) as a Fourier series:

$$\tilde{V}(y) = \sum_{m=-\infty}^{\infty} c_m e^{imy}, \tag{2.34}$$

and use the complex exponential definition of the sin function to derive a recurrence relation in c_m:

$$c_m \frac{2}{\Omega\alpha}(\alpha^2 + m^2 + \beta^2)^2 + c_{m-n}((m-n)^2 - n^2 + \alpha^2 + \beta^2) \\ - c_{m+n}((m+n)^2 - n^2 + \alpha^2 + \beta^2) = 0. \tag{2.35}$$

This recurrence relation is similar to the one derived in Meshalkin and Sinai [26].

We consider the recurrence relation in $\{\dots, c_{k-2n}, c_{k-n}, c_k, c_{k+n}, c_{k+2n}, \dots\}$, and write this as a linear system. Bifurcations from the shear flow occur when the coefficient matrix of this system is singular. We use the idea of H.B. Keller to approximate this infinite matrix by a convergent sequence of its centred principal minors, and we prove that a convergent sequence of parameter values at which the minors are singular, converges to a parameter value at which the infinite matrix is singular.

Convergence for Singly Infinite Matrix

Given the singly infinite matrix:

$$\begin{pmatrix} \beta_1 x & \gamma_1 & & \\ \alpha_2 & \beta_2 x & \gamma_2 & \\ & \alpha_3 & \beta_3 x & \ddots \\ & & \ddots & \ddots \end{pmatrix}, \tag{2.36}$$

we use the idea of H.B. Keller to approximate the value of x for which this matrix is singular by a sequence $\{x_n\}$ for which the n'th leading minor is singular. We prove convergence with the condition that $\sum_{n=1}^{\infty} k_n$ is absolutely convergent, where $k_n \equiv \frac{\alpha_{n+1}\gamma_n}{\beta_{n+1}\beta_n}$.

Assuming that $x \neq 0$, and for all j, $\beta_j \neq 0$, we divide the matrix by its diagonal, leaving:

$$\begin{pmatrix} 1 & \frac{\gamma_1}{\beta_1 x} & & \\ \frac{\alpha_2}{\beta_2 x} & 1 & \frac{\gamma_2}{\beta_2 x} & \\ & \frac{\alpha_3}{\beta_3 x} & 1 & \ddots \\ & & \ddots & \ddots \end{pmatrix}. \tag{2.37}$$

With the above conditions we have that

$$\begin{pmatrix} \beta_1 x & \gamma_1 & & \\ \alpha_2 & \beta_2 x & \gamma_2 & \\ & \alpha_3 & \beta_3 x & \ddots \\ & & \ddots & \ddots \end{pmatrix} \text{ is singular if and only if } \begin{pmatrix} 1 & \frac{\gamma_1}{\beta_1 x} & & \\ \frac{\alpha_2}{\beta_2 x} & 1 & \frac{\gamma_2}{\beta_2 x} & \\ & \frac{\alpha_3}{\beta_3 x} & 1 & \ddots \\ & & \ddots & \ddots \end{pmatrix}$$

is singular.

For $x \in \mathbb{C}$ we define the polynomial $P_n : \mathbb{C} \to \mathbb{C}$ by

$$P_n(x) \equiv \begin{vmatrix} \beta_1 x & \gamma_1 & & & \\ \alpha_2 & \beta_2 x & \gamma_2 & & \\ & \ddots & \ddots & \ddots & \\ & & \alpha_{n-1} & \beta_{n-1}x & \gamma_{n-1} \\ & & & \alpha_n & \beta_n x \end{vmatrix} \tag{2.38}$$

and provided $x \neq 0$, and for all j, $\beta_j \neq 0$, we define $Q_n : \mathbb{C} \to \mathbb{C}$ by

$$Q_n(x) \equiv \begin{vmatrix} 1 & \frac{\gamma_1}{\beta_1 x} & & & \\ \frac{\alpha_2}{\beta_2 x} & 1 & \frac{\gamma_2}{\beta_2 x} & & \\ & \ddots & \ddots & \ddots & \\ & & \frac{\alpha_{n-1}}{\beta_{n-1}}x & 1 & \frac{\gamma_{n-1}}{\beta_{n-1}x} \\ & & & \frac{\alpha_n}{\beta_n x} & 1 \end{vmatrix}. \tag{2.39}$$

Lemma 2.2 *Assuming $x \neq 0$ and for all j, $\beta_j \neq 0$, we have $P_n(x) = 0$ if and only if $Q_n(x) = 0$.*

Proof: Clearly

$$\begin{pmatrix} \beta_1 x & \gamma_1 & & \\ \alpha_2 & \beta_2 x & \ddots & \\ & \ddots & \ddots & \gamma_{n-1} \\ & & \alpha_n & \beta_n x \end{pmatrix} = \begin{pmatrix} \beta_1 x & & & \\ & \beta_2 x & & \\ & & \ddots & \\ & & & \beta_n x \end{pmatrix} \begin{pmatrix} 1 & \frac{\gamma_1}{\beta_1 x} & & \\ \frac{\alpha_2}{\beta_2 x} & 1 & \ddots & \\ & \ddots & \ddots & \frac{\gamma_{n-1}}{\beta_{n-1}x} \\ & & \frac{\alpha_n}{\beta_n x} & 1 \end{pmatrix}. \tag{2.40}$$

Taking the determinant yields

$$P_n(x) = x^n Q_n(x) \prod_{j=1}^{n} \beta_j. \tag{2.41}$$

Therefore, using the assumption that $x \neq 0$ and for all j, $\beta_j \neq 0$, we have the result that $P_n(x) = 0$ if and only if $Q_n(x) = 0$.

□

We make the assumption that for all $n > 1$, $P_n(x) \neq x^n$. Then P_n has a non-zero root, and hence Q_n has a non-zero root. Thus it follows that there exists a sequence $\{x_n\}$ with $Q_n(x_n) = 0$ and $x_n \neq 0$.

Lemma 2.3 *If the series $\sum_{n=1}^{\infty} k_n$ is absolutely convergent, then for all $x \neq 0$ the sequence $\{Q_n(x)\}$ converges. We define $Q(x)$ to be this limit.*

Proof: From the definition of $Q_n(x)$ we derive the recurrence relation $Q_{n+1}(x) = Q_n(x) - \frac{k_n}{x^2}Q_{n-1}(x)$, with starting values $Q_1(x) = 1$ and $Q_2(x) = 1 + \frac{k_1}{x^2}$. To show convergence of $\{Q_n(x)\}$, we define the recurrence relation $R_{n+1}(x) = R_n(x) + \frac{|k_n|}{|x^2|}R_{n-1}(x)$, with starting values $R_1(x) = |Q_1(x)|$ and $R_2(x) = |Q_2(x)|$. It is easily proved by induction that for all n, $R_n(x) \geq |Q_n(x)|$, and that $R_n(x) \geq R_{n-1}(x)$.

Using $R_n(x) \geq R_{n-1}(x)$ we obtain

$$R_{n+1}(x) \leq \left(1 + \frac{|k_n|}{|x^2|}\right) R_n(x) \leq R_1(x) \prod_{j=1}^{n} \left(1 + \frac{|k_j|}{|x^2|}\right). \tag{2.42}$$

Since $\sum k_j$ is absolutely convergent implies that the above product converges for all $x \neq 0$ as $n \to \infty$ (see Apsotol [2] p. 381,) we have that $\{R_n(x)\}$ is bounded, and therefore $\{|Q_n(x)|\}$ is bounded.

Let $\hat{Q}(x)$ be a bound on $\{|Q_n(x)|\}$. Then

$$|Q_{n+1}(x) - Q_n(x)| = \left|\frac{k_n}{x^2}Q_{n-1}(x)\right| \leq \frac{|k_n|}{|x^2|}\hat{Q}(x). \tag{2.43}$$

Now using the absolute convergence of $\sum k_j$, we get the result that $\{Q_n(x)\}$ converges for all $x \neq 0$.

□

Theorem 2.4 *For all $\epsilon > 0$, if $\{Q_n\}$ converges pointwise to Q in $D_\epsilon \equiv \{x \in \mathbb{C} : |x| \geq \epsilon\}$, then $\{Q_n\}$ converges uniformly to Q in D_ϵ.*

Proof: In the domain D_ϵ, $Q_n(x)$ has no poles and $Q_n(x) \to 1$ as $|x| \to \infty$, from (2.41). Thus $|Q_{n+1}(x) - Q_n(x)|$ is bounded by $M_n \equiv \sup_{x \in D_\epsilon} \frac{|k_n|}{|x^2|}\hat{Q}(x)$. Now given that $\sum k_n$ is absolutely convergent, clearly $\sum M_n$ converges. Therefore, by Weierstrass' M-test, $\{Q_n\}$ converges uniformly to Q in D_ϵ.

□

Theorem 2.5 *If $\{x_n\}$ is a convergent sequence with $Q_n(x_n) = 0$ and $x \equiv \lim_{n\to\infty} x_n \neq 0$, then $Q(x) = 0$.*

Proof: Since $x \neq 0$ we can pick ϵ sufficiently small so that $x \in D_\epsilon$. Then given that $\{Q_n\}$ converges uniformly to Q on D_ϵ, we have that Q is continuous on D_ϵ.

□

Theorem 2.6 *We assume that (2.36) is a real matrix. If $Q(x) = 0$ and Q is invertible with a continuous inverse in a neighbourhood of x, then there exists a sequence $\{x_n\}$ that converges to x with $Q_n(x_n) = 0$.*

Proof: Since Q is invertible with a continuous inverse, there exists an ϵ_1 such that Q is injective on $B_{\epsilon_1}(x)$. We also choose ϵ_1 small enough so that $0 \notin B_{\epsilon_1}(x)$.

We choose δ_1 small enough such that $|Q(x - \epsilon_1)| < 2\delta_1$ and $|Q(x + \epsilon_1)| < 2\delta_1$. Without loss of generality we assume that $Q(x - \epsilon_1) < -2\delta_1$ and $Q(x + \epsilon_1) > 2\delta_1$.

Since $\{Q_n\}$ converges uniformly to Q, for all $\delta_1 > 0$ there exists N_1 such that for all $n > N_1$ and for all $y \in D_\epsilon$, we have $|Q_n(y) - Q(y)| < \delta_1$. This implies that $|Q_n(x - \epsilon_1) - Q(x - \epsilon_1)| < \delta_1$. Therefore, we have

$$\begin{aligned} Q_n(x - \epsilon_1) - Q(x - \epsilon_1) &< \delta_1, \\ Q_n(x - \epsilon_1) &< \delta_1 + Q(x - \epsilon_1), \\ &< \delta_1 - 2\delta_1 < 0. \end{aligned} \tag{2.44}$$

Similarly we can show that $Q_n(x+\epsilon_1) > 0$. Therefore, by the intermediate value theorem there exists $x_n \in B_{\epsilon_1}(x)$ such that $Q_n(x_n) = 0$.

Now we use the triangle inequality to get

$$|Q(x_n) - Q(x)| \leq |Q_n(x_n) - Q(x_n)| + |Q_n(x_n) - Q(x)| < \delta_1. \tag{2.45}$$

The definition of Q^{-1} continuous at x, gives that for all $\epsilon_2 > 0$ there exists δ_2 such that for all y, $|Q(y) - Q(x)| < \delta_2$ implies $|y - x| < \epsilon_2$. Therefore, given ϵ_2, there exists an N so that for all $n > N$, $|Q(x_n) - Q(x)| < \delta_2$, and hence $|x_n - x| < \epsilon_2$.

□

Convergence for Doubly Infinite Matrix

Now we consider the doubly infinite case. Suppose we have the matrix

$$\begin{pmatrix} \ddots & \ddots & & & \\ \ddots & \beta_{-1}x & \gamma_{-1} & & \\ & \alpha_0 & \beta_0 x & \gamma_0 & \\ & & \alpha_1 & \beta_1 x & \ddots \\ & & & \ddots & \ddots \end{pmatrix}. \tag{2.46}$$

As in the singly infinite case, we assume that for all j, $\beta_j \neq 0$, and $x \neq 0$. Then we divide the matrix by its diagonal which leaves

$$\begin{pmatrix} \ddots & \ddots & & & \\ \ddots & 1 & \frac{\gamma_{-1}}{\beta_{-1}x} & & \\ & \frac{\alpha_0}{\beta_0 x} & 1 & \frac{\gamma_0}{\beta_0 x} & \\ & & \frac{\alpha_1}{\beta_1 x} & 1 & \ddots \\ & & & \ddots & \ddots \end{pmatrix}. \tag{2.47}$$

Recall that we want to determine the values of x for which this matrix is singular. This is achieved by locating where the determinant is zero.

The determinant of this matrix is said to converge if the determinant of

$$\begin{pmatrix} 1 & \frac{\gamma_{-m}}{\beta_{-m}x} & & \\ \frac{\alpha_{-m+1}}{\beta_{-m+1}x} & 1 & \ddots & \\ & \ddots & \ddots & \frac{\gamma_{n-1}}{\beta_{n-1}x} \\ & & \frac{\alpha_n}{\beta_n x} & 1 \end{pmatrix} \tag{2.48}$$

converges as $m \to \infty$ and $n \to \infty$.

We consider the sequence of minors that are centred, i.e., have $m = n$, and we expand the determinant about the central row.

$$\begin{vmatrix} \ddots & \ddots & & & \\ \ddots & 1 & \frac{\gamma_{-1}}{\beta_{-1}x} & & \\ & \frac{\alpha_0}{\beta_0 x} & 1 & \frac{\gamma_0}{\beta_0 x} & \\ & & \frac{\alpha_1}{\beta_1 x} & 1 & \ddots \\ & & & \ddots & \ddots \end{vmatrix} = \begin{vmatrix} \ddots & \ddots & & & & \\ \ddots & 1 & \frac{\gamma_{-2}}{\beta_{-2}x} & & & \\ & \frac{\alpha_{-1}}{\beta_{-1}x} & 1 & 0 & & \\ & & 0 & 1 & \frac{\gamma_1}{\beta_1 x} & \\ & & & \frac{\alpha_2}{\beta_2 x} & 1 & \ddots \\ & & & & \ddots & \ddots \end{vmatrix}$$

$$- \frac{\alpha_0}{\beta_0 x} \begin{vmatrix} \ddots & \ddots & & & & \\ \ddots & 1 & \frac{\gamma_{-3}}{\beta_{-3}x} & & & \\ & \frac{\alpha_{-2}}{\beta_{-2}x} & 1 & 0 & & \\ & & \frac{\alpha_{-1}}{\beta_{-1}x} & \frac{\gamma_{-1}}{\beta_{-1}x} & 0 & \\ & & & \frac{\alpha_1}{\beta_1 x} & 1 & \frac{\gamma_1}{\beta_1 x} \\ & & & & \frac{\alpha_2}{\beta_2 x} & 1 & \ddots \\ & & & & & \ddots & \ddots \end{vmatrix}$$

$$- \frac{\gamma_0}{\beta_0 x} \begin{vmatrix} \ddots & \ddots & & & & & \\ \ddots & 1 & \frac{\gamma_{-2}}{\beta_{-2}x} & & & & \\ & \frac{\alpha_{-1}}{\beta_{-1}x} & 1 & \frac{\gamma_{-1}}{\beta_{-1}x} & & & \\ & & 0 & \frac{\alpha_1}{\beta_1 x} & \frac{\gamma_1}{\beta_1 x} & & \\ & & & 0 & 1 & \frac{\gamma_2}{\beta_2 x} & \\ & & & & \frac{\alpha_3}{\beta_3 x} & 1 & \ddots \\ & & & & & \ddots & \ddots \end{vmatrix} \tag{2.49}$$

We note that each term in the above equation is the determinant of a block triangular matrix, which is equal to the product of the determinant of the diagonal blocks.

Hence we have

$$Q_n^0(x) \equiv Q_n^{1+}(x)Q_n^{1-}(x) - \frac{\alpha_0\gamma_{-1}}{\beta_0\beta_{-1}x^2}Q_n^{1+}(x)Q_n^{2-}(x) - \frac{\alpha_1\gamma_0}{\beta_0\beta_1 x^2}Q_n^{2+}(x)Q_n^{1-}(x). \tag{2.50}$$

Where

$$Q_n^{1+}(x) \equiv \begin{vmatrix} 1 & \frac{\gamma_1}{\beta_1 x} & & \\ \frac{\alpha_2}{\beta_2 x} & 1 & \ddots & \\ & \ddots & \ddots & \frac{\gamma_{n-1}}{\beta_{n-1}x} \\ & & \frac{\alpha_n}{\beta_n x} & 1 \end{vmatrix}, \qquad Q_n^{1-}(x) \equiv \begin{vmatrix} 1 & \frac{\gamma_{-n}}{\beta_{-n}x} & & \\ \frac{\alpha_{-n+1}}{\beta_{-n+1}x} & 1 & \ddots & \\ & \ddots & \ddots & \frac{\gamma_{-2}}{\beta_{-2}x} \\ & & \frac{\alpha_{-1}}{\beta_{-1}x} & 1 \end{vmatrix},$$

and

$$Q_n^{2+}(x) \equiv \begin{vmatrix} 1 & \frac{\gamma_2}{\beta_2 x} & & \\ \frac{\alpha_3}{\beta_3 x} & 1 & \ddots & \\ & \ddots & \ddots & \frac{\gamma_{n-1}}{\beta_{n-1}x} \\ & & \frac{\alpha_n}{\beta_n x} & 1 \end{vmatrix}, \qquad Q_n^{2-}(x) \equiv \begin{vmatrix} 1 & \frac{\gamma_{-n}}{\beta_{-n}x} & & \\ \frac{\alpha_{-n+1}}{\beta_{-n+1}x} & 1 & \ddots & \\ & \ddots & \ddots & \frac{\gamma_{-3}}{\beta_{-3}x} \\ & & \frac{\alpha_{-2}}{\beta_{-2}x} & 1 \end{vmatrix}.$$

By the analysis of the singly infinite matrix, if both the series $\sum_{n=1}^{\infty} k_n$ and $\sum_{n=1}^{\infty} k_{-n}$ are absolutely convergent, then the sequences $\{Q_n^{1+}\}$, $\{Q_n^{2+}\}$, $\{Q_n^{1-}\}$, and $\{Q_n^{2-}\}$ all converge uniformly in D_ϵ to the continuous functions Q^{1+}, Q^{2+}, Q^{1-}, and Q^{2-} respectively.

Hence the sequence $\{Q_n^0\}$ converges uniformly in D_ϵ to the continous function Q^0, where:

$$Q^0(x) \equiv Q^{1+}(x)Q^{1-}(x) - \frac{\alpha_0\gamma_{-1}}{\beta_0\beta_{-1}x^2}Q^{1+}(x)Q^{2-}(x) - \frac{\alpha_1\gamma_0}{\beta_0\beta_1 x^2}Q^{2+}(x)Q^{1-}(x). \tag{2.51}$$

Theorem 2.6 also holds for the case of the doubly infinite matrix.

2.2.4 Results

We now find the curve of singular points of the infinite matrix. This shows how the bifurcations points vary as the aspect ratio is altered.

First we consider the recurrence relation in the variables $\{\dots, c_{-2n}, c_{-n}, c_0, c_n, c_{2n}, \dots\}$. We note that the entries in our matrix are real so the assumption of theorem 2.6 holds.

The first approximation to $\tilde{V}(y)$ is the 3x3 minor, which we simplify by setting $d^2 = \alpha^2 + \beta^2$, and $\kappa = \frac{2}{\Omega\alpha}$, to give

$$\begin{pmatrix} \kappa(d^2+n^2)^2 & -(d^2-n^2) & \\ d^2 & \kappa(d^2)^2 & -d^2 \\ & d^2-n^2 & \kappa(d^2+n^2)^2 \end{pmatrix} \begin{pmatrix} c_{-n} \\ c_0 \\ c_n \end{pmatrix} = \begin{pmatrix} 0 \\ 0 \\ 0 \end{pmatrix}. \tag{2.52}$$

The coefficient matrix is singular when its determinant is zero, which yields the equation

$$\kappa(\kappa^2 d^4(d^2+n^2)^4 + 2d^2(d^2+n^2)^2(d^2-n^2)) = 0. \tag{2.53}$$

By definition the Reynolds number Ω and the aspect ratio α are both real and positive; therefore, the only physically relevant solutions of κ are when it is real and positive. Solving for κ gives the positive real solution:

$$\kappa = \sqrt{2}\frac{\sqrt{n^2-d^2}}{d(d^2+n^2)}. \tag{2.54}$$

Therefore, a first approximation to the bifurcation points is

$$\Omega = \frac{\sqrt{2}\sqrt{(A^2r^2+B^2s^2)}(A^2r^2+B^2s^2+n^2)}{Ar\sqrt{n^2-A^2r^2-B^2s^2}}. \tag{2.55}$$

The smallest value of Ω at which a bifurcation occurs is when $\Omega = n\sqrt{2}$; this corresponds to $r = 0$ and $s = 0$. We define Ω_c to be this value.

Better approximations are obtained by using larger centred principal minors. For the next approximation we use the 5x5 minor:

$$\begin{pmatrix} \kappa(d^2+4n^2)^2 & -d^2 & & & \\ d^2+3n^2 & \kappa(d^2+n^2)^2 & -(d^2-n^2) & & \\ & d^2 & \kappa(d^2)^2 & -d^2 & \\ & & d^2-n^2 & \kappa(d^2+n^2)^2 & -(d^2+3n^2) \\ & & & d^2 & \kappa(d^2+4n^2)^2 \end{pmatrix}. \tag{2.56}$$

The determinant of a minor is calculated using an algebraic manipulator, and the resulting polynomial is solved to give the locations of the bifurcation points. We choose to do

the expansions centred around zero, although it is possible to use asymmetric expansions. In table 2.1 we show the computed locations of the bifurcation points for various sizes of the minor when $A = B = 1$.

r	s	Ω/Ω_c			
		3x3 minor	5x5 minor	7x7 minor	9x9 minor
1	0	1.09735	1.09756	1.09756	1.09756
2	0	1.44338	1.44882	1.44879	1.44879
3	0	2.36228	2.43895	2.43686	2.43687
1	1	1.70084	1.70224	1.70223	1.70223
2	1	1.76977	1.78108	1.78100	1.78100
3	1	2.79715	2.92942	2.92425	2.92431
1	2	3.53955	3.56215	3.56200	3.56200
2	2	3.00000	3.06699	3.06570	3.06570
3	2	5.03069	5.96945	5.82213	5.82773
1	3	8.39146	8.78827	8.77275	8.77294
2	3	7.54604	8.95418	8.73319	8.74159

Table 2.1: Bifurcation Points for $A = B = 1$

We find the location of the bifurcation points as the aspect ratio A is varied. This gives us the same bifurcation curves as we found with AUTO; see figures 2.2-2.4. These figures are for $s = 0, 1, 2$ respectively, with $B = 1$, and $r = 1, \ldots, 10$. The curves obtained from this approximation method and from AUTO tend to the same result as the accuracy of both methods is increased.

The two-dimensional bifurcation curves all approach $\Omega_c = n\sqrt{2}$ as $A \to 0$. This agrees with the result due to Sinai.

The bifurcation curves to three-dimensional flow are of a similar form to those found by Dinar and Keller [11], for bifurcation from Taylor-Couette flow. Their results show how the Reynolds number of bifurcation points to Taylor-Vortex flows vary as the aspect ratio of the system is changed. Likewise, we vary the aspect ratio of our system and obtain similar results.

For $n \neq 1$ we observe that there exist other recurrence relations that are not centred around the zero wavenumber, i.e., in the variables $\{\ldots, c_{k-2n}, c_{k-n}, c_k, c_{k+n}, c_{k+2n}, \ldots\}$, for $k \neq 0$. The same analysis can be applied; however, we observed that the first few minors are not singular for any real non-zero parameter value.

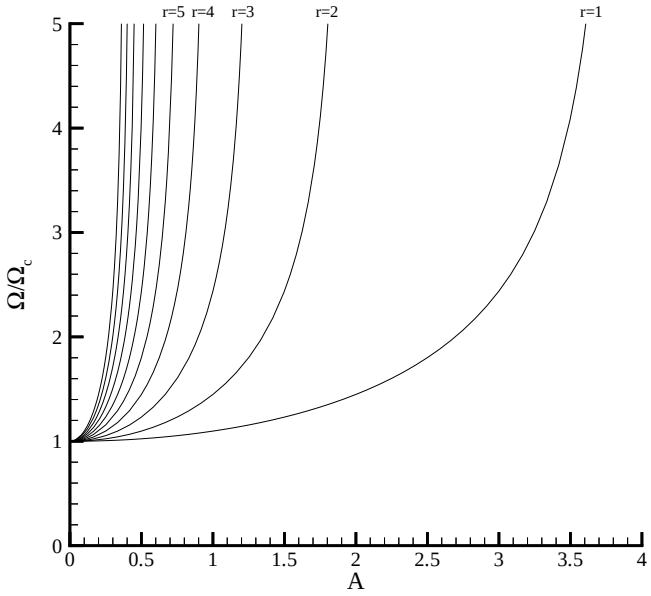

Figure 2.2: Bifurcation Curves for B=1, s=0

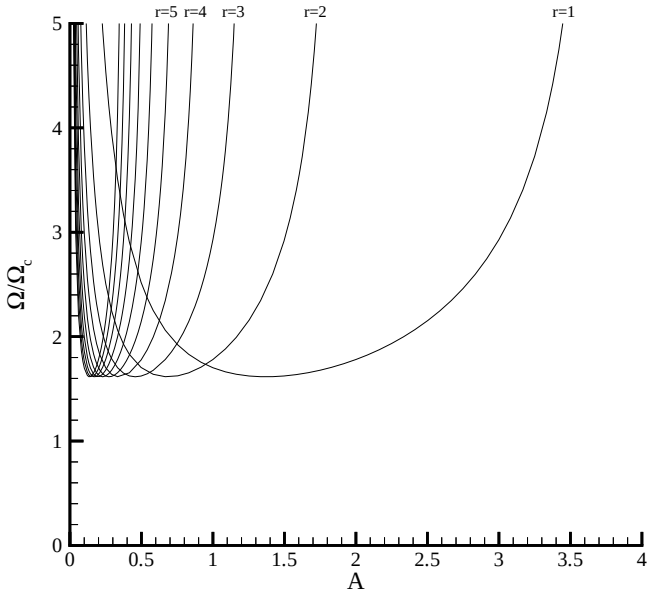

Figure 2.3: Bifurcation Curves for B=1, s=1

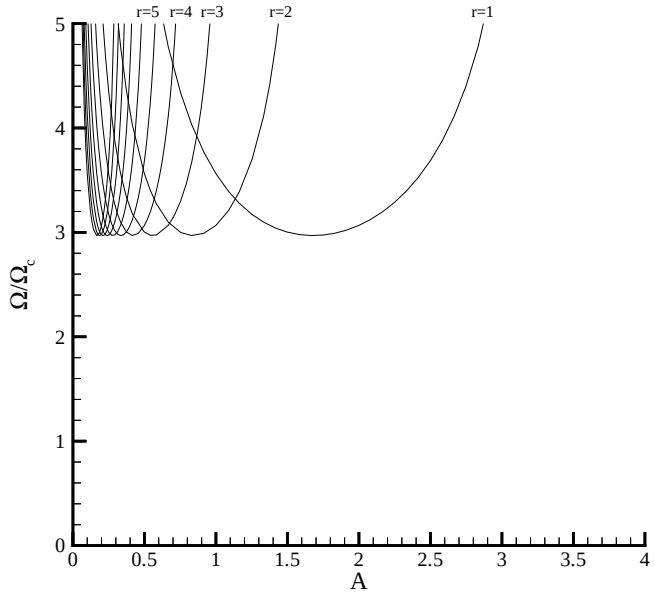

Figure 2.4: Bifurcation Curves for B=1, s=2

Chapter 3 Numerical Method

We compute solutions of the Navier-Stokes equations (2.4)-(2.7), in order to examine the behaviour of Kolmogorov flow along the bifurcating branches as the Reynolds number is increased.

We discretize the partial differential equation using spectral methods rather than finite differences, to give spectral accuracy. Leonard and Wray [21] have proposed a new set of basis functions for discretizing divergence free flows. These basis functions are divergence free, so that any vector function expanded in them automatically satisfies the divergence free condition. Some benefits of their expansion are that the pressure is eliminated from the dynamics, and there are only two unknowns per "mesh point." However, the matrices required to solve a system are complicated to construct, and there is some additional effort required in converting back to the original variables.

In our approach we also have only two unknowns per "mesh point." However, we use standard basis functions and instead of eliminating the pressure and one velocity component, we regard them as being dependent on the other two velocity components.

We briefly explain our use of the pseudospectral Fourier-Collocation method, full details of which can be found in Gottlieb and Orszag [16]. Then we discuss the details of the method that we use to solve the Navier-Stokes equations.

3.1 Discretization

Since we are studying Kolmogorov flow on a periodic domain, it is natural that we approximate the velocity and pressure fields using finite Fourier series, since these basis functions already satisfy the periodic boundary conditions.

If we use N_x, N_y, and N_z basis functions in the x, y, and z directions respectively, then we approximate the function $u(x, y, z)$, which is defined on a three-dimensional 2π periodic

domain by

$$u(x,y,z) \equiv \frac{1}{N_x N_y N_z} \sum_{k_x,k_y,k_z} \hat{u}_{k_x k_y k_z} e^{-ik_x x} e^{-ik_y y} e^{-ik_z z}, \tag{3.1}$$

where $-N_x/2 \leq k_x < N_x/2$,$-N_y/2 \leq k_y < N_y/2$, and $-N_z/2 \leq k_z < N_z/2$. We define similar expansions for all of the velocity components and the pressure.

We approximate the Navier-Stokes equations using collocation, which means that we evaluate the non-linear advective terms at a set of collocation points in physical space.

To compute the product s of two functions u and v using collocation, given their coefficients from the expansion (3.1), we introduce $N_x N_y N_z$ collocation points. These collocation points are arranged on an equally spaced Cartesian grid of N_x by N_y by N_z points. In order to use the standard fast transform method, we impose the restriction that N_x,N_y, and N_z are powers of two.

First we calculate the value of the two functions u and v at all of the collocation points using (3.1). This gives the values $u_{m_x m_y m_z} \equiv u(2\pi m_x/N_x, 2\pi m_y/N_y, 2\pi m_z/N_z)$ and $v_{m_x m_y m_z} \equiv v(2\pi m_x/N_x, 2\pi m_y/N_y, 2\pi m_z/N_z)$ for $0 \leq m_x < N_x$, $0 \leq m_y < N_y$, and $0 \leq m_z < N_z$. Then at each collocation point we take the product of the two functions and define $s_{m_x m_y m_z} \equiv u_{m_x m_y m_z} v_{m_x m_y m_z}$. Finally, we determine the coefficients $\hat{s}_{k_x k_y k_z}$ of the Fourier expansion of the product s from its values $s_{m_x m_y m_z}$ at the collocation points with

$$\hat{s}_{k_x k_y k_z} = \sum_{m_x,m_y,m_z} s_{m_x m_y m_z} e^{ik_x x_{m_x}} e^{ik_y y_{m_y}} e^{ik_z z_{m_z}}. \tag{3.2}$$

We define $col(u,v)$ to be the product of the two functions u and v evaluated using the above procedure.

However, this procedure introduces aliasing errors, which get introduced because on a finite grid a high wavenumber mode is indistinguishable from a lower wavenumber mode. The solution to this problem for quadratic non-linearities is to set the coefficients of the largest third of the wavenumbers of $col(u,v)$ equal to zero.

Derivatives in the Navier-Stokes equations are evaluated directly from the coefficients

of the Fourier expansion (3.1), so that differentiation with respect to x is given by

$$\frac{\partial u}{\partial x}(x,y,z) \equiv \frac{1}{N_x N_y N_z} \sum_{k_x,k_y,k_z} -ik_x \hat{u}_{k_x k_y k_z} e^{-ik_x x} e^{-ik_y y} e^{-ik_z z}, \tag{3.3}$$

and the other derivatives are defined similarly.

The x-momentum equation, excluding the pressure term, evaluated using Fourier Collocation is given by

$$\begin{aligned}\hat{F}_{k_x k_y k_z} \equiv \frac{1}{\Omega}(-A^2 k_x^2 - k_x^2 - B^2 k_z^2)\hat{u}_{k_x k_y k_z} + \frac{n^2}{2i\Omega}\delta_{k_x 0}\delta_{k_z 0}(\delta_{k_y n} - \delta_{-k_y n}) \\ - col(u, A\frac{\partial u}{\partial x})_{k_x k_y k_z} - col(v, \frac{\partial u}{\partial y})_{k_x k_y k_z} - col(w, B\frac{\partial u}{\partial z})_{k_x k_y k_z},\end{aligned} \tag{3.4}$$

where δ_{ij} is the Kronecker Delta. The other momentum equations and the continuity equation are defined similarly.

Theorem 2.1 implies $\hat{F}_{000} = \hat{G}_{000} = \hat{H}_{000} = 0$. Therefore, instead of numerically integrating the differential equations for $\hat{u}_{000}, \hat{v}_{000}$, and $\hat{w}_{000}$, we set $\hat{u}_{000} = \hat{v}_{000} = \hat{w}_{000} = 0$.

Discretization leaves the following system of differential algebraic equations:

$$\begin{aligned}\frac{d\hat{u}_{k_x k_y k_z}}{dt} &= \hat{F}_{k_x k_y k_z} + iAk_x \hat{p}_{k_x k_y k_z}, \\ \frac{d\hat{v}_{k_x k_y k_z}}{dt} &= \hat{G}_{k_x k_y k_z} + ik_y \hat{p}_{k_x k_y k_z}, \\ \frac{d\hat{w}_{k_x k_y k_z}}{dt} &= \hat{H}_{k_x k_y k_z} + iBk_z \hat{p}_{k_x k_y k_z},\end{aligned} \tag{3.5}$$

$$iAk_x \hat{u}_{k_x k_y k_z} + ik_y \hat{v}_{k_x k_y k_z} + iBk_z \hat{w}_{k_x k_y k_z} = 0, \tag{3.6}$$

for the range of k_x,k_y, and k_z mentioned earlier, and the equations for $k_x = k_y = k_z = 0$ are absent. We observe that the coefficient $\hat{p}_{000}$ does not appear in any of the equations. This corresponds the the normal indeterminacy of the pressure which is resolved by requiring

$$\int_0^{2\pi}\int_0^{2\pi}\int_0^{2\pi} p(x,y,z)dxdydz = 0; \tag{3.7}$$

this is equivalent to setting $\hat{p}_{000} = 0$.

3.2 Conversion from a DAE to an ODE

The spatially discretized Navier-Stokes equations yields a system of $3N_xN_yN_z - 3$ ordinary differential equations and $N_xN_yN_z - 1$ algebraic equations, with $4N_xN_yN_z - 4$ unknowns. Following the work of Keller and Von Sosen [19], we use the Implicit Function Theorem to reduce this DAE to a system of $2N_xN_yN_z - 2$ ordinary differential equations in $2N_xN_yN_z - 2$ unknowns.

This is achieved by using the knowledge that any solution to the Navier-Stokes equations must satisfy both the continuity and pressure equations. Therefore, we use these equations to make one velocity component and the pressure be functions of the other two velocity components.

For Kolmogorov flow, we use the continuity equation to calculate the values of the velocity coefficients that are in the set:

$$\begin{aligned}\mathbb{Y} \equiv \{\hat{w}_{k_x k_y k_z} : k_z \neq 0\} \cup \{\hat{v}_{k_x k_y k_z} : k_y \neq 0 \wedge k_z = 0\} \\ \cup \{\hat{u}_{k_x k_y k_z} : k_x \neq 0 \wedge k_y = 0 \wedge k_z = 0\},\end{aligned} \tag{3.8}$$

and we use the pressure Poisson equation to calculate all of the pressure coefficients.

For the remaining velocity coefficients, i.e., those in the set:

$$\begin{aligned}\mathbb{X} \equiv \{\hat{u}_{k_x k_y k_z} : k_x = 0 \vee k_y \neq 0 \vee k_z \neq 0\} \cup \{\hat{v}_{k_x k_y k_z} : k_y = 0 \vee k_z \neq 0\} \\ \cup \{\hat{w}_{k_x k_y k_z} : k_z = 0\} \setminus \{\hat{u}_{000}, \hat{v}_{000}, \hat{w}_{000}\},\end{aligned} \tag{3.9}$$

we have a system of ordinary differential equations that governs their behaviour.

3.2.1 Continuity Equation

Since we are looking for solution to the incompressible Navier-Stokes equations, we need to ensure that the continuity equation

$$A\frac{\partial u}{\partial x} + \frac{\partial v}{\partial y} + B\frac{\partial w}{\partial z} = 0 \tag{3.10}$$

is satisfied throughout our domain. The common approach for solving the incompressible Navier-Stokes equations in Computational Fluid Dynamics is to use Green's functions to

determine the pressure such that the flow remains divergence free at the next time step. However, we achieve this directly by using the continuity equation to calculate the last velocity component given the other two. Specifically we use the continuity equation to determine the velocity coefficients in the set $\mathbb{Y}$, defined in (3.8), by using the following formulas:

$$\hat{w}_{k_x k_y k_z} = \frac{-iAk_x\hat{u}_{k_x k_y k_z} - ik_y\hat{v}_{k_x k_y k_z}}{iBk_z}, \qquad \text{for } k_z \neq 0; \tag{3.11}$$

$$\hat{v}_{k_x k_y k_z} = \frac{-iAk_x\hat{u}_{k_x k_y k_z}}{ik_y}, \qquad \text{for } k_y \neq 0 \text{ and } k_z = 0; \tag{3.12}$$

$$\hat{u}_{k_x k_y k_z} = 0, \qquad \text{for } k_x \neq 0 \text{ and } k_y = k_z = 0. \tag{3.13}$$

3.2.2 Pressure Poisson Equation

We take the divergence of the momentum equations to give a Poisson equation for the pressure, with periodic boundary conditions. Since we are on a periodic domain, we have none of the usual problems relating to implementing Neumann boundary conditions at the walls.

There is no time evolution equation for the pressure, so the pressure is chosen such that the momentum equations are satisfied under the condition that the flow remains incompressible.

Recalling the definitions of $\hat{F}$,$\hat{G}$, and $\hat{H}$ from (3.4), the pressure is computed by

$$\hat{p}_{k_x k_y k_z} = \frac{-iAk_x\hat{F}_{k_x k_y k_z} - ik_y\hat{G}_{k_x k_y k_z} - iBk_z\hat{H}_{k_x k_y k_z}}{-A^2k_x^2 - k_y^2 - B^2k_z^2}. \tag{3.14}$$

Note that there is no equation for $\hat{p}_{000}$, which is consistent with the earlier assertion that due to the normal indeterminacy in the pressure, we set $\hat{p}_{000} = 0$.

3.3 Obtaining Steady State Solutions

The above use of the continuity and pressure Poisson equations means that we only have to consider the best method for finding steady state solutions of a differential equation, rather than of a differential algebraic equation. Note that to compute steady state solutions in both cases, we are only required to solve a system of non-linear algebraic equations. However the ODE formulation has half the number of unknowns, and the different formulations allows

us to consider different methods for finding these solutions.

There are many methods that can be used to solve algebraic non-linear systems, which include Newton's Method, Full Approximation Storage Multi-grid, or by integrating the differential equation until it reaches a steady state. Our choice of method needs to take into account that during continuation we need to be able to follow unstable branches, detect bifurcation points, and switch branches. Additionally we need to be able to augment the system by adding constraints, so that we can traverse folds and follow travelling wave solutions.

Most of the theory for numerical continuation assumes the use of Euler-Newton for following the branch, in particular factorizing the Jacobian while solving Newton's method. This factorization is used to give information about the location of the bifurcation points, along with the null vectors needed to switch branches. Additionally factorizing also allows the efficient use of the bordering algorithm to solve augmented systems. However, since we have a three-dimensional domain and have spatially discretized it using Fourier series, the Jacobian is dense; therefore, factorizing the Jacobian is not practical.

To solve the non-linear equations, we use Newton's method as an outer iteration. We solve the linear system for each Newton step with an inner iteration.

However, using an iterative method instead of factorizing the Jacobian to determine the correction at each Newton step means that we lose the benefits of the factorization, although branch switching can still be done easily by using the method of perturbed bifurcation. The bordering algorithm can no longer be used efficiently since we now have to solve two linear systems. Also, the right-hand side of the additional system is large, so there is the problem of round-off errors affecting how accurate a solution it can give. Therefore, we need to use alternative methods to determine the location of the bifurcation points, and to augment the system.

Methods for performing continutation while using preconditioned conjugate gradient type methods have been proposed by Tuckerman and Barkley [34]; however, these methods require additional work to determine the location of the bifurcation points. Additionally, their technique for determining bifurcation points assume that you have a good initial guess for location of the bifurcation points and the direction of the bifurcating branch.

The iterative methods we consider to solve the linear system in Newton's Method,

$\mathfrak{F}_u \Delta u = -\mathfrak{F}$, are suggested by the numerical integration of the ordinary differential equation:

$$\frac{d\Delta u}{d\tau} = \mathfrak{F}_u \Delta u + \mathfrak{F}. \tag{3.15}$$

We note that steady state solutions of this ordinary differential equation are solutions of the linear system $\mathfrak{F}_u \Delta u = -\mathfrak{F}$.

Convergence to a steady state requires that all the eigenvalues of $\mathfrak{F}_u$ are in the left half plane of $\mathbb{C}$. However, this is not always possible since at a bifurcation point an eigenvalue crosses the imaginary axis. We use the Recursive Projection Method on this inner iteration, which regains convergence on unstable branches, as well as accelerating convergence on stable branches.

Additionally RPM is used to provide the augmentation to the system and it gives approximations to the eigenvalues with largest real parts, so giving the approximate locations of the bifurcation points. Furthermore, if the solution is randomly perturbed at the beginning of each continuation step, then we can be assured that RPM will isolate all of the eigenvalues with largest real part, therefore giving the approximate locations of all the bifurcations points.

3.4 Solving For Newton Iterates

We solve the linear system $\mathfrak{F}_u \Delta u = -\mathfrak{F}$ by iteration. The iteration schemes that we use are suggested by numerically integrating the initial value problem:

$$\frac{d\Delta u}{d\tau} = \mathfrak{F}_u \Delta u + \mathfrak{F}, \qquad \Delta u(0) = 0 \tag{3.16}$$

in the dummy variable τ until it reaches a steady state, although in practice we stop the integration when the residual has been reduced to a predetermined amount. We integrate this ordinary differential equation by using a mixture of implicit and explicit schemes, thereby giving a large stability region while avoiding having to solve a large linear system at every time step.

Consider the ordinary differential equation:

$$\frac{dy}{d\tau} = f(y) + g(y). \tag{3.17}$$

We examine two integration methods for integrating this ordinary differential equation to its steady state solution. In the first method we integrate the $f(y)$ portion using explicit Euler and the $g(y)$ portion using implicit Euler, while in the second method we integrate the $f(y)$ portion using second order Runge-Kutta and the $g(y)$ portion using the Trapezoidal Rule.

These methods yield the following schemes:

$$y^{n+1} = y^n + \Delta\tau\Big(f(y^n) + g(y^{n+1})\Big), \tag{3.18}$$

and

$$\begin{aligned} y^* &= y^n + \Delta\tau\left(f(y^n) + \frac{g(y^n) + g(y^*)}{2}\right), \\ y^{n+1} &= y^n + \Delta\tau\left(\frac{f(y^n) + f(y^*)}{2} + \frac{g(y^n) + g(y^{n+1})}{2}\right). \end{aligned} \tag{3.19}$$

Note that both of these are iterative methods for solving $f(y)+g(y) = 0$. The first procedure is first order accurate in $\Delta\tau$, while the second one is second order accurate in $\Delta\tau$. However neither the order of accuracy in $\Delta\tau$ nor the size of $\Delta\tau$ affects the accuracy of the steady state solution. Also the accuracy as solutions of the ordinary differential equation system is not relevant; only the steady states are significant.

These choices of time-stepping methods are also based on results from the next chapter on RPM that indicate that it is preferable to use an implicit method, so that the eigenvalues of the resultant fixed point iteration are smaller and well-separated.

To investigate the stability of these schemes we use the following test problem:

$$f(y) = \lambda y, \qquad g(y) = \mu y; \qquad \lambda, \mu \in \mathbb{C}. \tag{3.20}$$

Substituting these definitions for f and g into the above iterations gives:

$$y^{n+1} = (1 - \Delta\tau\mu)^{-1}(1 + \Delta\tau\lambda)y^n, \tag{3.21}$$

and

$$y^{n+1} = \left[1 + \frac{\Delta\tau}{2}\left(\lambda + \mu\right) + \frac{\Delta\tau\lambda}{2}\left(1 + \Delta\tau\lambda + \frac{\Delta\tau\mu}{2}\right)\left(1 - \frac{\Delta\tau\mu}{2}\right)^{-1}\right]\left(1 - \frac{\Delta\tau\mu}{2}\right)^{-1} y^n. \tag{3.22}$$

Therefore, for the test problem, the first iteration converges when:

$$\|(1 - \Delta\tau\mu)^{-1}(1 + \Delta\tau\lambda)\| < 1, \tag{3.23}$$

while the second iteration converges when:

$$\left\|\left[1 + \frac{\Delta\tau}{2}\left(\lambda + \mu\right) + \frac{\Delta\tau\lambda}{2}\left(1 + \Delta\tau\lambda + \frac{\Delta\tau\mu}{2}\right)\left(1 - \frac{\Delta\tau\mu}{2}\right)^{-1}\right]\left(1 - \frac{\Delta\tau\mu}{2}\right)^{-1}\right\| < 1. \tag{3.24}$$

Looking at the eigenvalues of the terms in the Navier-Stokes equations, we note that the diffusive terms have negative real eigenvalues, while the advective terms have pure imaginary eigenvalues. Using this information and that we integrate the diffusive terms implicitly and the non-linear advective terms explicitly, we assume that $Im(\mu) \equiv 0$ and $Re(\lambda) \equiv 0$. Now setting $\alpha = Re(\mu)$, and $\beta = Im(\lambda)$, the iterations are stable in the region to the left of the lines shown in figure 3.1.

Both regions extend to infinity, and the boundaries for large α and β are given by $(\beta\Delta\tau)^2 \approx -(\alpha\Delta\tau)^2$, and $(\beta\Delta\tau)^4 \approx -2(\alpha\Delta\tau)^3$ for the first and second methods respectively. However, the stability region for the second order problem stays closer to the imaginary axis. Therefore, it is more efficient to use on systems that have many Hopf bifurcations, such as Taylor-Vortex flow.

To accelerate the speed of convergence to the steady state, the Recursive Projection Method is used, details of which can be found in the next chapter. We also consider the differences in the accuracy of the approximate eigenvalues obtained through RPM whilst using the two methods.

The first iteration can be compared with the matrix that Tuckermann and Barkley [34]

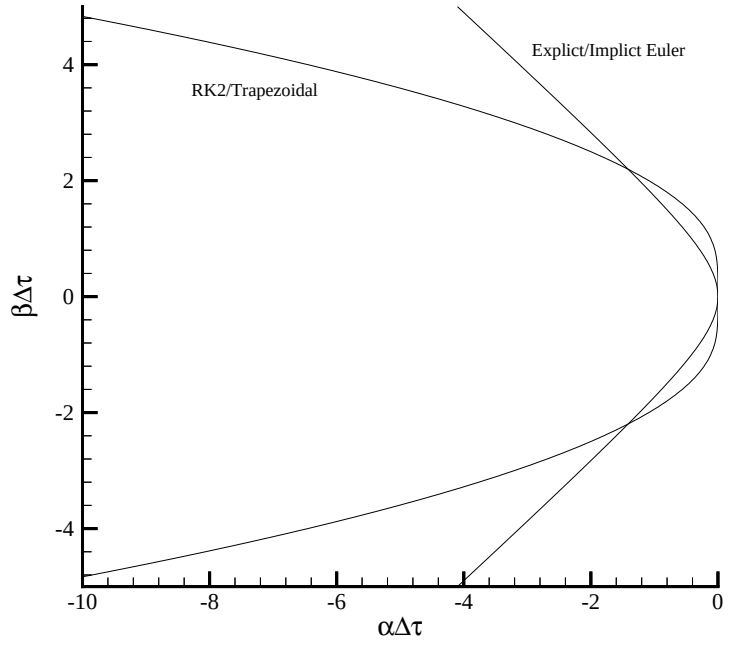

Figure 3.1: Stability Regions for the Iteration Schemes

solve using a conjugate gradient style algorithm. The matrix equation from Tuckerman is

$$[(I - \Delta\tau g_y)^{-1}(I + \Delta\tau f_y) - I]y = [(I - \Delta\tau g(Y))^{-1}(I + \Delta\tau f(Y)) - I]Y, \tag{3.25}$$

where Y is the initial guess and y is the correction. We obtain iteration (3.18) from the above by converting it into the fixed point iteration:

$$(I - \Delta\tau g_y)^{-1}(I + \Delta\tau f_y)y_n - y_{n+1} = [(I - \Delta\tau g(Y))^{-1}(I + \Delta\tau f(Y)) - I]Y. \tag{3.26}$$

The right-hand sides of these equations is just the forcing term $\mathfrak{F}$ from equation (3.16) multiplied with the matrix $(I - \Delta\tau g(Y))^{-1}\Delta\tau$, since:

$$[(I - \Delta\tau g(Y))^{-1}(I + \Delta\tau f(Y)) - I]Y \equiv (I - \Delta\tau g(Y))^{-1}\Delta\tau(f(Y) + g(Y))Y. \tag{3.27}$$

3.5 Parallelization

To improve the speed of these calculations, we implement the algorithm on a distributed memory computer. Information about how to implement numerical methods efficiently on a distributed memory computer can be found in Van de Velde [35].

The main communication between nodes is during the collocation process when we perform a fast Fourier transform, which is a variant of the standard recursive doubling technique. To reduce the amount of communication, the bit reversal part of the fast Fourier transform is not done. This means the physical domain is distributed across the nodes in a bit reversed form.

The only other communication required is by the Recursive Projection Method which needs to compute inner products.

3.6 Obtaining Time Periodic Solutions

Frequently when following steady state branches we encounter Hopf bifurcations. It is more difficult to follow these bifurcating time dependent branches. However, we find that travelling wave solutions also bifurcate and they can be easily followed with the aid of a phase condition.

We explain how we follow branches of travelling wave solutions, then we examine two methods for finding general periodic solutions.

3.6.1 Travelling Wave Solutions

Travelling wave solutions can be easily computed as steady state solutions by changing variables so that we are in a frame of reference that is moving at the same speed as the wave.

For Kolmogorov flow, where we have a travelling wave moving in the x direction, say $u(x, y, z, t) = u(x - ct, y, z)$, we replace the x-momentum equation by

$$\frac{\partial u}{\partial t} = F(u) - c\frac{\partial u}{\partial x}, \tag{3.28}$$

and solve for the steady state solution. The wave speed c is determined by requiring

$$\int_0^{2\pi} u(x,y,z)\frac{du_{k-1}}{dx}(x,y,z)dx = 0, \tag{3.29}$$

where $u_{k-1}(x,y,z)$ is the solution at the previous continuation step. Having introduced a new unknown scalar, c, we can introduce a new scalar constraint and that is how the addition of (3.29) is justified.

When integrating the non-linear differential equation directly, we have an alternative method for determining the wave speed. This is to keep track of the phase of the largest coefficient and to adjust the wave speed so that this phase remains constant.

3.6.2 Discretization In Time

One approach for obtaining general time periodic solutions is to discretize the equations in time as well as in space, and solve the resulting algebraic system. This is the same approach as described in Doedel et al. [12], and used in the AUTO package. However, we discretize in time using Fourier series. We can then find time-periodic solutions by using the same iterative scheme described in sections 3.3 and 3.4.

Since the period of the solution is unknown, we call it T and fix the interval of periodicity by rescaling time using $t \to t/T$ and look for solutions of period 1. The new unknown T is determined by introducing the constraint:

$$\int_0^1 u(t)\frac{du_{k-1}}{dt}(t)dt = 0. \tag{3.30}$$

This phase condition is the same one that is used while following travelling wave solutions, except that the derivative is with respect to time rather than space.

We now study the structure of the eigenvalues of the enlarged system to determine the effectiveness of RPM in accelerating convergence to a solution. For clarity in the following analysis, we use centred finite differencing in time rather than Fourier series.

Lemma 3.1 *Given the ordinary differential equation*

$$\frac{du}{dt} = Au, \tag{3.31}$$

with $A \in \mathbb{C}^{n\times n}$ and $u \in \mathbb{C}^n$. Additionally we assume that A is similar to the diagonal matrix Λ. Assume without loss of generality that the period of the solution to the above ordinary differential equation is $2\pi \equiv m\Delta t$. If λ is an eigenvalue of $A \in \mathbb{R}^{n\times n}$, then $\lambda + \frac{i}{\Delta t}\sin(k\Delta t)$, $k \in \{-m/2, \ldots, m/2\}$ are eigenvalues of:

$$B \equiv \begin{pmatrix} A & I/(2\Delta t) & & & -I/(2\Delta t) \\ -I/(2\Delta t) & A & I/(2\Delta t) & & \\ & \ddots & \ddots & \ddots & \\ & & -I/(2\Delta t) & A & I/(2\Delta t) \\ I/(2\Delta t) & & & -I/(2\Delta t) & A \end{pmatrix} \in \mathbb{R}^{nm\times nm}. \tag{3.32}$$

Proof

Since we assume that A is similar to Λ, we have that B is similar to

$$\begin{pmatrix} \Lambda & I/(2\Delta t) & & & -I/(2\Delta t) \\ -I/(2\Delta t) & \Lambda & I/(2\Delta t) & & \\ & \ddots & \ddots & \ddots & \\ & & -I/(2\Delta t) & \Lambda & I/(2\Delta t) \\ I/(2\Delta t) & & & -I/(2\Delta t) & \Lambda \end{pmatrix}. \tag{3.33}$$

Permuting the rows and columns of this matrix gives a block diagonal matrix. Each block is of the form:

$$\begin{pmatrix} \lambda & 1/(2\Delta t) & & & -1/(2\Delta t) \\ -1/(2\Delta t) & \lambda & 1/(2\Delta t) & & \\ & \ddots & \ddots & \ddots & \\ & & -1/(2\Delta t) & \lambda & 1/(2\Delta t) \\ 1/(2\Delta t) & & & -1/(2\Delta t) & \lambda \end{pmatrix}, \tag{3.34}$$

where λ is an eigenvalue of A.

Now given $k \in \{-m/2, \ldots, m/2\}$, consider the vector

$$\begin{pmatrix} e^{ik\Delta t} & e^{2ik\Delta t} & \ldots & e^{nik\Delta t} \end{pmatrix}^T. \tag{3.35}$$

This is an eigenvector of the preceding matrix, with eigenvalue $\lambda + \frac{i}{\Delta t}\sin(k\Delta t)$.

□

This lemma shows if Jacobian of a differential equation is the same at every point on a periodic solution and we discretize it in time, then the resulting enlarged system has many eigenvalues that cross the imaginary axis simultaneously. Therefore, RPM is ineffective in identifying the bad subspace and in accelerating the convergence to the periodic solution.

In reality for non-linear equations the Jacobian is different at different points on the periodic solution, and the analysis for this case has not been done. However, the preceding lemma is applicable close to the Hopf bifurcation point.

3.6.3 Poincare Map

As suggested by Lust et al. [24], another approach for finding periodic solutions is to find fixed points of the Poincare Return Map, and then use the Recursive Projection Method on the Return Map to accelerate convergence. However, this is only useful in following the first Hopf bifurcation branch, since subsequent branches bifurcating from Hopf bifurcations lie on an invarient torus and do not yield fixed points on the Poincare Map.

Care needs to be taken when accelerating the Poincare map using RPM, since when approximating the Jacobian of the bad subspace using finite differences we have a large round off error as we cannot simply compute the difference directly as in the steady state case, but take the difference of two successive iterates.

A major disadvantage of using the Poincare Return Map is that to obtain accurate solutions requires the use of a high order time stepping method, and a small time step. However, for efficiency reasons, we need a method that allows a large time step. Therefore, we use a second order time stepping method described in section 3.4, and Richardson extrapolation to get enhanced accuracy.

Chapter 4 Recursive Projection Method

The Recursive Projection Method (RPM) invented by Schroff and Keller [32] accelerates the convergence rate of fixed point iterations by using Newton's method on the slowly convergent and unstable subspaces. However, RPM becomes less efficient as the dimension of the unstable subspace increases, or when the eigenvalues of the system are not well separated.

In this chapter we study the performance of RPM when used to help find the solutions of high resolution discretizations of multidimensional partial differential equations. Most previous studies of RPM have only considered its performance on coarse one-dimensional boundary value problems.

Keller and Von Sosen [19] used RPM to accelerate convergence while computing solutions of the Taylor-Vortex flow. Although their calculations were on a three-dimensional grid, their perturbation did not break the symmetry in the azimuthal direction; therefore, many of the eigenvectors were orthogonal to the iterates and hence they were not detected.

A common way to find the steady state solutions of partial differential equations is to integrate them forward in time until they converge. RPM is useful in accelerating this convergence, as well as for enabling convergence to unstable solutions. Moreover, RPM is easily implemented on distributed memory computers that are typically used to solve high resolutions problems. The only additional communication imposed is in the calculation of some inner products.

We use the same RPM algorithm as originally devised by Schroff and Keller, except that we replace the Modified Gram Schmidt orthogonalization with Householder orthogonalization. This change reduces the errors that are generated by the orthogonalization process while updating the unstable subspace and finding the orthogonal basis of the Krylov space.

4.1 RPM Algorithm

Here we give a brief description of the RPM algorithm, full details of which and convergence proofs can be found in Schroff and Keller [32].

Suppose we have the fixed point iteration:

$$x^{(\nu+1)} = G(x^{(\nu)}, \lambda), \tag{4.1}$$

where $G : \mathbb{R}^N \times \mathbb{R} \to \mathbb{R}^N$ is smooth.

Given some $\delta > 0$ we define the unstable subspace $\mathbb{P}$ to be the span of the eigenvectors of G_x that have eigenvalues which lie outside of the disk $K_\delta \equiv \{|z| < 1 - \delta\}$.

We write the space $\mathbb{R}^N$ as the direct sum of the unstable subspace $\mathbb{P}$, and its orthogonal component $\mathbb{Q}$, and introduce the orthogonal projection operators P, and Q, respectively.

Using these projection operators, for each $x \in \mathbb{R}^N$, we have the unique decomposition:

$$x = p + q, \qquad \begin{cases} p \equiv Px \in \mathbb{P}, \\ \dim \mathbb{P} = m, \end{cases} \qquad \begin{cases} q \equiv Qx \in \mathbb{Q}, \\ \dim \mathbb{Q} = N - m. \end{cases} \tag{4.2}$$

It is assumed that $m \ll N$.

Now applying a Lyapunov-Schmidt decomposition to the system $x = G(x, \lambda)$ gives the coupled system:

$$p = f(p, q, \lambda) \equiv PG(p + q, \lambda), \tag{4.3}$$

$$q = g(p, q, \lambda) \equiv QG(p + q, \lambda). \tag{4.4}$$

The idea of RPM is to use Newton's method to solve for p which is in the low dimensional unstable subspace $\mathbb{P}$, and to continue using the fixed point iteration for q. This yields the new iteration:

$$(I - f_p^{(\nu)})(p^{(\nu+1)} - p^{(\nu)}) = f(p^{(\nu)}, q^{(\nu)}, \lambda) - p^{(\nu)}, \tag{4.5}$$

$$q^{(\nu+1)} = g(p^{(\nu)}, q^{(\nu)}, \lambda). \tag{4.6}$$

For efficiency in the computation we introduce coordinate variables z to represent $p \in \mathbb{P}$ with the orthonormal basis Z:

$$z \equiv Z^T p = Z^T u, \qquad z \in \mathbb{R}^m. \tag{4.7}$$

Using these coordinate variables we rewrite (4.5) as

$$(I - Z^T G_x^{(\nu)} Z)(z^{(\nu+1)} - z^{(\nu)}) = Z^T G(x^{(\nu)}, \lambda) - z^{(\nu)}. \tag{4.8}$$

The use of coordinates variables reduces the size of the matrix that we need to invert from $N \times N$ to $m \times m$. This is why we are willing to use Newton's method to compute p.

4.1.1 Addition of Vectors to Unstable Subspace

To determine which vectors should be added to the unstable subspace, we use the Krylov space of the difference of the previous iterates:

$$K \equiv \{\Delta q^{(\nu)}, \Delta q^{(\nu-1)}, \Delta q^{(\nu-2)}, \ldots, \Delta q^{(\nu-k+1)}\}, \qquad \Delta q^{(\nu)} \equiv q^{(\nu)} - q^{(\nu-1)}. \tag{4.9}$$

Schroff and Keller showed that asymptotically Δq lies in the dominant eigenspace of g_q.

We compute the QR factorization of K using Householder transformations, so $K = \hat{K}T$, with $T \in \mathbb{R}^{k \times k}$ upper triangular, and $\hat{K} \in \mathbb{R}^{N \times k}$ orthogonal. We examine the matrix T and if for some i: $|T_{ii}| \gg |T_{i+1i+1}|$ then we add the vectors $\{\hat{K}_1, \ldots, \hat{K}_i\}$, the first i columns of the matrix $\hat{K}$, to the unstable subspace. In our computations we use an acceptance ratio of 80, which gives the test: $|T_{ii}| \geq 80|T_{i+1i+1}|$.

Since all of the vectors in the Krylov space are almost in the same direction, the use of the Householder transformation, instead of the Modified Gram-Schmidt algorithm as originally proposed by Schroff and Keller, means that the orthogonalization is much more accurate.

For RPM to perform efficiently, it needs to be able to identify the unstable subspace quickly. This is only a concern at the beginning of the continuation procedure since we keep the unstable subspace as we progress along the branch. However, on very unstable branches we experience problems starting the continuation procedure. By the time RPM has identified the divergent vectors, the error in the current solution has grown too large.

The size of the acceptance ratio greatly affects how quickly vectors are added to the unstable subspace, especially when the eigenvalues are not well separated. In the following chapter we give an example of how the performance is affected when the acceptance ratio is altered. If the acceptance ratio is too small, then the unstable subspace that is constructed

is not invariant. This causes convergence problems. Conversely if the acceptance ratio is too large, then it takes too many iterations to isolate the vectors to be added.

Increasing the size of the Krylov space improves the speed at which the unstable subspace is constructed, since it allows us to add more vectors simultaneously. Round off errors do not cause a problem with the accuracy of the unstable subspace. The orthogonalized vectors of the Krylov space that are contaminated by round off error are all of the same order of magnitude. Therefore, they do not pass our acceptance test.

During our use of RPM we found occasions when only one vector relating to a complex conjugate pair of eigenvalues is added to the unstable subspace. This causes convergence failure due to the loss of invariancy of the unstable subspace. To correct this problem we use the idea of H.B. Keller to introduce a new test to determine whether the eigenvalues are complex or real.

For large ν the iterates $\Delta q^{(\nu)}$ asymptote to the sum of the eigenvectors of the largest two eigenvalues, λ_1 and λ_2. This gives the equations:

$$\Delta q^{(\nu)} = \lambda_1^2 c_1 + \lambda_2^2 c_2, \tag{4.10}$$

$$\Delta q^{(\nu-1)} = \lambda_1 c_1 + \lambda_2 c_2, \tag{4.11}$$

$$\Delta q^{(\nu-2)} = c_1 + c_2. \tag{4.12}$$

Eliminating c_1 and c_2 from these equations yields the same quadratic equation for either λ_1 or λ_2:

$$\lambda^2 \Delta q^{(\nu-2)} - 2\lambda \Delta q^{(\nu-1)} + \Delta q^{(\nu)} = 0. \tag{4.13}$$

We now take the inner product with $\Delta q^{(\nu)}$, leaving:

$$\lambda^2 \langle \Delta q^{(\nu-2)}, \Delta q^{(\nu)} \rangle - 2\lambda \langle \Delta q^{(\nu-1)}, \Delta q^{(\nu)} \rangle + \langle \Delta q^{(\nu)}, \Delta q^{(\nu)} \rangle = 0. \tag{4.14}$$

This quadratic equation is easily solved for λ:

$$\lambda = \frac{\langle \Delta q^{(\nu-1)}, \Delta q^{(\nu)} \rangle \pm \sqrt{\langle \Delta q^{(\nu-1)}, \Delta q^{(\nu)} \rangle^2 - \langle \Delta q^{(\nu-2)}, \Delta q^{(\nu)} \rangle \langle \Delta q^{(\nu)}, \Delta q^{(\nu)} \rangle}}{\langle \Delta q^{(\nu-2)}, \Delta q^{(\nu)} \rangle}. \tag{4.15}$$

If $\langle \Delta q^{(\nu-1)}, \Delta q^{(\nu)} \rangle^2 < \langle \Delta q^{(\nu-2)}, \Delta q^{(\nu)} \rangle \langle \Delta q^{(\nu)}, \Delta q^{(\nu)} \rangle$ then the two largest eigenvalues are

a complex conjugate pair, so we forbid RPM from only adding one vector to the unstable subspace. We could use the components of any fixed coordinate in (4.13), or several of them, in place of (4.14).

4.1.2 Maintaining Accuracy of Unstable Subspace

As described in Schroff and Keller, while continuing along a branch of solutions the dominant eigenspace of G_x changes. Therefore, we need to periodically update the basis of the unstable subspace. This is achieved by performing one step of a power iteration and then orthogonalizing:

$$Z \leftarrow orth(G_x Z). \tag{4.16}$$

Note that this power iteration is effectively free, since we have already computed $G_x Z$ for the stabilized iteration (4.8).

4.2 Bifurcation Techniques

The use of RPM to detect bifurcations and to provide pseudo arc length continuation was described in the paper by Schroff and Keller. In this section we explore the use of RPM to perform bifurcation theory in the particular case that the fixed point iteration approximates the time integration of a differential equation.

We assume that we are following branches of steady state solutions of the differential equation:

$$\frac{du}{d\tau} = F(u, \lambda). \tag{4.17}$$

To obtain the steady state solutions, we integrate this in time, with a time step of $\Delta\tau$, yielding the fixed point iteration:

$$x_{n+1} = G(x_n, \lambda), \tag{4.18}$$

with $x_n = u(n\Delta\tau)$. RPM is used to accelerate the convergence of this fixed point iteration. The relationship between F and G depends on the method of integration and the size of

$\Delta\tau$. For the moment we assume that the differential equation is integrated exactly in τ.

4.2.1 Detection of Bifurcations

To find the bifurcation points of (4.17), we need to detect when an eigenvalue of F_u crosses the imaginary axis; however, from RPM we obtain an approximation to the dominant eigenvalues of G_x.

Since we assume that we integrate the differential equation exactly, we have the following relation between the eigenvalues γ of F_u and the eigenvalues μ of G_x:

$$\gamma = \frac{\ln \mu}{\Delta\tau}. \tag{4.19}$$

This transformation converts the interior of the unit circle in $\mathbb{C}$, the stability region for a fixed point iteration, into the left half plane, the stability region for a differential equation.

To show an argument for the correctness of the above relation, consider the case when:

$$F(u) \equiv \gamma u. \tag{4.20}$$

Integrating the differential equation (4.17) for this function yields the exact relation:

$$u((n+1)\Delta\tau) = e^{\gamma\Delta\tau} u(n\Delta\tau). \tag{4.21}$$

Now since we had assumed that the fixed point iteration $x_{n+1} = G(x_n, \lambda)$ was obtained by integrating the differential equation exactly, we get that the relationship between the eigenvalues γ of F_u and the eigenvalues μ of G_x is

$$e^{\gamma\Delta\tau} = \mu. \tag{4.22}$$

This is trivally rearranged to give the desired relation (4.19).

However, in reality we are not integrating the differential equation exactly so the locations at which we detect a bifurcation will be perturbed. Additionally the stability regions of our integration methods, see figure 3.1, are not equal to the left plane, the stability region of a differential equation. This also results in altering the locations at which we detect the bifurcation points.

Our time integration differs significantly from previous studies which have used a high order Runge-Kutta method with a small time step. Although this theoretically provides better estimates for the locations of the bifurcation points, it requires a lot more iterations to obtain high resolution solutions.

As also noted in Schroff and Keller, an unstable eigenvector will not be added to the unstable subspace if it is orthogonal to the iterates. This is easily overcome by adding a small random perturbation to the initial guess at the start of every continuation step.

4.2.2 Branch Switching

Once we have detected a bifurcation point, we require a method of switching to the new branch. Since only the right null vectors are available from RPM, we have the option to use either the parallel search or perturbed bifurcation method when switching branches. The other methods for switching branches require knowledge of the left null vectors; however, we are unable to obtain these from RPM unless the matrix G_x is symmetric.

Since we do not know the exact location of the bifurcation points, using the parallel search method may cause convergence problems if our initial guess is too far away from the solution. These problems are avoided when using the perturbed bifurcation technique to switch branches.

Switching branches using the perturbed bifurcation approach involves adding a small perturbation to the system, so we find solutions of $F(u, \lambda) = \epsilon v$, for some v, instead of $F(u, \lambda) = 0$. The effect of this for a generic choice of v is that the branches are broken apart as shown in figure 4.1, where the solid lines are perturbed to the dashed lines. Then

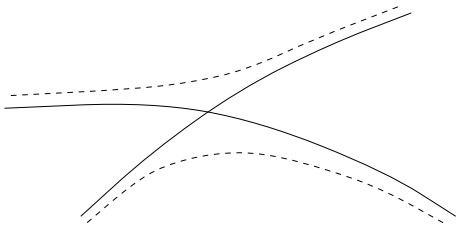

Figure 4.1: Breaking of Branches with Perturbed Bifurcation

we continue in λ past the bifurcation point and remove the perturbation, which leaves a solution of $F(u, \lambda) = 0$ on the other branch.

4.2.3 Augmentation

When the linear system in Newton's method is solved directly, an efficient way for also satisfying constraints that are augmented to the problem is with the bordering algorithm. The bordering algorithm involves solving two or more linear systems which is inefficient when an iterative procedure is used. Additionally the extra systems need to be solved to a high degree of accuracy to prevent truncation errors from affecting the convergence.

Schroff and Keller showed how to implement pseudo arc-length continuation efficiently with RPM by projecting the constraint onto the unstable subspace. Instead of requiring the solution u to satisfy the constraint

$$N(u, u^*, \lambda) = 0, \tag{4.23}$$

we make u satisfy the projection of the constraint onto the unstable subspace:

$$N(Pu, Pu^*, \lambda) \equiv N(p, p^*, \lambda) = 0, \qquad p, p^* \in \mathbb{P}. \tag{4.24}$$

Schroff and Keller did not address what happens when vectors are added to the unstable subspace during the iteration. However, this changes the constraint that is being satisfied, which we take into account in the present work.

We extend this idea to include augmentating with a phase condition, and to the general case where there are many constraints.

Phase Condition

We follow the same idea for augmenting the system as Schroff and Keller. That is we only require that the phase condition is satisfied on the unstable subspace. Lust et al. also use a phase condition but they do not restrict it to the unstable subspace. They introduce an iterative process so that the phase condition is satisfied on the entire space.

Recall from chapter 3 that to determine the wave speed we chose to use the phase condition derived by Doedel [12]:

$$\int_0^{2\pi}\int_0^{2\pi}\int_0^{2\pi} u(x,y,z)\frac{du_{k-1}}{dx}(x,y,z)dxdydz = 0, \tag{4.25}$$

where u_{k-1} is the solution from the previous continuation step. This condition minimizes the distance between two consecutive solution point with respect to translation. The advantages this condition has over the classical orthogonality conditions is that is keeps the sharp fronts or peaks in the same position during the continuation.

Projecting this condition onto the unstable subspace yields:

$$\int_0^{2\pi}\int_0^{2\pi}\int_0^{2\pi} P(u(x,y,z))P(\frac{du_{k-1}}{dx}(x,y,z))dxdydz = 0. \tag{4.26}$$

As in Schroff and Keller the actual computation is done using coordinate variables for the unstable subspace.

Projecting the phase condition onto the bad subspace still produces a convergent iteration for the same reasons as given by Schroff and Keller, namely the restriction of $I - G_x$ to $\mathbb{Q}$, the orthogonal complement to the unstable subspace, is non-singular.

Many Parameter Continuation

RPM is easily adapted to solve problems that have more than one constraint by projecting all of them onto the unstable subspace.

In our numerical experiments we have used two parameters to perform continuation when a travelling wave branch has a fold, a pseudo arc length condition and a phase condition. Both of these constraints are projected onto the unstable subspace; therefore, the Newton iteration inside the RPM algorithm has two additional rows.

The RPM algorithm is easily extended for n constraints, $N^1, \ldots, N^n$, in n unknown parameters, $\lambda_1, \ldots, \lambda_n$, which yields the iteration:

$$q^{(\nu+1)} = g(p^{(\nu)}, q^{(\nu)}, \lambda_1^{(\nu)}, \ldots, \lambda_n^{(\nu)}) + \sum_1^n g_{\lambda_i}^{(\nu)} \Delta\lambda_i^{(\nu)} \tag{4.27}$$

$$\begin{pmatrix} I - f_p^{(\nu)} & -f_{\lambda_1}^{(\nu)} & \ldots & -f_{\lambda_n}^{(\nu)} \\ N_p^1 & N_{\lambda_1}^1 & \ldots & N_{\lambda_n}^1 \\ \vdots & \vdots & \ddots & \vdots \\ N_p^n & N_{\lambda_1}^n & \ldots & N_{\lambda_n}^n \end{pmatrix} \begin{pmatrix} \Delta p^{(\nu)} \\ \Delta\lambda_1^{(\nu)} \\ \vdots \\ \Delta\lambda_n^{(\nu)} \end{pmatrix} = \begin{pmatrix} f(p^{(\nu)}, q^{(\nu)}, \lambda_1^{(\nu)}, \ldots, \lambda_n^{(\nu)}) - p^{(\nu)} \\ -N^1(p^{(\nu)}, \lambda_1^{(\nu)}, \ldots, \lambda_n^{(\nu)}) \\ \vdots \\ -N^n(p^{(\nu)}, \lambda_1^{(\nu)}, \ldots, \lambda_n^{(\nu)}) \end{pmatrix} \tag{4.28}$$

Again, as described in section 4.1, we introduce coordinate variable z to represent the unstable subspace. Therefore, the size of this matrix is only $(m+n) \times (m+n)$, where m is

the dimension of the unstable subspace. Since the size of the matrix is small, we solve the entire linear system directly using LU-decompostion.

4.3 Convergence Behaviour of Solutions Using RPM for Kolmogorov Flow

To study the convergence behaviour of RPM for continuation in Kolmogorov flows, we generally used the secant approximation along the branch to get the initial guess. However, for the higher resolution solutions we simply used the lower resolution solution as the initial guess. The solutions branches and bifurcations are described in detail in the next chapter.

On the following plots the numbers above the lines indicate how many vectors were added to the unstable subspace at that point. Recall from chapter 3 that we use Newton's method to obtain the solution, and for each Newton step we use an iterative procedure to determine the correction. The different lines on each plot correspond to the different Newton steps that were used in calculating the solution. Each Newton step was stopped when the residual norm of the correction had been reduced by a factor of 10^{-4}.

The typical convergence behaviour when a vector is added to the unstable subspace of RPM is that there is a large drop in the error. An example of this behaviour is shown in figure 4.2, which is computed on branch A, see figure 5.7, at $\Omega/\Omega_c = 2.20$. Further examples of the standard RPM behaviour can be seen in most of the following plots.

Additionally we notice in figure 4.2 that there is a large drop in the residual error at the beginning of the second Newton step since we keep the unstable subspace from the first step. Since we keep the unstable subspace between steps, we do not waste effort in determining it again and therefore we achieve faster convergence for the second Newton step.

In addition to keeping the unstable subspace for the different Newton steps, we use an updated version of the unstable subspace at the subsequent continuation steps. In figures 4.3 and 4.4 we show the convergence plots while continuing along branch G; see figure 5.16. In this case we kept the unstable subspace from our calculation of the solution at $\Omega/\Omega_c = 3.20$, updated it with a power iteration and used it to help compute the solution at $\Omega/\Omega_c = 3.40$.

Some unusual behaviour occurred during the second Newton step to find the solution at $\Omega/\Omega_c = 3.40$, figure 4.4. When a vector was added to the unstable subspace, we observed

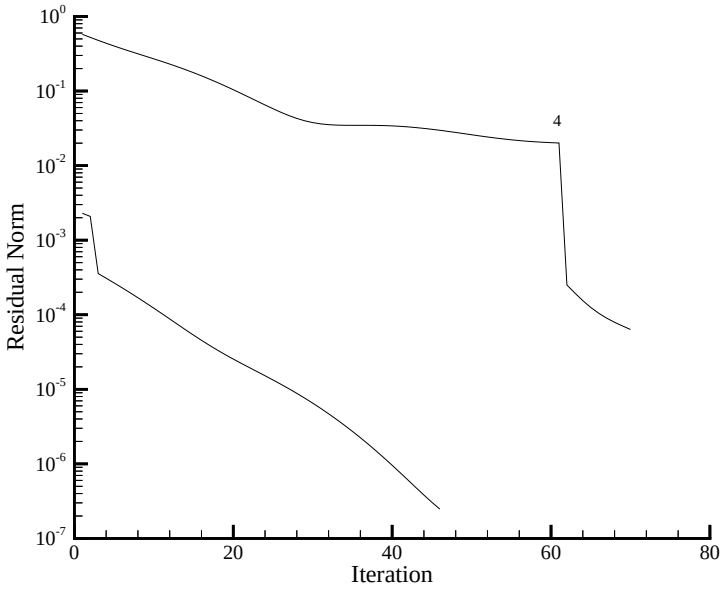

Figure 4.2: Convergence on branch A at $\Omega/\Omega_c = 2.20$

that the residual norm increased. The first increase was due to RPM adding an inaccurate vector to the unstable subspace. The resulting loss of invariancy caused a failure in convergence. However, shortly afterwards the invariancy was restored with the addition of another vector. Unfortunately, by this point the error in the current solution was relatively large so a large correction to the solution was required. Although this reduced the error, it increased the residual norm. After this point we see that the residual norm is decaying faster than before the first vector was added.

To compute solutions along branch Gt, which is similar to branch G, see figure 5.16, we need to augment the system with a phase condition to determine the wave speed; see section 4.2.3. The convergence for branch Gt at $\Omega/\Omega_c = 3.20$ is shown in figure 4.5.

We also observed an increase in the residual norm after vectors are added to the unstable subspace. This was due to the error of the current solution being too large. The large error is mainly due to the phase condition that we imposed. This condition changes when vectors are added to the unstable subspace.

The error jump can be observed in figure 4.6 where we plot the computed wavespeed correction during the second Newton step. At the position where a vector is added to the

unstable subspace, we see a large jump in this wavespeed correction.

In figure 4.7 we show the convergence for the same Ω/Ω_c value on branch Gt but the wavespeed fixed. We still get slight increases when vectors are added to the unstable subspace this is again due to the current solution being relatively far away from the correct value. Compare figures 4.5 and 4.7.

Figure 4.8 shows the convergence for branch H, see figure 5.17, at $\Omega/\Omega_c = 4.00$. After about 40 iterations we see that the scheme is becoming unstable. However, RPM detects the divergent subspace, corresponding to a pair of complex conjugate eigenvalues, adds two vectors to the basis and thereby regains convergence.

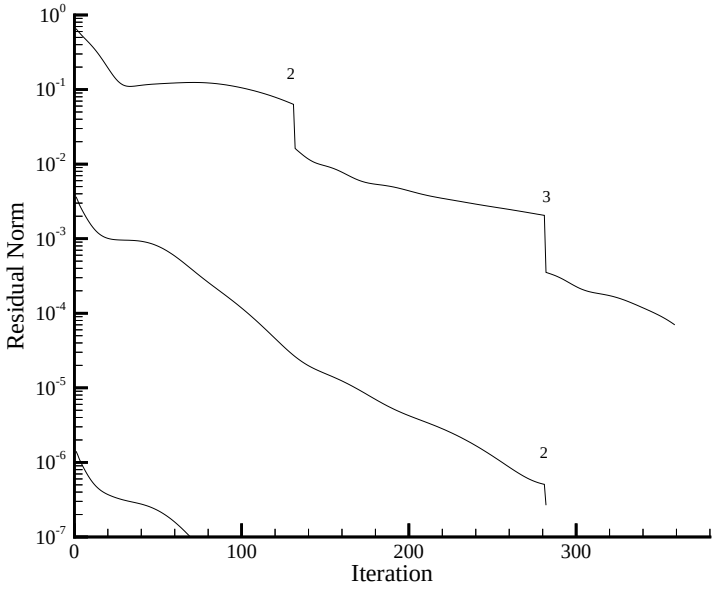

Figure 4.3: Convergence on Branch G at $\Omega/\Omega_c = 3.20$

Figures 4.9 and 4.10 also show increases in the residual norm when vectors are added to the unstable subspace. These figures are computed on branch J at $\Omega/\Omega_c = 4.70$. However, another vector is quickly identified and added to the unstable subspace to cause the residual to decrease significantly. This occurs when RPM adds only one vector relating to a pair of complex conjugate eigenvalues into the unstable subspace. The effect of this is that the unstable subspace is no longer invariant and does not contain the basis for the two-dimensional space corresponding to the complex eigenvalues, thus causing a loss

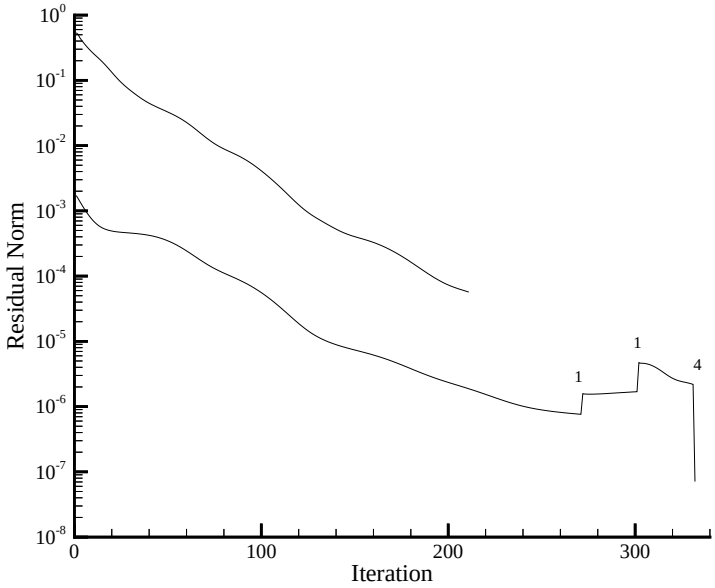

Figure 4.4: Convergence on Branch G at $\Omega/\Omega_c = 3.40$

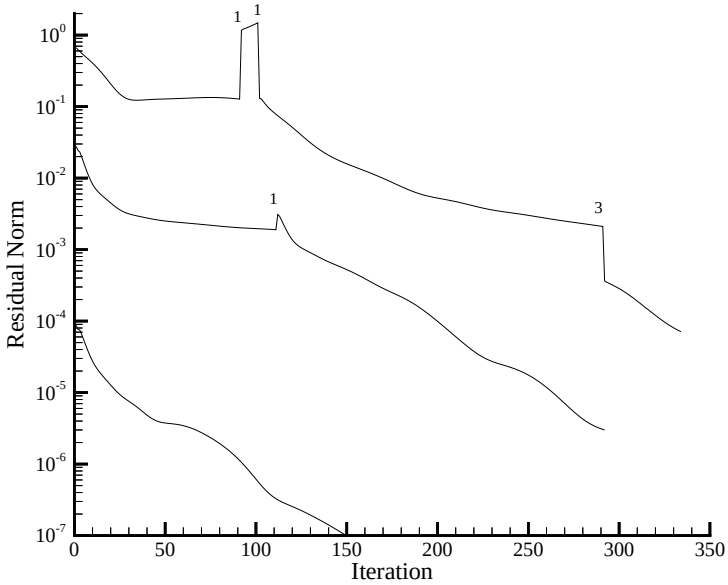

Figure 4.5: Convergence on Branch Gt at $\Omega/\Omega_c = 3.20$ Using the Phase Condition to Determine the Wave Speed

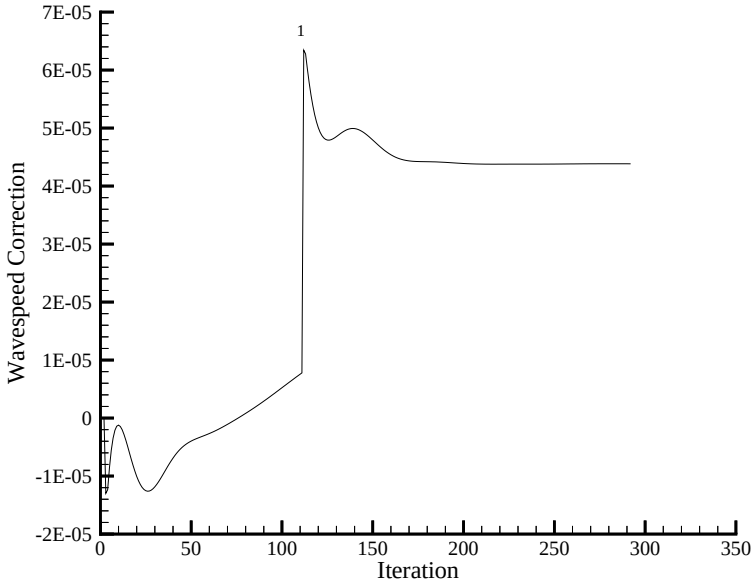

Figure 4.6: Convergence of Wavespeed Correction on Branch Gt at $\Omega/\Omega_c = 3.20$ During the Second Newton Step Using the Phase Condition to Determine the Wave Speed

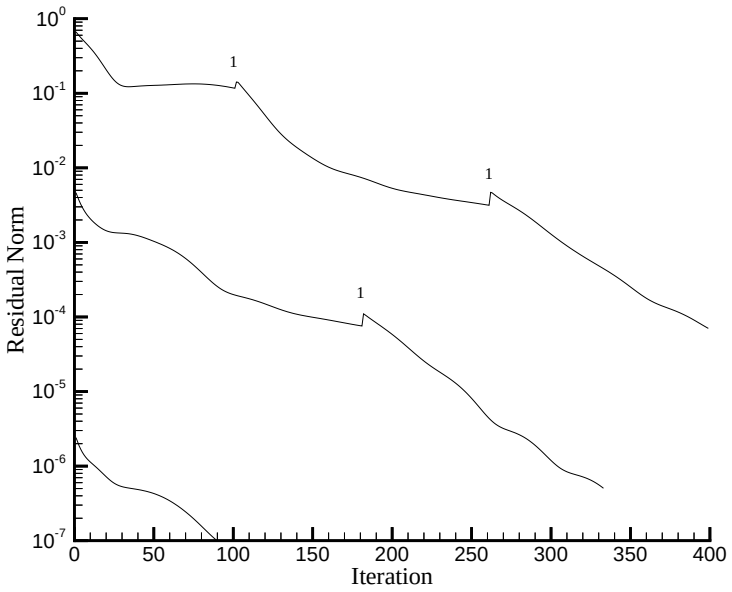

Figure 4.7: Convergence on Branch Gt at $\Omega/\Omega_c = 3.20$ With the Wave Speed Fixed at the Known Value

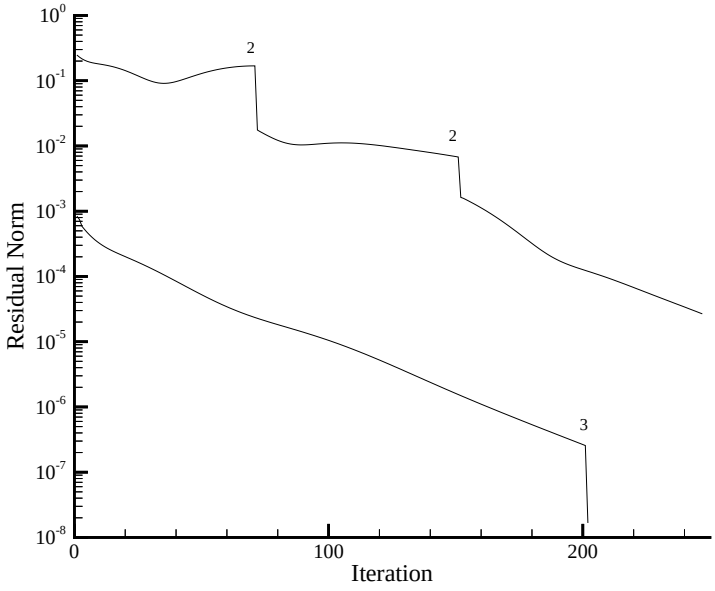

Figure 4.8: Convergence on Branch H at $\Omega/\Omega_c = 4.00$

of convergence. However, due to this RPM isolates a second vector quickly and recovers convergence.

To correct this problem we test the dominant eigenvalues, as described in section 4.1.1, to determine whether they are real or a complex conjugate pair. With this test we do not allow RPM to add only one vector when we have a complex conjugate pair of eigenvalues. However, the vectors of the Krylov subspace are not accurate enough for this test to work.

In section 3.4 we considered two methods for integrating an ordinary differential equation, a first order accurate implicit/explicit Euler method, and a second order accurate Runge-Kutta/Trapezoidal rule. Figures 4.9 and 4.10 show the difference in performance between these two methods. We observe from these figures that the Runge-Kutta/Trapezoidal rule method requires fewer iterations, which is due to the larger time step that we are able to use. However, each iteration requires twice as much work compared with the implicit/explicit Euler method. The higher order accurate method seems more efficient.

Figure 4.11 is also computed using the Runge-Kutta/Trapezoidal rule; however, it uses a larger Krylov space. This larger Krylov space allows more vectors to be added to the unstable subspace simultaneously. On the first Newton step of figure 4.10, six vectors

are added in quick succession, whereas with the larger Krylov space they are all added simultaneously. The benefits of using a larger Krylov space are more apparent when the eigenvalues of the system being solved are not well separated.

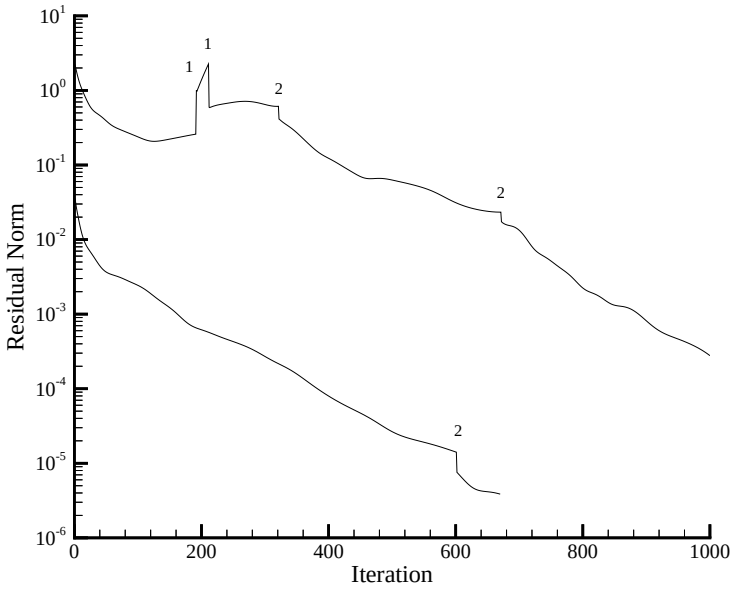

Figure 4.9: Convergence on Branch J at $\Omega/\Omega_c = 4.70$ Using Euler Time Stepping

Figures 4.12 and 4.13 show the convergence plots while continuing along the three-dimensional flow of branch S, at $\Omega/\Omega_c = 6.50$, and $\Omega/\Omega_c = 7.00$ respectively. (Branch S is similar to branch K, figure 5.4, except it has twice as many modes in the x and z directions.) These figures show that it takes a few continuation steps for RPM to detect all of the vectors to be included in the unstable subspace. Figure 4.13 shows a good example of RPM detecting divergent vectors on the second Newton step. These vectors are added to the unstable subspace which results in the iteration regaining its stability.

In figures 4.12, 4.14 and 4.15 we show the convergence for the solution of branch S at $\Omega/\Omega_c = 6.50$ using 32, 64 and 128 modes respectively. The calculations for the 64 and 128 mode solutions used the 32 mode solution, instead of a secant approximation, as the initial guess. We note that the convergence plots of the 64 and 128 modes solutions are the same. This is due to performing the same time integration from the same initial guess at both resolutions. Additionally we were able to keep the time step the same at all resolutions.

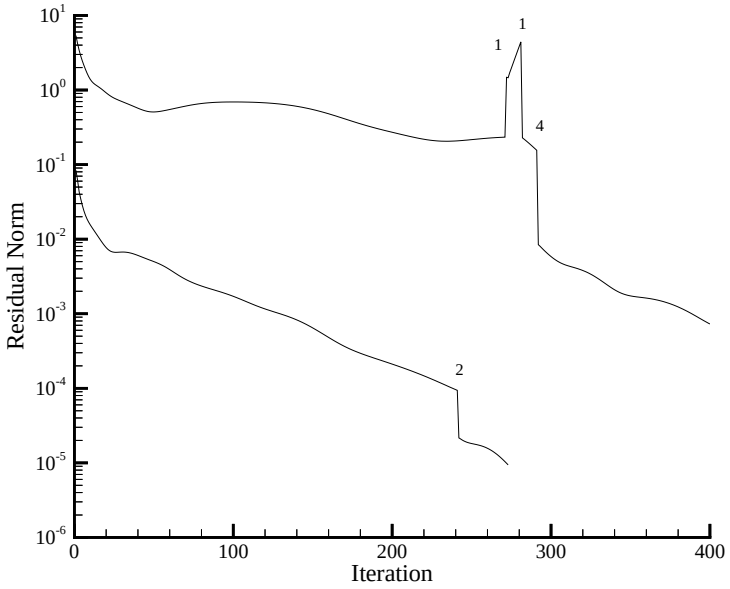

Figure 4.10: Convergence on Branch J at $\Omega/\Omega_c = 4.70$ Using Second Order Runge-Kutta With Krylov Space Size=6

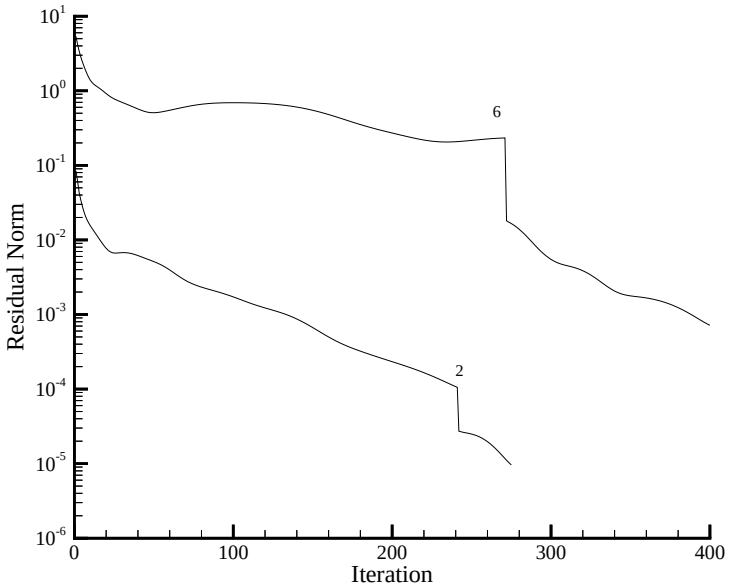

Figure 4.11: Convergence on Branch J at $\Omega/\Omega_c = 4.70$ Using Second Order Runge-Kutta With Krylov Space Size=8

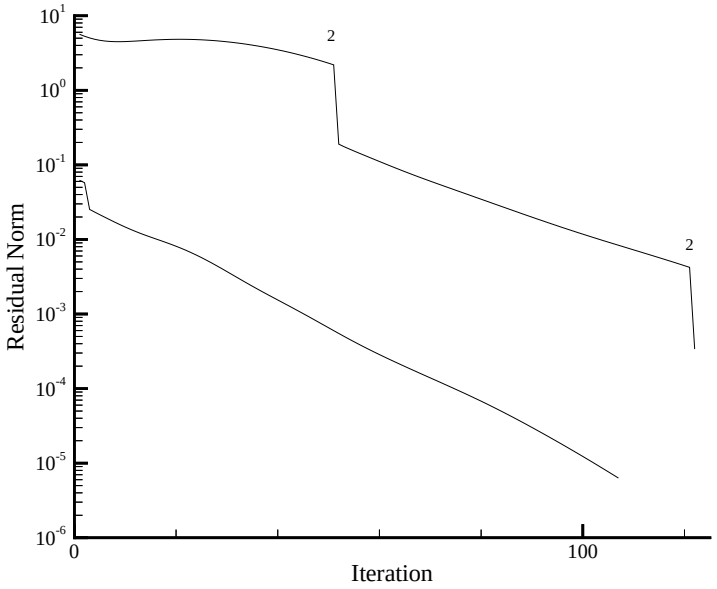

Figure 4.12: Convergence on Branch S at $\Omega/\Omega_c = 6.50$

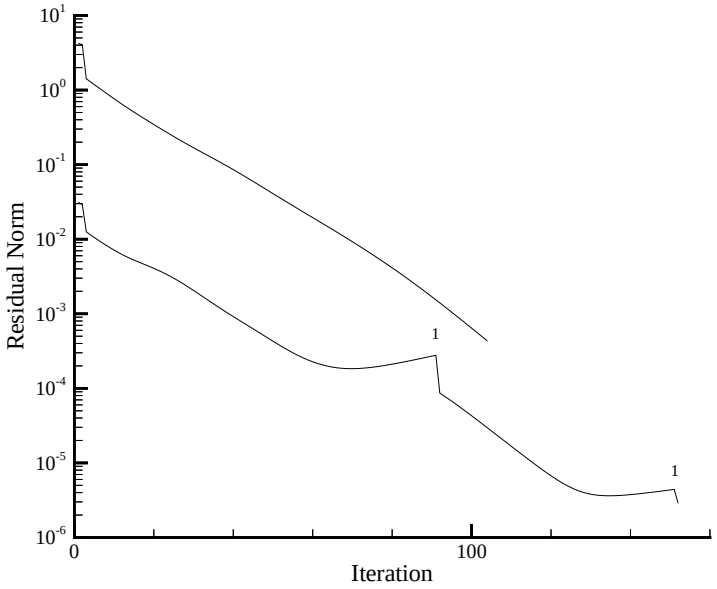

Figure 4.13: Convergence on Branch S at $\Omega/\Omega_c = 7.00$

This shows that the higher wavenumber modes do not effect the convergence of our scheme, although using them still produces a substantial improvement in the accuracy of the solution. Note that if we had used an explicit time stepping method to keep the iteration stable, we would have needed to reduce the time step for the higher resolution solutions.

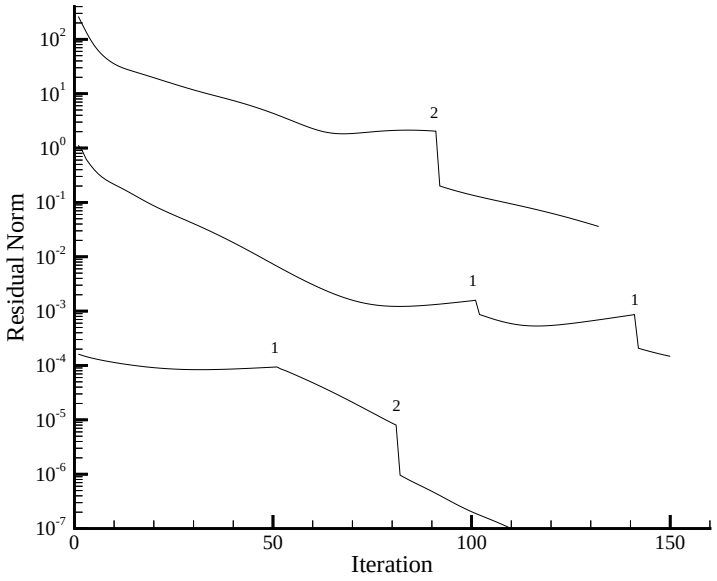

Figure 4.14: Convergence on Branch S at $\Omega/\Omega_c = 6.50$ With 64 Modes in Each Direction

4.4 Convergence Behaviour of Solutions Using RPM for Taylor Vortex Flow

For Taylor Vortex flow we observe the same behaviour as in Kolmogorov flow. The Taylor-Vortex solutions and bifurcations are described in chapter 7. The convergence while continuing along the Taylor-Vortex branch is shown in figures 4.16 and 4.17. Keeping the unstable subspace at the end of one Newton step yields sharp drops in the residual norm at the beginning of the next Newton step.

We also examine the effect on convergence rate when calculating higher resolution solution of the Taylor-Vortex flow; compare figures 4.16 and 4.18. When we increase the radial resolution we need to make a reduction in the time step to maintain stability. We see

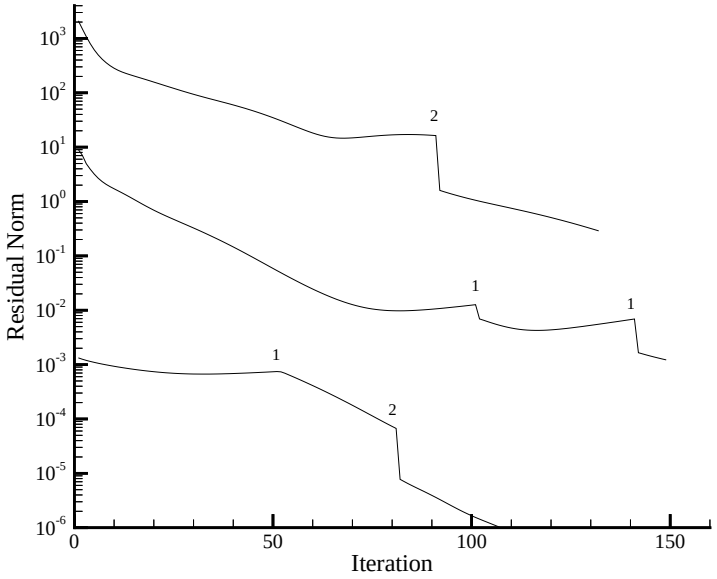

Figure 4.15: Convergence on Branch S at $\Omega/\Omega_c = 6.50$ With 128 Modes in Each Direction

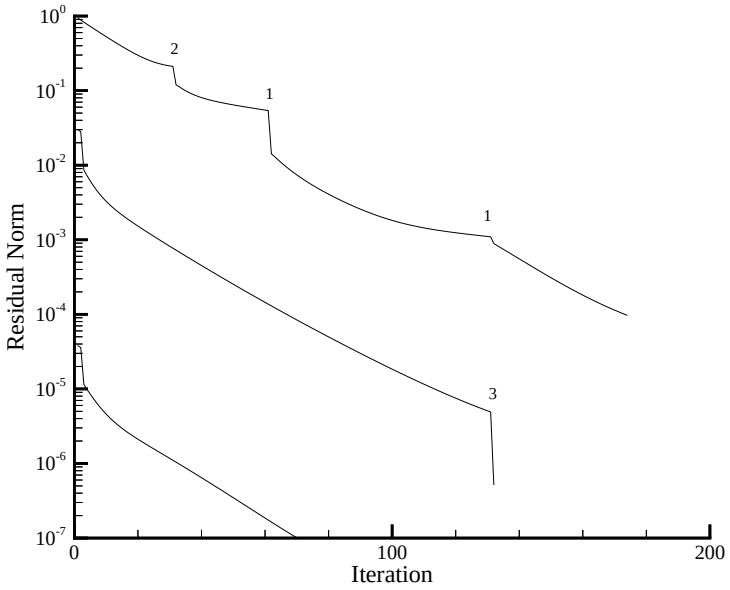

Figure 4.16: Convergence on Taylor Vortex Flow Branch at $Re = 140$, q=4, With 32 Radial Points

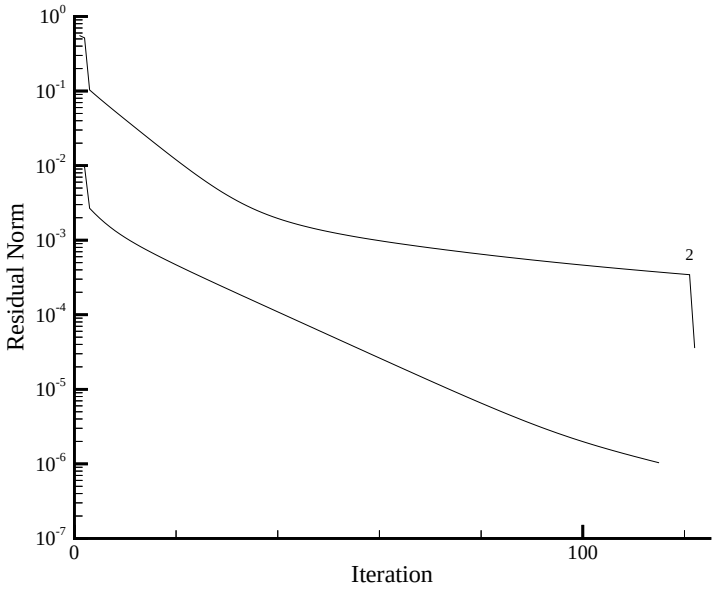

Figure 4.17: Convergence on Taylor Vortex Flow Branch at $Re = 145$, q=4, With 32 Radial Points

that the number of iterations also increases, and recall that each iteration takes more computational effort. For Kolmogorov flow, with periodic boundary conditions, the increased resolution did not require smaller timesteps.

When computing the solution for Wavy Taylor Vortex branches, we see an increase in the residual norm just as in computing travelling wave solutions of Kolmogorov flow. These increases occur for the same reason as before. A phase condition is introduced and the error is relatively large since the phase condition changes when vectors are added. The large error is indicated in figure 4.20; a large jump in wavespeed occurs when vectors are added at iteration 100.

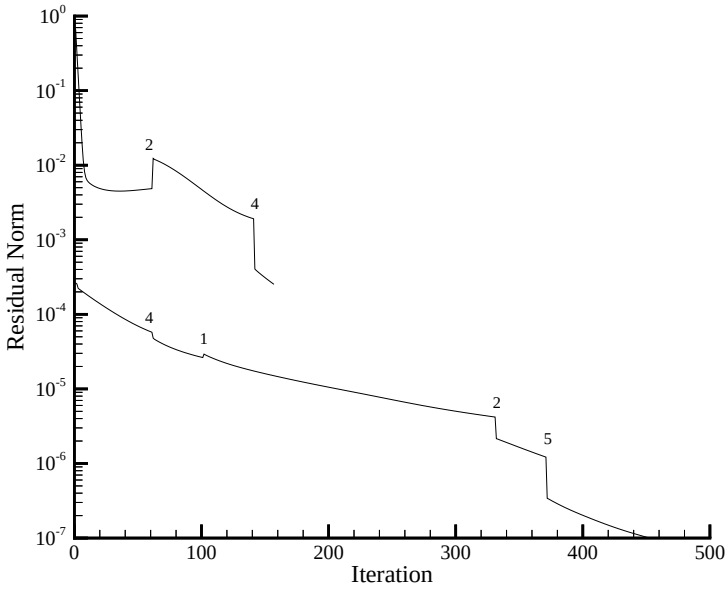

Figure 4.18: Convergence on Taylor Vortex flow branch at $Re = 140$, q=4, with 64 radial points

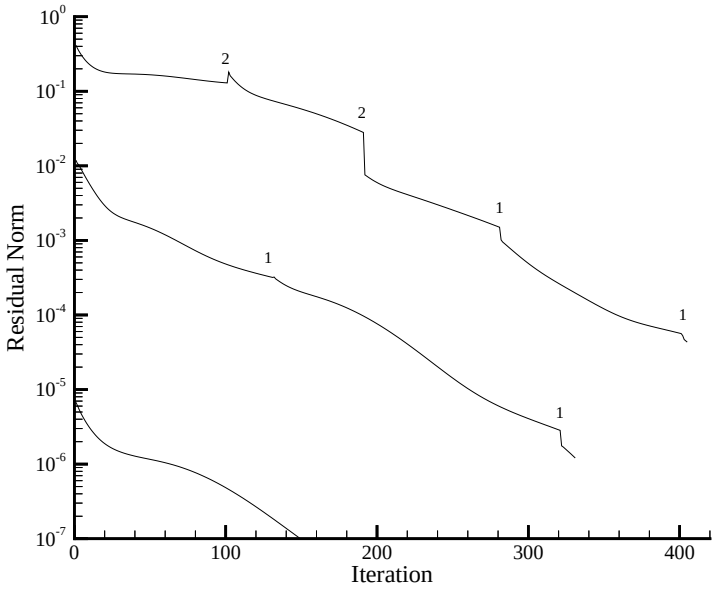

Figure 4.19: Convergence on Wavy Taylor Vortex Flow Branch at $Re = 200$, q=4, With 32 Radial Points

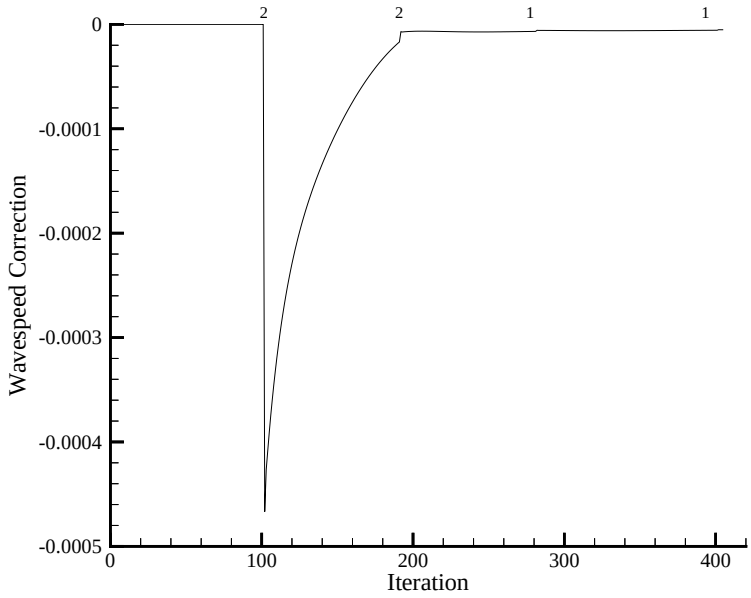

Figure 4.20: Convergence of Wavespeed Correction on Wavy Taylor Vortex Flow Branch at $Re = 200$, q=4, With 32 Radial Points, During the First Newton Step

Chapter 5 Continuation Results for Kolmogorov Flow

We use the methods described in chapters 3 and 4 to find the various solution branches of Kolmogorov flow. In the next chapter we compare the statistics of the solutions from some of these branches to those obtained from turbulence calculations.

5.1 Bifurcations from Shear Flow

Bifurcations from branches of solutions of the Navier-Stokes equations occur when an eigenvalue of the linearized system crosses the imaginary axis as the parameter value is varied. As described in chapter 4, we use the Recurrsive Projection Method to approximate these eigenvalues.

The major error in the eigenvalues obtained through RPM originates from adding eigenvectors before the Krylov space approximation of them is accurate enough. The accuracy of the unstable subspace is monitored by evaluating the matrix:

$$\varepsilon \equiv QF_u^*P, \tag{5.1}$$

which vanishes for exact eigenvectors determining P and Q.

The accuracy is increased by increasing the acceptance ratio which, as described in chapter 4, is used to decide if a vector of the orthogonalized Krylov space is to be added to the unstable subspace of RPM.

Figures 5.1 and 5.2 show the eigenvalues obtained while continuing along the shear flow solution branch. Figure 5.1 has an acceptance ratio of 80, while in figure 5.2 the acceptance ratio is 200. These figures show that the locations at which the eigenvalue traces cross the axis are within one continuation step of the analytical bifurcation results shown in table 2.1.

The obvious discontinuity in the graphs is due to the continuation being stopped and then restarted at $\Omega/\Omega_c = 3.0$. At this restart point the difference between these two plots

is most noticeable. We observe that with an acceptance ratio of 200 the traces of multiple eigenvalues start closer together.

This was to observe the performance of RPM in starting continuation at an unstable location of a branch. Notice that some eigenvalue traces do not restart immediately after this discontinuity, because it takes a few continuation steps to obtain all of the divergent eigenvalues since some of the eigenvectors are orthogonal to each other and we converge to the solution before RPM has had time to detect all of them. Additionally we find that the accuracy of the invariant subspace for those eigenvectors with eigenvalues greater than zero is approximately ten times that of the remaining eigenvectors. In figures 5.1 and 5.2 we see that an effect of greater accuracy is that the eigenvalue traces for positive eigenvalues are more clearly defined.

The discontinuites in some of the eigenvalue traces, as they approach the axis, are due to the eigenvectors not being accurate enough. This manifests itself most prominently when the eigenvalues are near zero. A good example of this can be seen in figure 5.1 at $\Omega/\Omega_c \approx 2.3$, where we see eigenvalues traces disappearing as they approach the axis. In this situation RPM detects that the iteration is not converging and adds additional vectors to the unstable subspace.

Due to the translation invariance in the Navier Stokes equations and the shear flow solution, at a bifurcation point multiple real eigenvalues change sign. The eigenvectors corresponding to a multiple eigenvalue are the same except that they are translated in the x and/or z directions. When a two-dimensional branch bifurcates, such as the one shown in figure 5.3, two real eigenvalues change sign. Whereas for a three-dimensional branch, such as that shown in figure 5.4, four real eigenvalues change sign.

In figures 5.1 and 5.2 we notice that there are eigenvalue that are close together. These are actually multiple eigenvalues, but due to various errors they split in the calculations. However, as the continuation progresses the approximations converge to the same value.

Figure 5.3 shows the bifurcated solution which has one wave in the x direction near its bifurcation point. We compare the two-dimensional bifurcating solution, figure 5.3, to the three-dimensional bifurcating solution, figure 5.4. The three-dimensional solution has layers that look similar to the two-dimensional flow interspersed with shear flow layers.

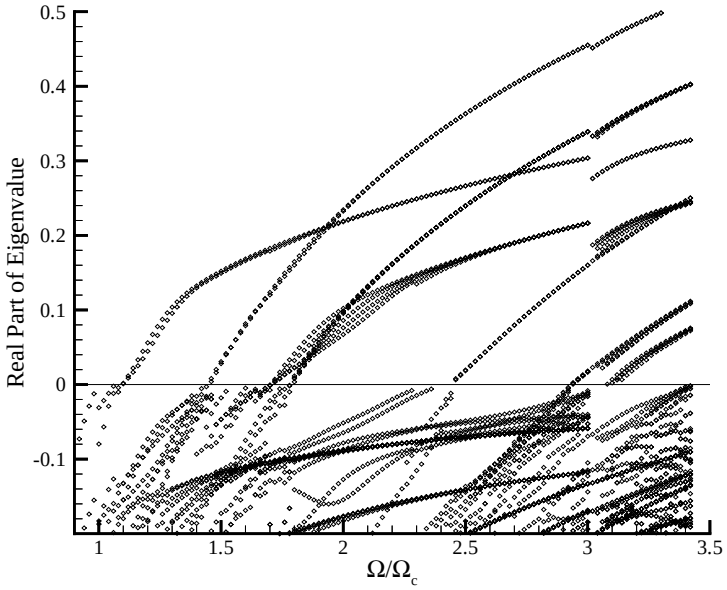

Figure 5.1: Eigenvalues of the Shear Flow, Acceptance Ratio=80

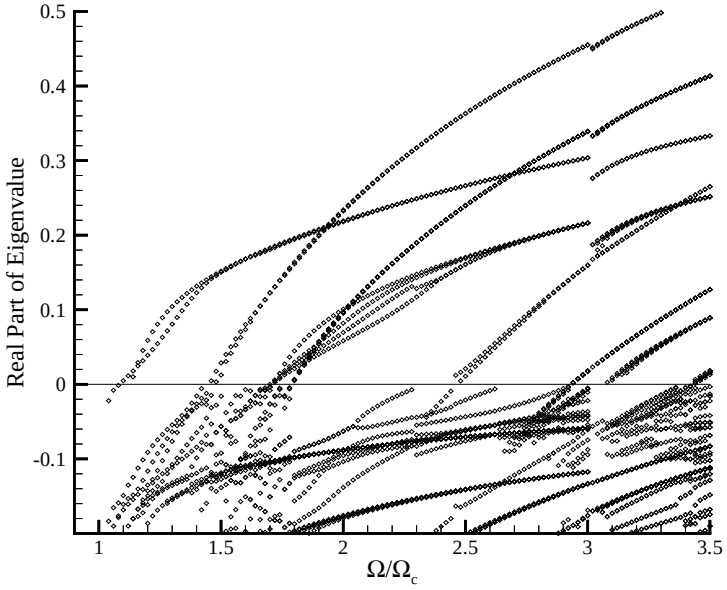

Figure 5.2: Eigenvalues of the Shear Flow, Acceptance Ratio=200

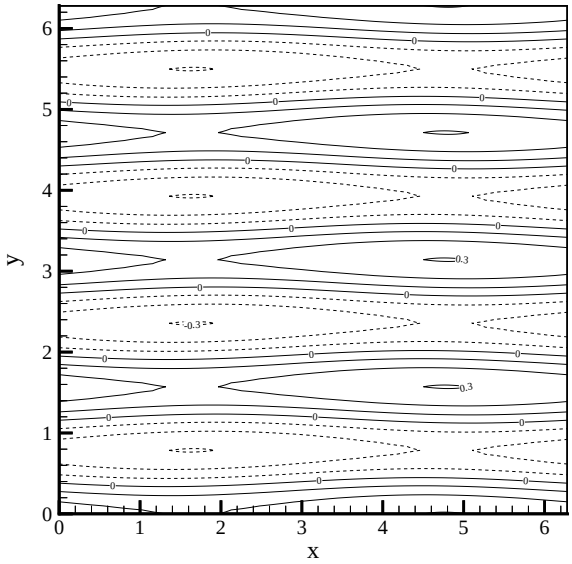

Figure 5.3: Streamfunction: Branch A at $\Omega/\Omega_c = 1.10$

5.2 Accuracy of Solutions

We compare the accuracy of the solutions obtained from using different numbers of Fourier modes to determine the optimal number of modes to use to get the most efficient accurate solutions. Since we are integrating the diffusive term using an implicit method, we are able to use the same time step for each resolution, therefore obtaining the solution at each resolution required approximately the same number of iterations.

In tables 5.1 and 5.2 we show how the error reduces as the number of modes is increased, for branch R at $\Omega/\Omega_c = 5.0$ and branch Gt at $\Omega/\Omega_c = 50.0$, respectively. When calculating the errors we use as the "exact" solution, the 128 mode numerical solution.

Modes	2-Norm	Error in Norm
16	0.577230584301	2.44×10^{-3}
32	0.574713737592	7.97×10^{-5}
64	0.574793408635	9.86×10^{-10}
128	0.574793409621	

Table 5.1: Convergence of Kolmogorov Solutions on Branch R at $\Omega/\Omega_c = 5.0$

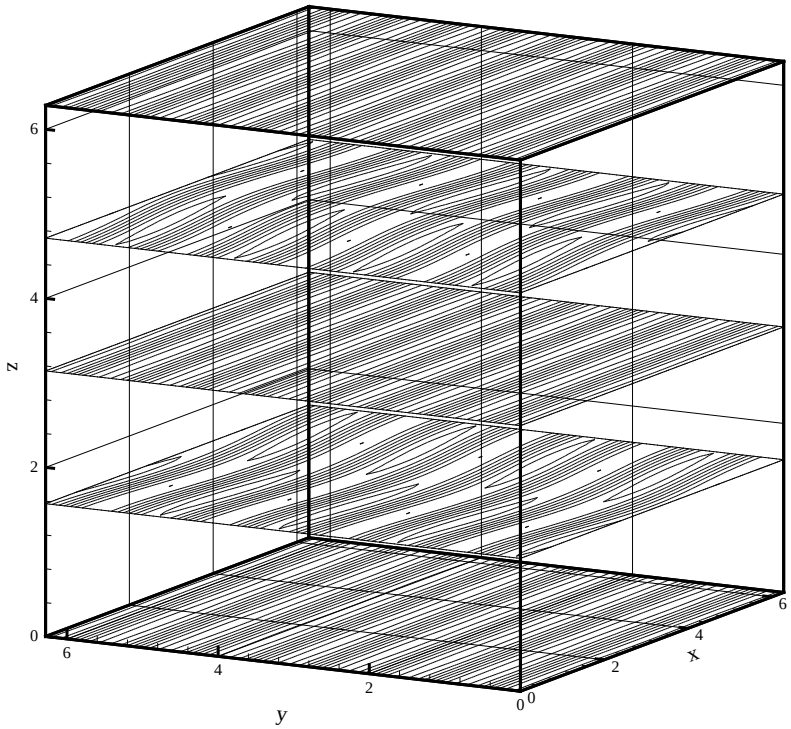

Figure 5.4: z Direction Vorticity: Branch K at $\Omega/\Omega_c = 1.80$

Modes	2-Norm	Error in Norm	Wavespeed	Wavespeed Error
32	0.334950931635	1.34×10^{-3}	0.00153153086037	2.79×10^{-5}
64	0.333615163732	4.44×10^{-7}	0.00155925852322	2.18×10^{-7}
128	0.333615607799		0.00155947682411	

Table 5.2: Convergence of Kolmogorov Solutions on Branch Gt at $\Omega/\Omega_c = 50.0$

These tables show that the error decreases exponentially as the resolution is increased, indicating that discretization is spectrally accurate.

We observe that 32 modes gives good accuracy especially at the lower Reynolds numbers. Ideally 64 modes should be used to get very accurate results; however, there is additional work required to obtain this more accurate solution. We could not get the 16 mode solution to converge on branch Gt at $\Omega/\Omega_c = 50.0$, using the 32 mode solution as the initial guess.

To examine the convergence in greater detail in figures 5.5 and 5.6, we plot the engergy spectrum function:

$$E(k) \equiv \frac{1}{2} \sum_{k-1/2<|\hat{k}|<k+1/2} |u_{\hat{k}}|^2. \tag{5.2}$$

The energy spectrum function is used more in chapter 6 where we use it to compare our solutions with those from turbulence calculations.

These plots jiggle because we only compute the energy spectrum function at integer values. These figures have a different jiggle frequency because figure 5.5 is for branch R, which has not had a y-symmetry breaking bifurcation and therefore the dominant wavenumbers are multiples of the forcing frequency.

The energy associated with each wavenumber remains almost exactly the same for each resolution, until the wavenumber is larger than two-thirds of the largest wavenumber for the least number of modes. This corresponds with our anti-aliasing technique where we set the largest third of the wavenumbers of the non-linear advective term equal to zero. From these figures we find that the energy exponentially decreases with wavenumber, which again indicates that our solutions have spectral accuracy.

By comparing the errors in tables 5.1 and 5.2, we observe that at higher Reynolds numbers our solutions become less accurate. This can also be seen by comparing the energy spectrum functions for both of these solutions. For the higher Reynolds number solution there is more energy associated with the higher wavenumbers but some energy is lost at the lower resolutions.

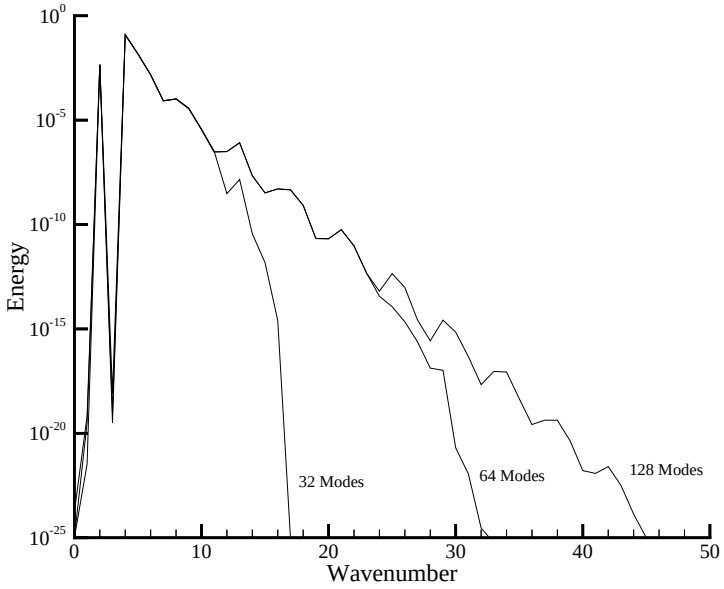

Figure 5.5: Energy vs. Wavenumber for Various Resolutions, Branch R, $\Omega/\Omega_c = 5.0$

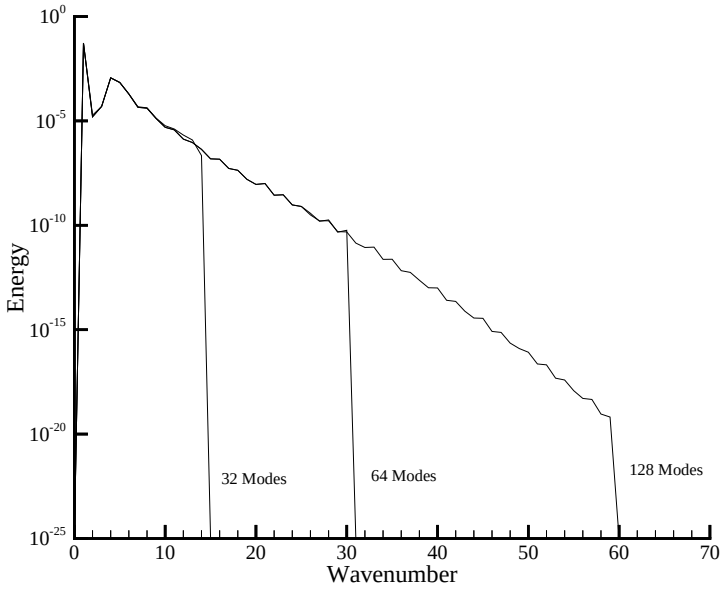

Figure 5.6: Energy vs. Wavenumber for Various Resolutions, Branch Gt, $\Omega/\Omega_c = 50.0$

5.3 Continuing Along the Bifurcating Branches

Continuing along the two-dimensional branches that bifurcate from the shear flow, figures 5.7 and 5.8, we observe that as the Reynolds number is increased, the flow changes from being mainly horizontal to mainly vertical. This was also observed by Platt and Sirovich, and agrees with the experimental results of Bondarenko et al. [6].

Again we use the approximations of the eigenvalues given by RPM to approximate the locations of the bifurcating branches. These secondary bifurcations are categorized into a number of different forms depending on what is the largest mode of the null vector.

A large number of the branches we followed are unstable. The full bifurcation diagram is shown in figure 5.9, and the locations of the bifurcation points are listed in table 5.3. Figure 5.10 shows a pictorial representation of the bifurcation diagram to make it easier to understand the structure of the bifurcations.

During the remainder of this chapter, we explain the bifurcations to the different branches and the transitions between various solutions observed by Platt and Sirovich. However, Platt et al. started the calculation for each Reynolds number at a perturbed shear flow; therefore, the solution they obtained also depends on the domain of attraction, in addition to the stability of the solution. The initial condition they used for all their calculations was

$$u_0 = \frac{1}{\Omega}\left(\sin(4y) + 10^{-4} \sum_{m_1,m_2\leq 0} \frac{m_2}{\sqrt{m_1^2+m_2^2}}[\cos(m_1x+m_2y) - \sin(m_1x+m_2y)]\right), \quad (5.3)$$

and the y velocity is such that this initial condition is divergence free. The domain of attraction for a particular steady state solution is the set of all initial conditions for the partial differential equation that converge to that particular solution as you integrate in time.

This is not an effective method of determining the nature of the bifurcations since it does not give a clear explanation of where a branch bifurcates from. Additionally it requires more computational effort since the initial guess is far away from the solution.

Platt et al. observed that the solution they obtained suddenly changed from branch A to branch B at $\Omega/\Omega_c = 1.97$. This location corresponds to the Reynolds number on branch B where the solutions become stable when branch D, figure 5.11, bifurcates from it.

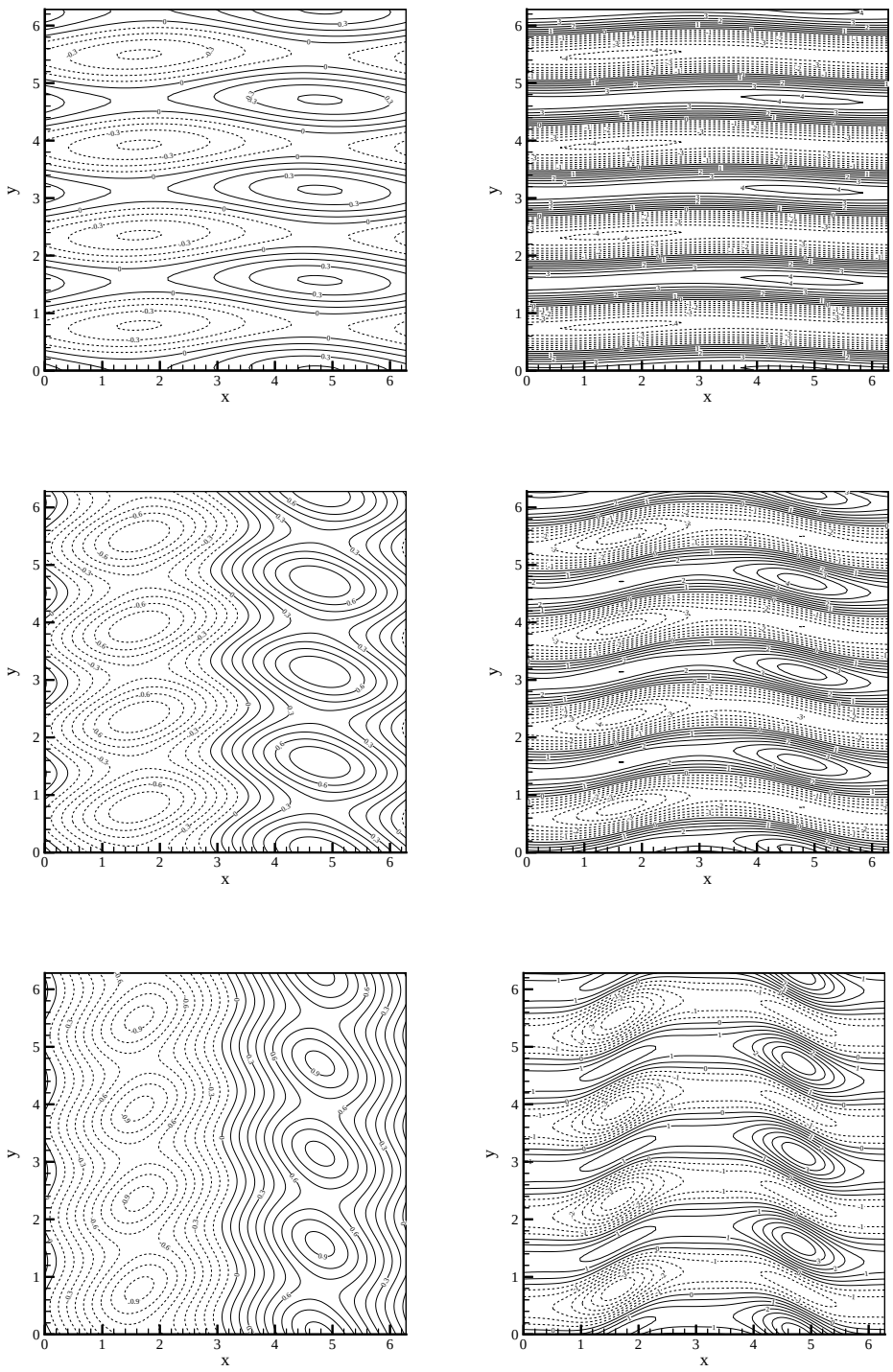

Figure 5.7: Streamfunction (Left) and Vorticity: Branch A at $\Omega/\Omega_c = 1.12, 1.50, 3.00$, From Top to Bottom

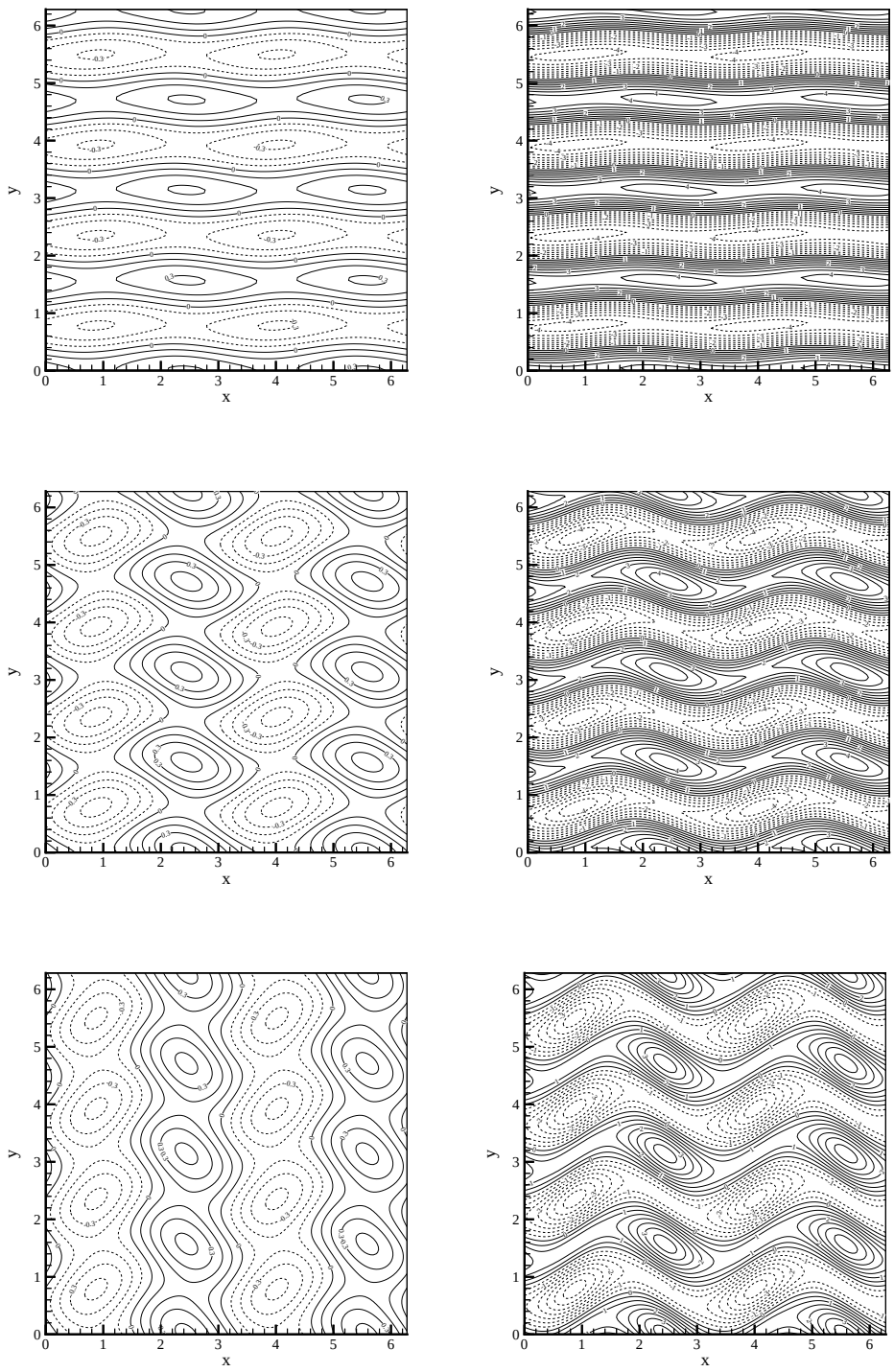

Figure 5.8: Streamfunction (Left) and Vorticity: Branch B at $\Omega/\Omega_c = 1.45, 2.00, 4.00$, From Top to Bottom

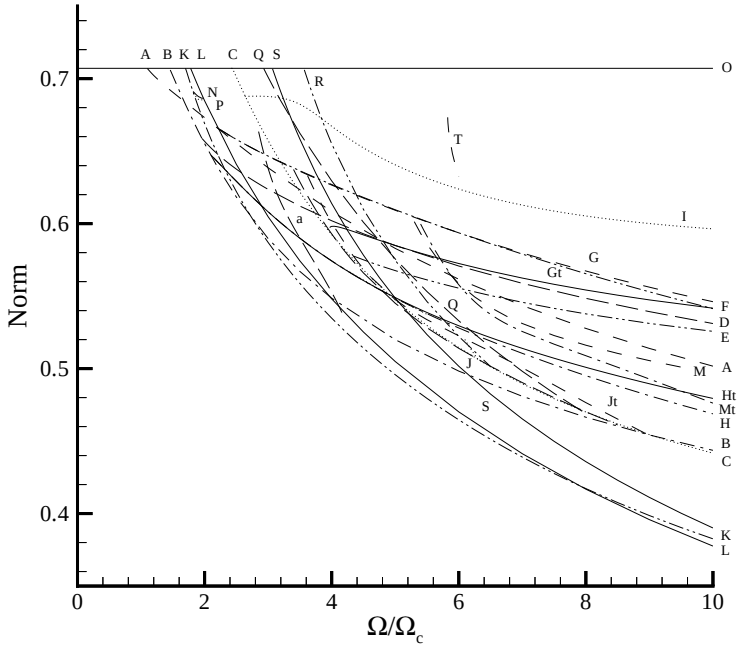

Figure 5.9: Norm of Bifurcating Branches of Solutions vs. Ω/Ω_c for Kolmogorov Flow

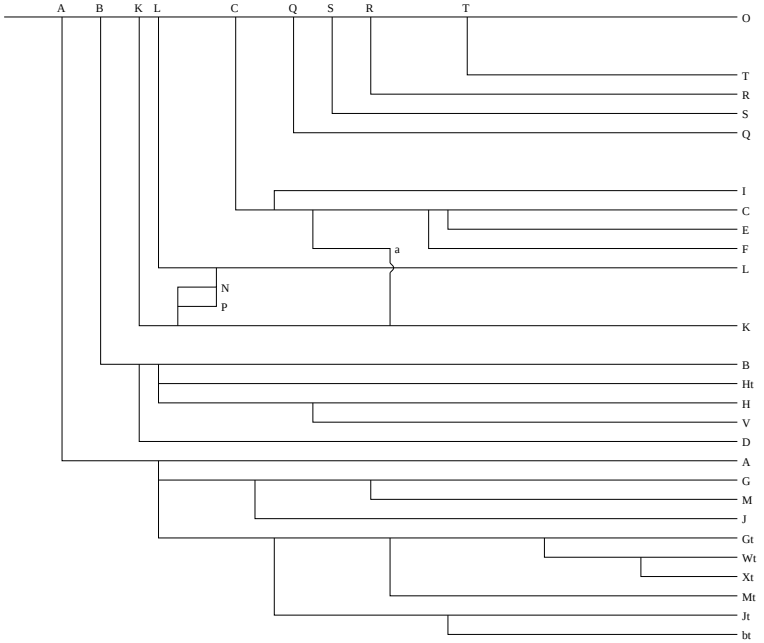

Figure 5.10: Bifurcation Diagram for Kolmogorov Flow

Branch	Bifurcates From Branch	At Ω/Ω_c (to 2 d.p.)	Largest Mode of Null Vector (k_x, k_y, k_z)
A	0	1.10	(1,4,0)
B	0	1.45	(2,4,0)
C	0	2.44	(3,4,0)
D	B	1.96	(1,4,0)
E	C	4.35	(1,4,0)
F	C	3.97	(2,4,0)
G	A	2.25	(1,1,0)
Gt	A	2.25	(1,1,0)
H	B	2.10	(2,1,0)
Ht	B	2.10	(2,1,0)
I	C	2.64	(3,1,0)
J	G	3.40	(1,4,1)
Jt	Gt	3.61	(1,4,1)
K	0	1.70	(1,4,1)
L	0	1.78	(2,4,1)
M	G	5.27	(1,4,2)
Mt	Gt	5.37	(1,4,2)
N	K, L	1.82, 1.98	(2,4,1), (1,4,1)
P	K, L	1.83, 1.98	(2,4,1), (1,4,1)
Q	0	2.93	(3,4,1)
R	0	3.57	(1,4,2)
S	0	3.07	(2,4,2)
T	0		(3,4,2)
V	H	4.14	Periodic
Wt	Gt		Periodic
Xt	Wt		Period Doubling
a	C,K	2.80, 4.17	(3,4,0), (1,4,1)
bt	Jt		Periodic

Table 5.3: Kolmogorov Flow Bifurcation Points

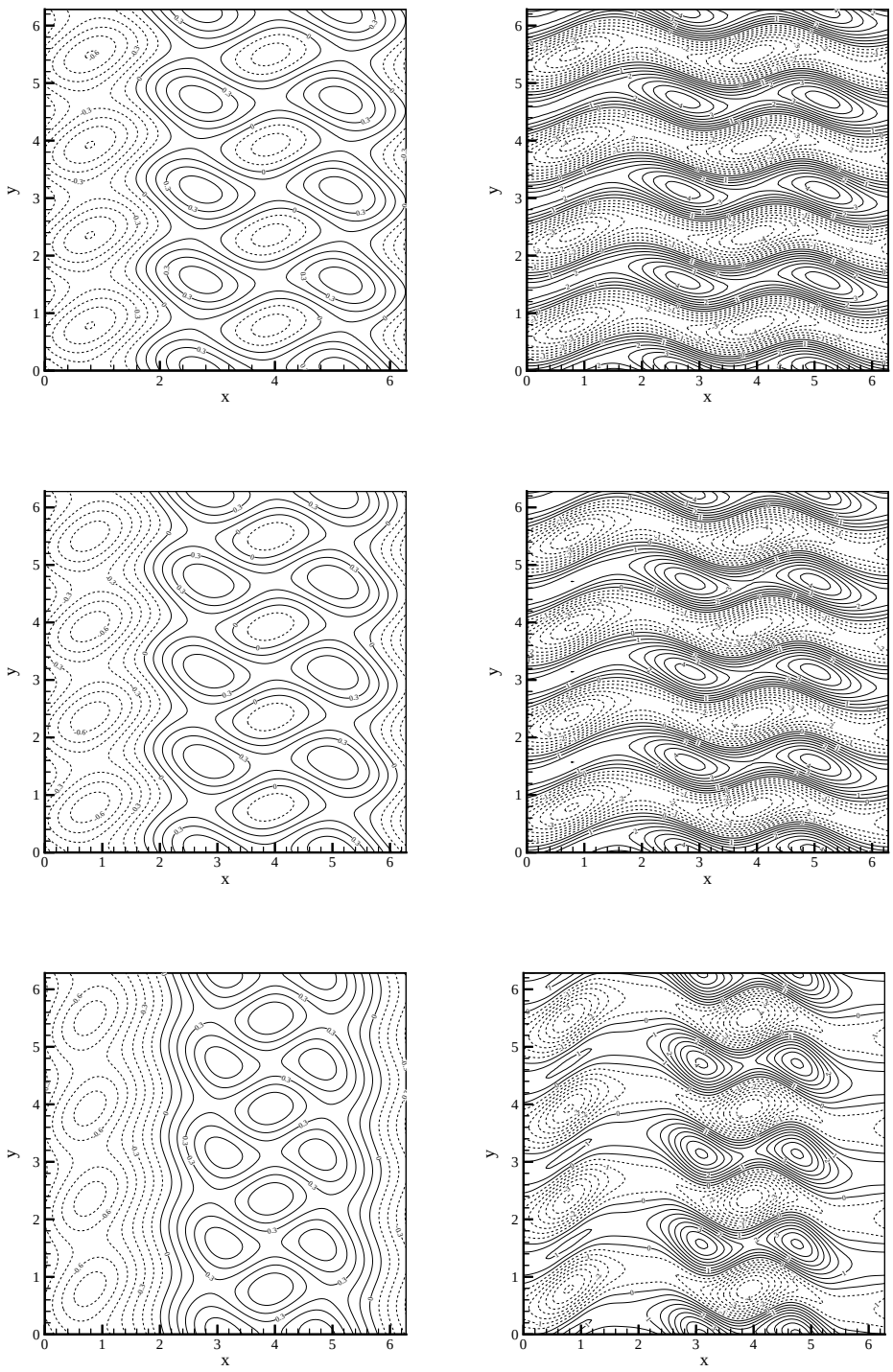

Figure 5.11: Streamfunction (Left) and Vorticity: Branch D at $\Omega/\Omega_c = 2.20, 2.50, 5.00$, From Top to Bottom

5.4 Interconnecting Branches

We have observed some branches that connect between the branches that bifurcate from the shear flow. There is a connection between branch K and branch L, a close up of which is shown in figure 5.12. There are two similar branches that connect between branch K and

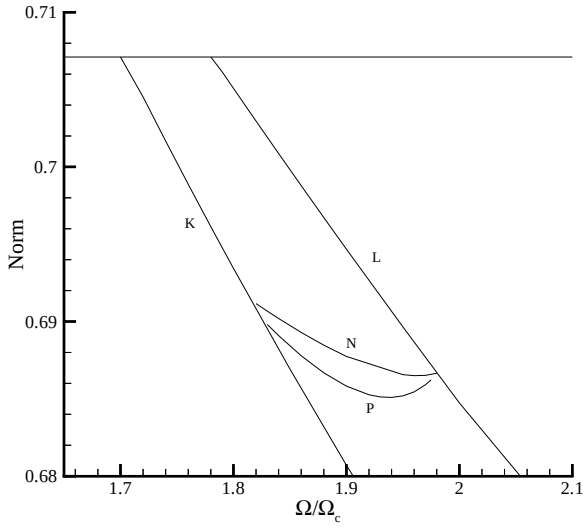

Figure 5.12: Connection Between Branches K and L

branch L; the difference between them is displayed in figure 5.13. Notice that the phase of the top, central and bottom planes has been shifted between the two branches, whereas the other two planes are at the same phase. We have only been able to find these two branches, and there does not appear to be a continuum of branches between these two.

Also a connection between branch C and branch K was found, which is shown in figure 5.15.

We conjecture that there are many other branches that form connections between different primary bifurcating branches.

5.5 Y-Symmetry Breaking Bifurcations

As we continue along both branches A and B, we encounter a point where a real double eigenvalue changes sign. At each of these points we find a bifurcation from which two

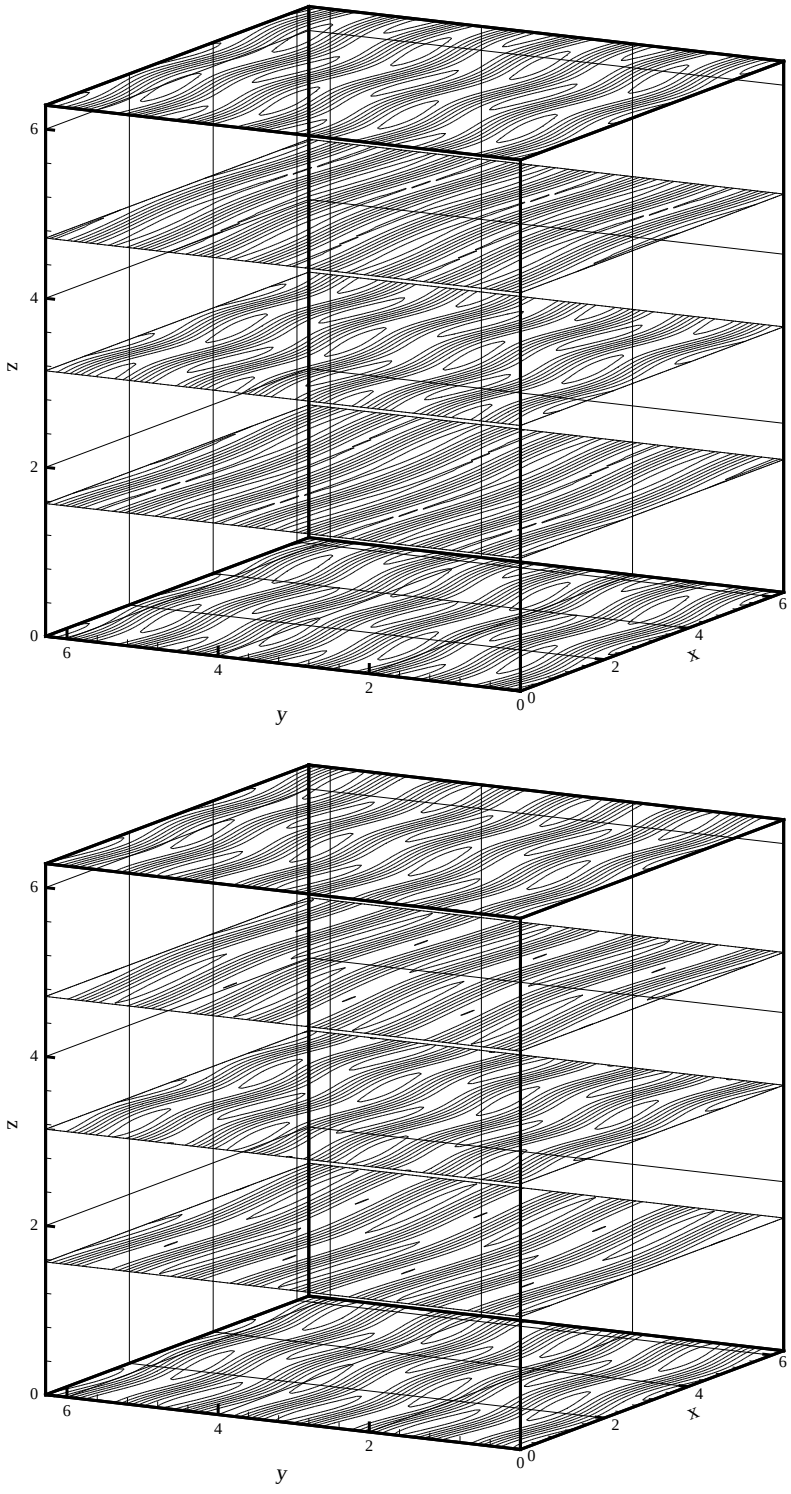

Figure 5.13: Vorticity Contours Showing the Difference Between Branches N (Top) and P at $\Omega/\Omega_c = 1.90$

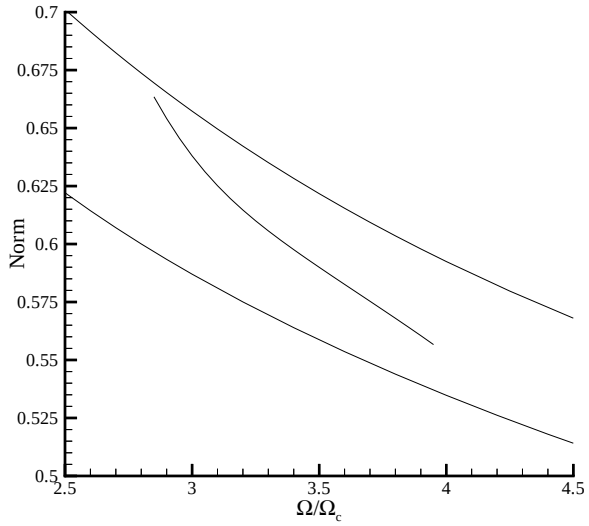

Figure 5.14: Connection Between Branches K and C

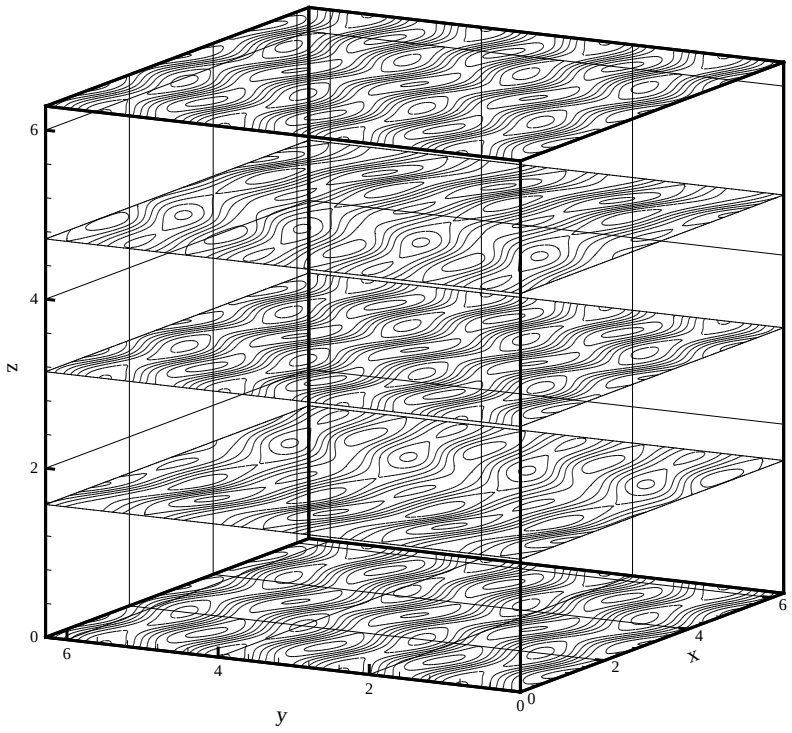

Figure 5.15: Vorticity Contours for Branch a at $\Omega/\Omega_c = 3.50$

branches emerge, a stationary branch and a travelling wave branch. We note that we have a pitchfork bifurcation for each branch. From branch A we obtain branches G and Gt, while from branch B we obtain branches H and Ht. Figures 5.16 and 5.17 show for branches G and Gt, and H and Ht respectively, the difference between the stationary and travelling wave branches.

After the symmetry in the direction of the forcing is broken by a bifurcation, large scale structures develop.

The two null vectors associated with the bifurcation differ by only a translation in the y direction. In order to determine the number of distinct branches bifurcating from this point, we applied the method of perturbed bifurcation numerous times, each time using a different perturbation from this two-dimensional null space. Although this process does not prove that there are only two branches emanating from the bifurcation point, every time we followed this process we obtained either the stationary or travelling wave branch.

Immediately after the bifurcation there is a small difference in the sizes of the vortices. These differences then grow and the cells merge to form large scale structures. Previous studies, such as those by Yakhot and Sivashinsky [36], have suggested that these large scale structures like those in branches G and Gt, figure 5.16 (bottom), form due to a negative-viscosity phenomena. They show that the instability of a flow to long-wavelength disturbances can be interpreted in terms of a negative effective viscosity in the large-scale flow.

Platt et al. first observed a y-symmetry breaking bifurcation on branch B when it loses its stability to branch H. Our parameter value for this bifurcation is at $\Omega/\Omega_c = 2.10$, whereas they observe it at $\Omega/\Omega_c = 2.2$. This discrepancy it probably due to their use of a time-stepping method and not allowing enough time steps for the instability to grow sufficiently.

However, since we were not using a time-stepping algorithm, we did not observe the sudden random horizontal shifts of the solution that Platt observed in the range $3.53 \leq \Omega/\Omega_c \leq 3.6$.

When Platt et al. started from the perturbed shear flow, they first found large-scale structure of branch Gt at $\Omega/\Omega_c = 4.72$. Altough in an attempt to find a hytersis loop back to some choatic flows they observed below this Reynolds number, they discovered that the large scale branch Gt solutions connect to the small scale branch A solutions

at $\Omega/\Omega_c = 2.2$. This is in good agreement with where we found the branch G and Gt bifurcation at $\Omega/\Omega_c = 2.25$.

5.6 Travelling Wave Solutions

Travelling wave solutions have been observed by She [31], and Platt et al [29]. However, they have not explained how these flows originate. As shown in figures 5.16 and 5.17, these solutions are similar to steady state solutions, except that they have an asymmetry in the y-direction in the size of the vortices. A careful look shows that branches G and H are symmetric about $y = \pi$, while branches Gt and Ht are not.

We find that speed of the branch Gt travelling wave, when it bifurcates from branch A, is equal to zero. As we continue along this branch, we plot how the speed of the travelling wave changes with Reynolds number, figure 5.18. Interestingly we find that the direction of the travelling wave changes at two locations along the Gt branch, whereas for branch Ht we only observe motion in one direction.

Platt et al. noted that there was a slow drift in their large-scale structure solutions; however, they did not identify them to be travelling wave solutions. The first stationary travelling wave solution at $\Omega/\Omega_c \approx 5.924$ was also observed by Platt et al. [29]. They refer to it as a spatially chaotic but temporally stable solution. Figure 5.19 shows how the energy of this solution varies with the wavenumber.

We note that wave speed of branch Gt is not asymptoting to the value shown in figure 5.18 but starts decreasing again. However, the wave speed of both branches Gt and Ht might asymptote to some value as the Reynolds number tends to infinity.

The difference in the wave speed between using 64 modes instead of 32 is of the order of 1%. This causes the Reynolds Number at which the wave speed first changes sign to be slightly reduced from $\Omega/\Omega_c \approx 5.924$ to $\Omega/\Omega_c \approx 5.918$.

5.7 Secondary Bifurcations to Three-Dimensional Flows

As noted in section 5.1, there are three-dimensional solutions that bifurcate directly from the shear flow solution. As we continue along branch G or Gt, we find other bifurcations to three-dimensional flows, with either one or two waves in the z direction.

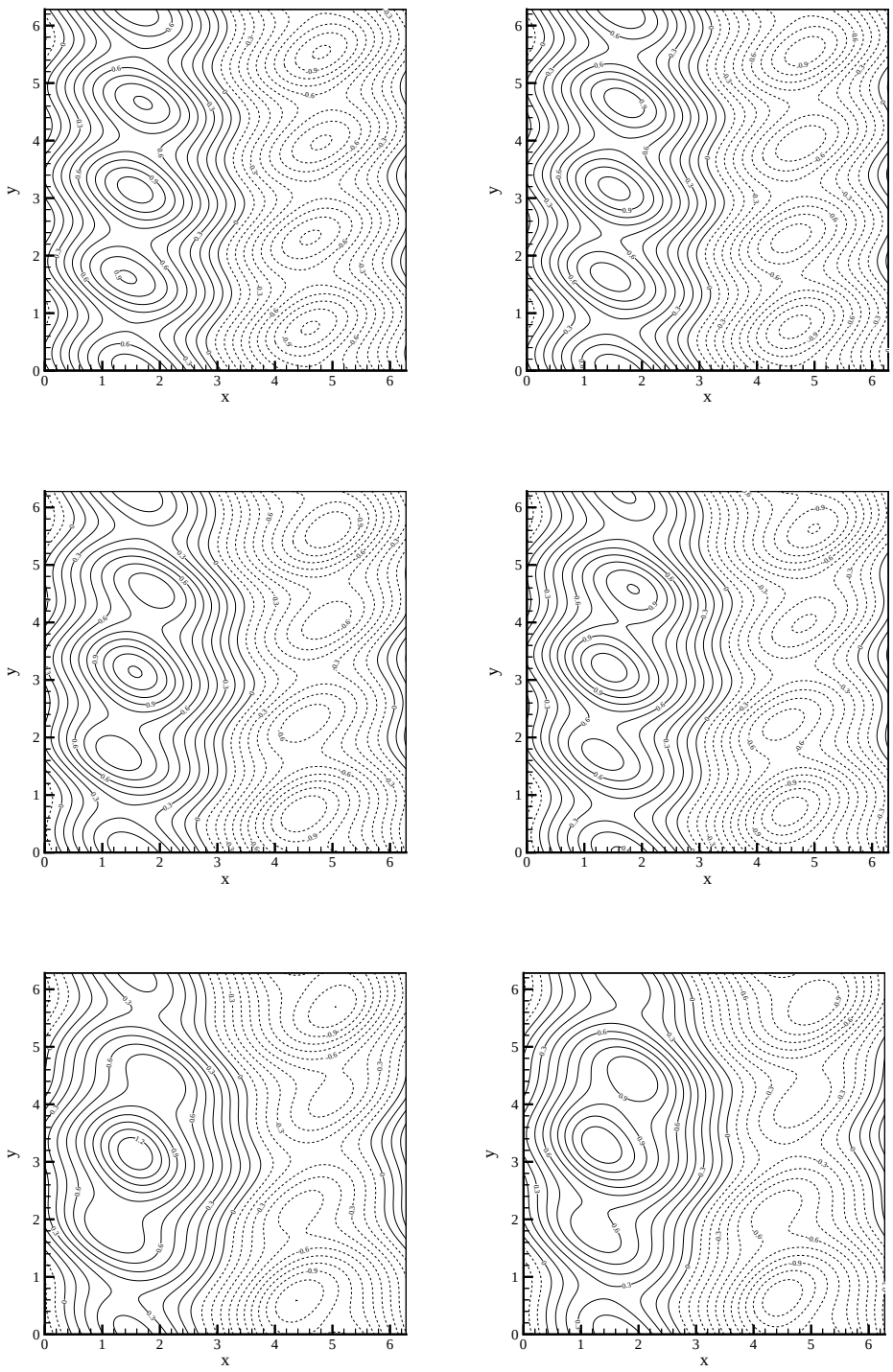

Figure 5.16: Streamfunction: Branches G (Left) and Gt at $\Omega/\Omega_c = 2.30, 3.00, 5.00,$ From Top to Bottom

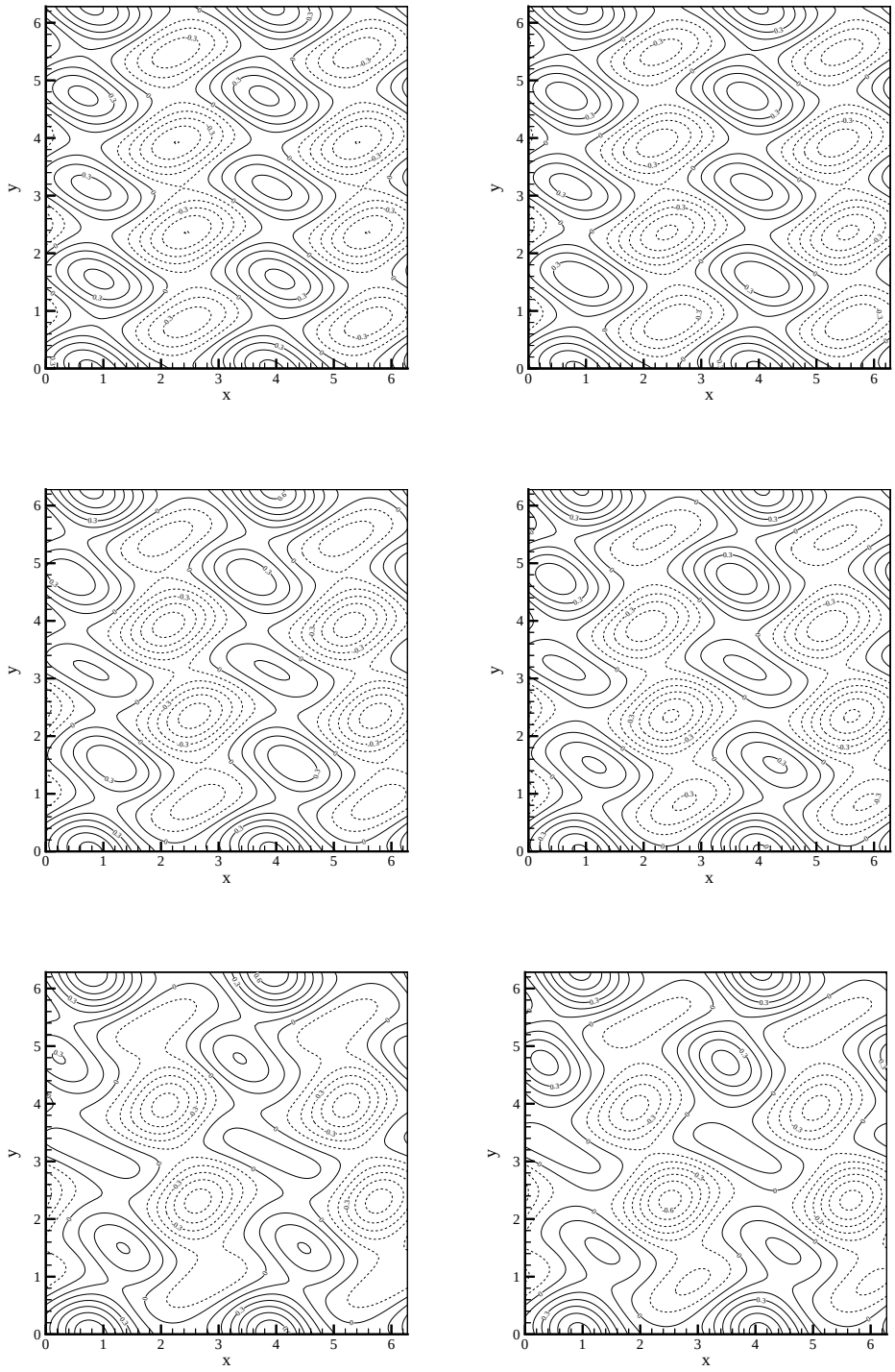

Figure 5.17: Streamfunction: Branches H (Left) and Ht at $\Omega/\Omega_c = 2.20, 3.00, 5.00,$ From Top to Bottom

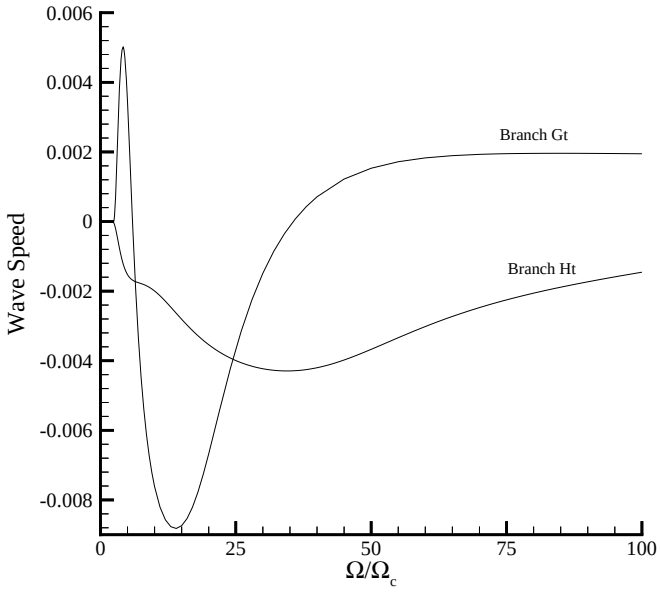

Figure 5.18: Wave Speed vs. Ω/Ω_c

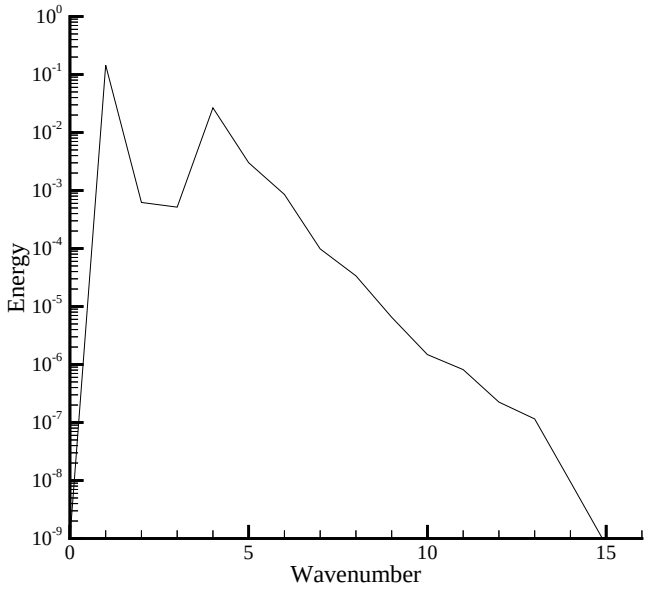

Figure 5.19: Energy vs. Wavenumber, Branch Gt, $\Omega/\Omega_c = 5.924$

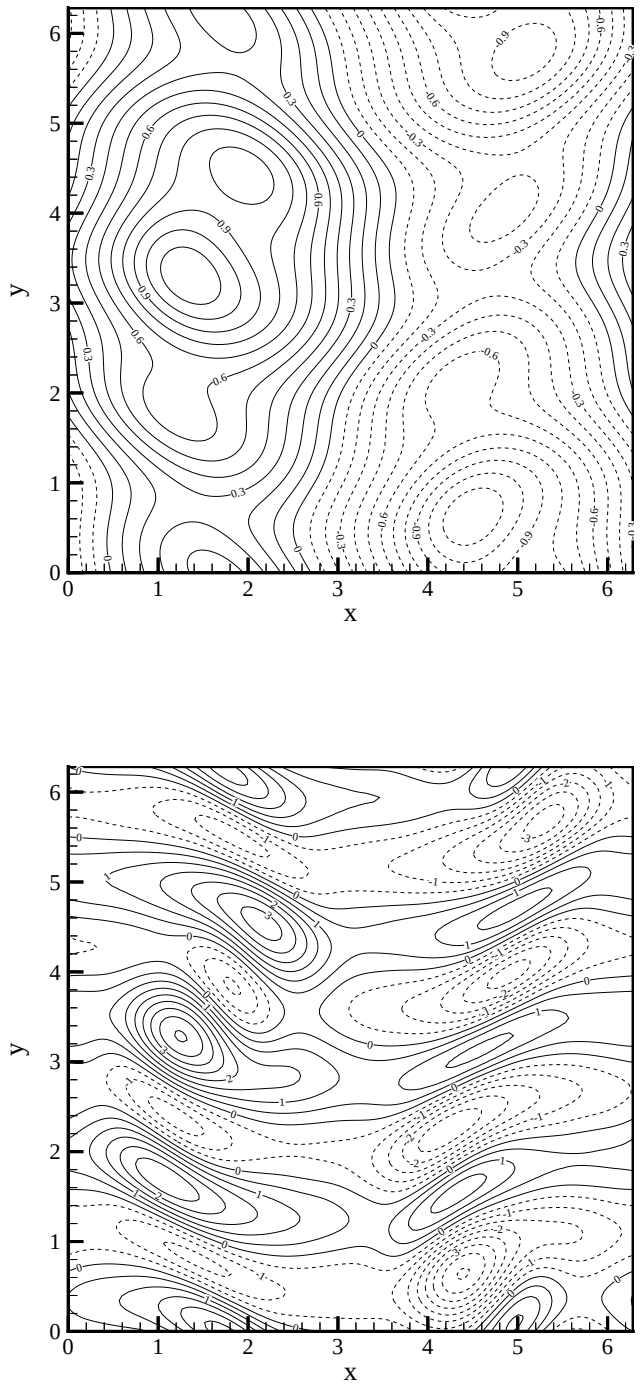

Figure 5.20: Streamfunction (Top) and Vorticity: Branch Gt, $\Omega/\Omega_c = 5.924$

Figure 5.21 shows the slight difference between the two three-dimensional flows, labeled J and Jt, with one wave in the z direction that originate from branches G and Gt respectively. The difference in the vortex sizes of these two solutions originates in the difference in the branches from which they bifurcate, as shown in figure 5.16.

Also we found similar solution branches M and Mt that have two waves in the z direction. A solution from branch M is shown in figure 5.22. Additionally we find that the three-dimensional branches Jt and Mt that bifurcate from the two-dimensional travelling wave branch Gt are also travelling wave solutions. Figure 5.23 shows the wave speed of these three-dimensional travelling wave branches, along with the average wave speed of a periodic branch Wt which is described in the next section.

It is seen in figures 5.21 and 5.22 that these solutions contain vortex tube structures. We conjecture that these tubes are the beginning of the worms that are present at higher Reynolds numbers in turbulent flow. During this transition the solution goes though many bifurcations which shear and stretch the vortex tubes into worms.

Strangely on branches H and Ht, which differ from branch G and Gt only by the number of waves in the x direction, we did not find any bifurcations to steady three-dimensional flows. We believe that this phenomenon is similar to the behaviour along the shear flow branch where there are only a finite number of bifurcation points, and at the higher aspect ratios the number of bifurcation points decreases. It would be interesting to follow the three-dimensional bifurcation points on branch G as the aspect ratio is changed.

5.8 Periodic Solutions

As the Reynolds number is increased further, we encounter Hopf Bifurcations which yield time periodic solutions. These branches are continued by finding the fixed point of a Poincare map as described in section 3.6.3. To compute this Poincare map we use the second order time-stepping method described in section 3.4. Thus only second order accurate solutions result. However, increased accuracy is achieved by using Richardson extrapolation, as shown in table 5.4.

We have followed two two-dimensional periodic solutions, V and Wt, that arise from Hopf bifurcations on branches H and Gt respectively. They are shown in figures 5.25 and 5.26. Figure 5.24 shows how the period of the solution varies along these branches. We have

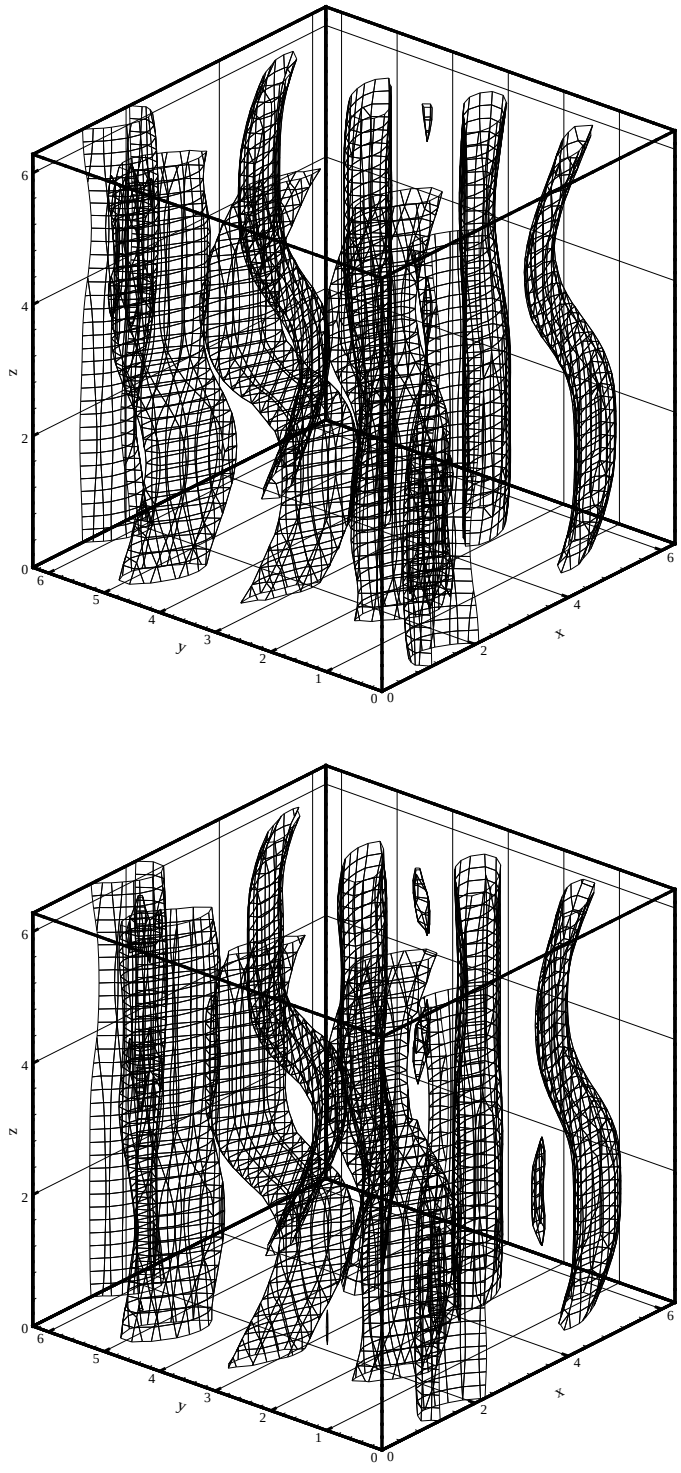

Figure 5.21: Vorticity Isosurface: Branches J (Top) and Jt at $\Omega/\Omega_c = 5.00$

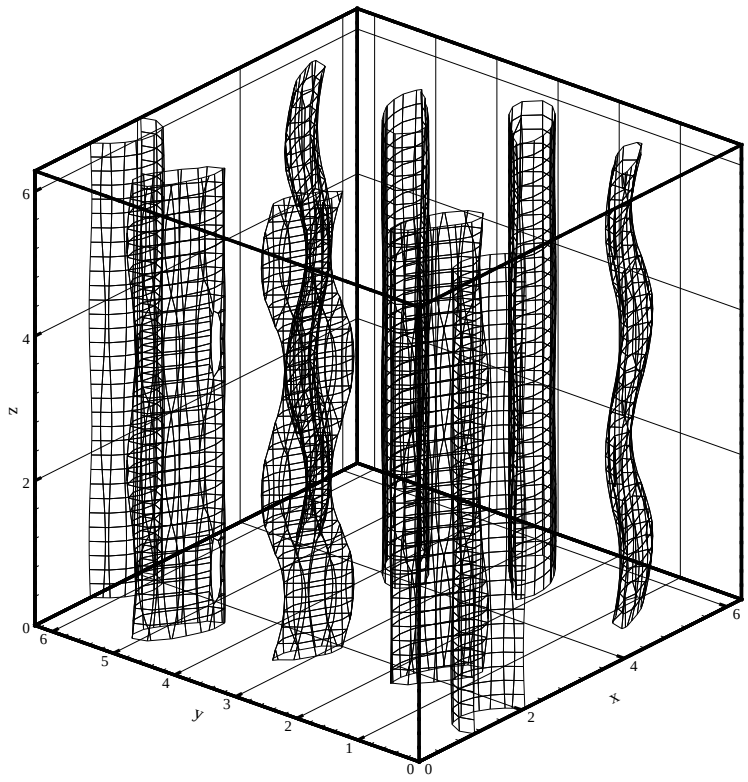

Figure 5.22: Vorticity Isosurface: Branch M at $\Omega/\Omega_c = 5.50$

Δt	Norm	Period	Error	Extrapolated
1/10	0.555066395533	13.3497703977	2.96×10^{-2}	
1/20	0.555046581214	13.3276095830	7.42×10^{-3}	13.3202226448
1/40	0.555041916099	13.3221653154	1.98×10^{-3}	13.3203505595
1/80	0.555040267633	13.3206589615	4.71×10^{-4}	13.3201568435
1/160	0.555039944093	13.3203081731	1.21×10^{-4}	13.3201912436
1/320	0.555039853934	13.3202176506	3.02×10^{-5}	13.3201874764

Table 5.4: Convergence of Period With Time-step on Branch V at $\Omega/\Omega_c = 4.50$

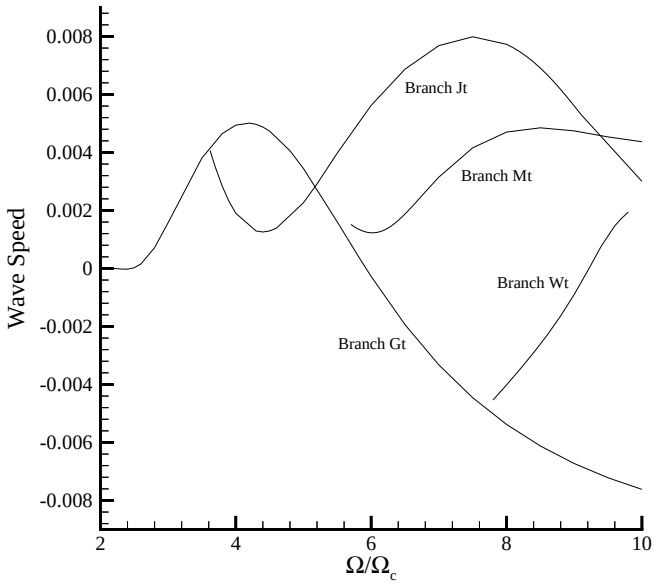

Figure 5.23: Wave Speed vs. Ω/Ω_c

not followed any other periodic branches resulting from any of the other Hopf bifurcation points because we are unable to switch to them as they are unstable.

Branch Wt is a periodic travelling wave solution. During one orbit the solution shifts horizontally, and this wave speed is shown in figure 5.23. Furthermore, we find that branch Wt undergoes a period doubling bifurcation at $\Omega/\Omega_c \approx 6.1$, the result of which is shown in figure 5.27. The small effect of the period doubling bifurcation can be observed by comparing the vortex sizes of the $t = 0.0$ and $t = 37.5$ pictures which are taken at the same phase in the orbit.

Additionally, there are three-dimensional time periodic branches. We follow the branch bt that bifurcates from branch Jt, figure 5.21. Figure 5.28 shows the two extremities of the movement of the vortex tubes for this periodic solution.

We find that the velocity of the travelling wave for periodic solutions on branch bt, unlike all other travelling wave solutions, is no longer in the x direction but has a small component in the z direction as well. Unfortunately, we are unable to follow this branch far, since it becomes unstable quickly and RPM has trouble in maintaining convergence.

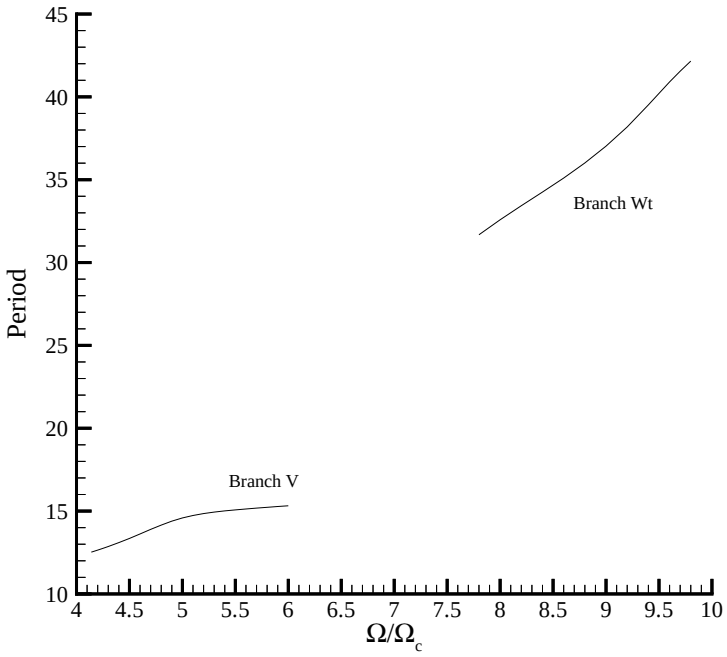

Figure 5.24: Period vs. Reynolds Number

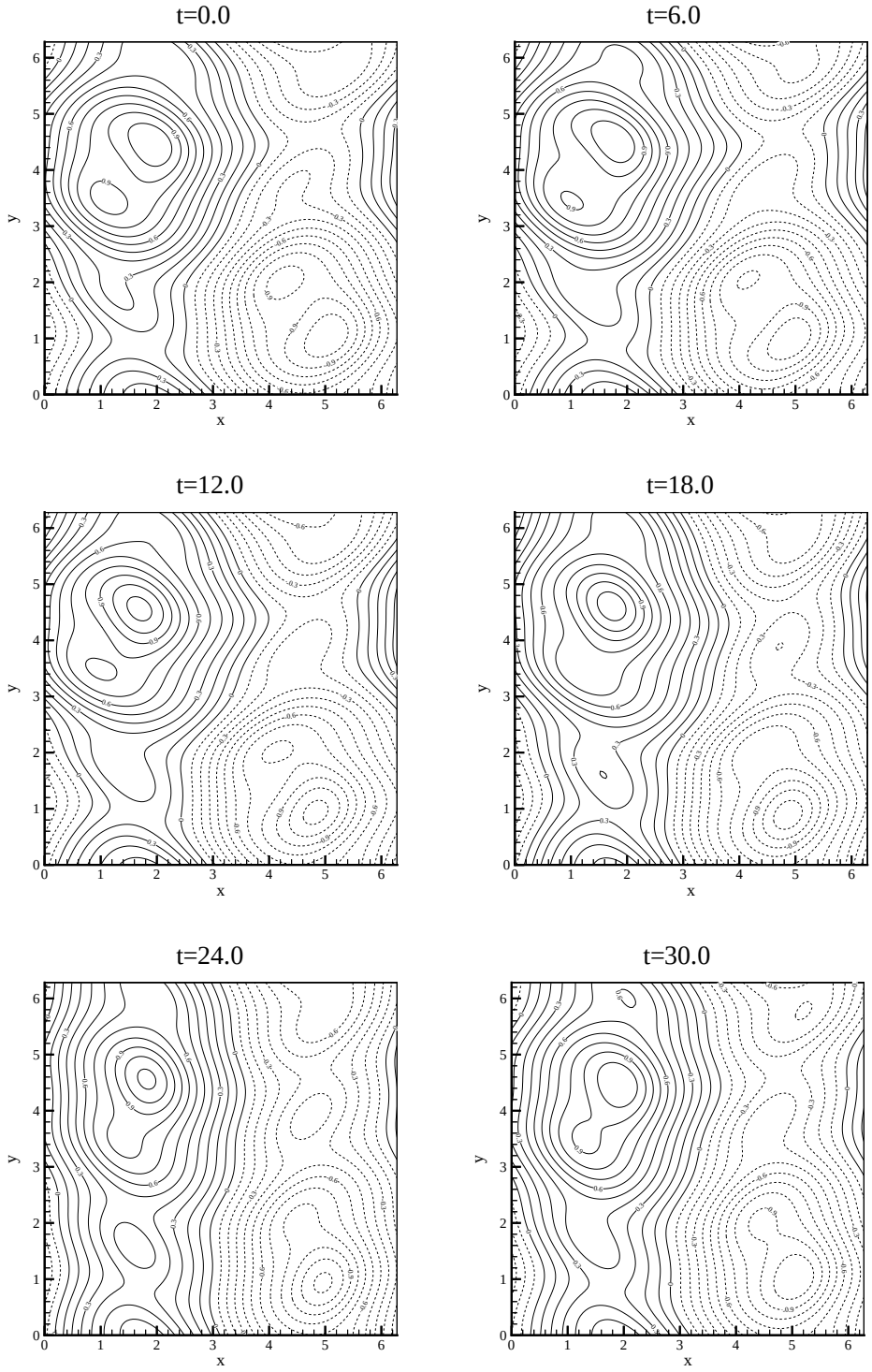

Figure 5.25: Streamfunction: Branch Wt at $\Omega/\Omega_c = 8.80, t = 0.0, 6.0, 12.0, 18.0, 24.0, 30.0$. Period=36.0113, dt=0.1

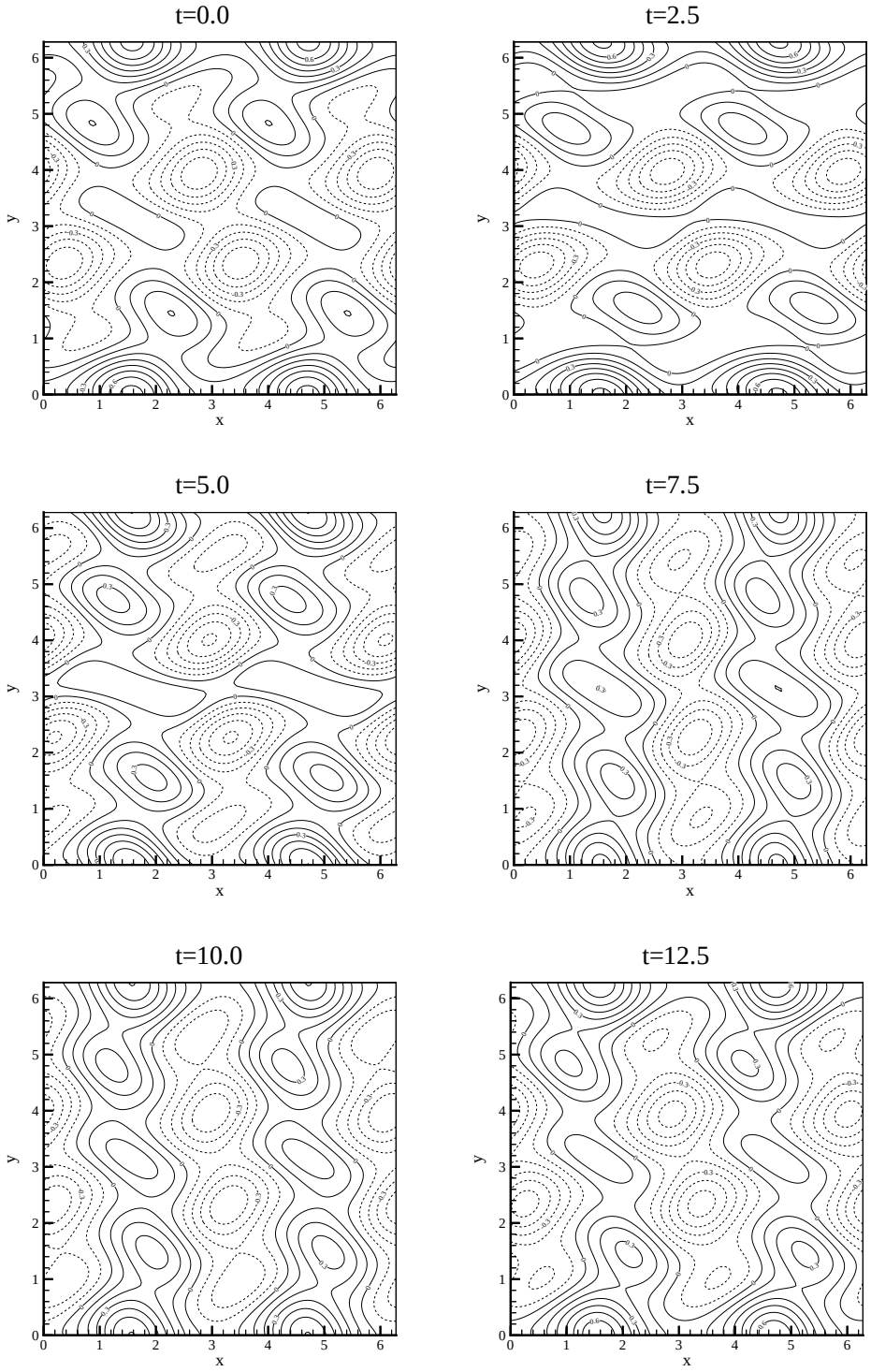

Figure 5.26: Streamfunction: Branch V at $\Omega/\Omega_c = 5.00, t = 0.0, 2.5, 5.0, 7.5, 10.0, 12.5$. Period=14.5857, dt=0.1

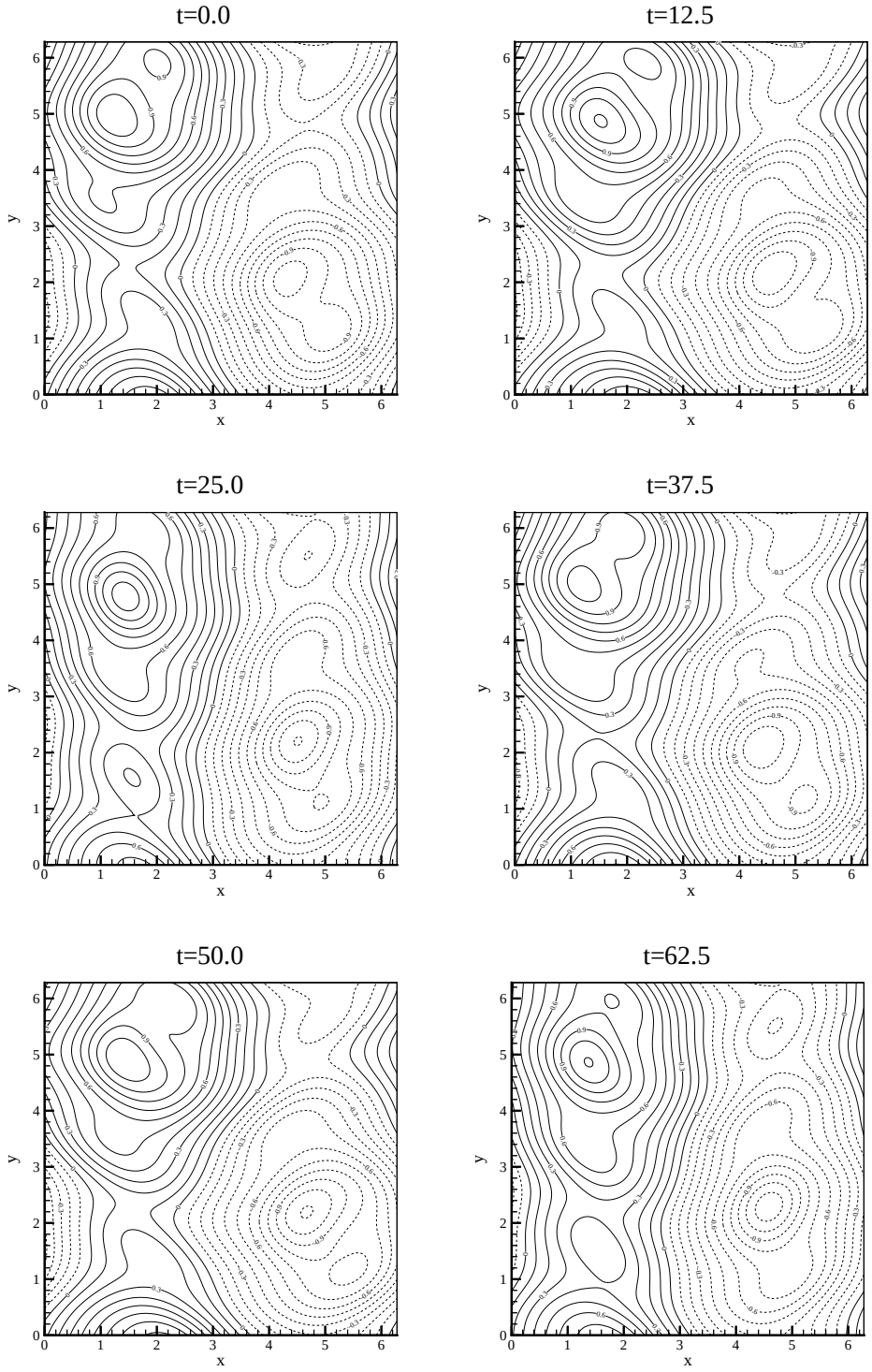

Figure 5.27: Streamfunction: Branch Xt at $\Omega/\Omega_c = 9.30, t = 0.0, 12.5, 25.0, 37.5, 50.0, 62.5$. Period=75.1436, dt=0.1

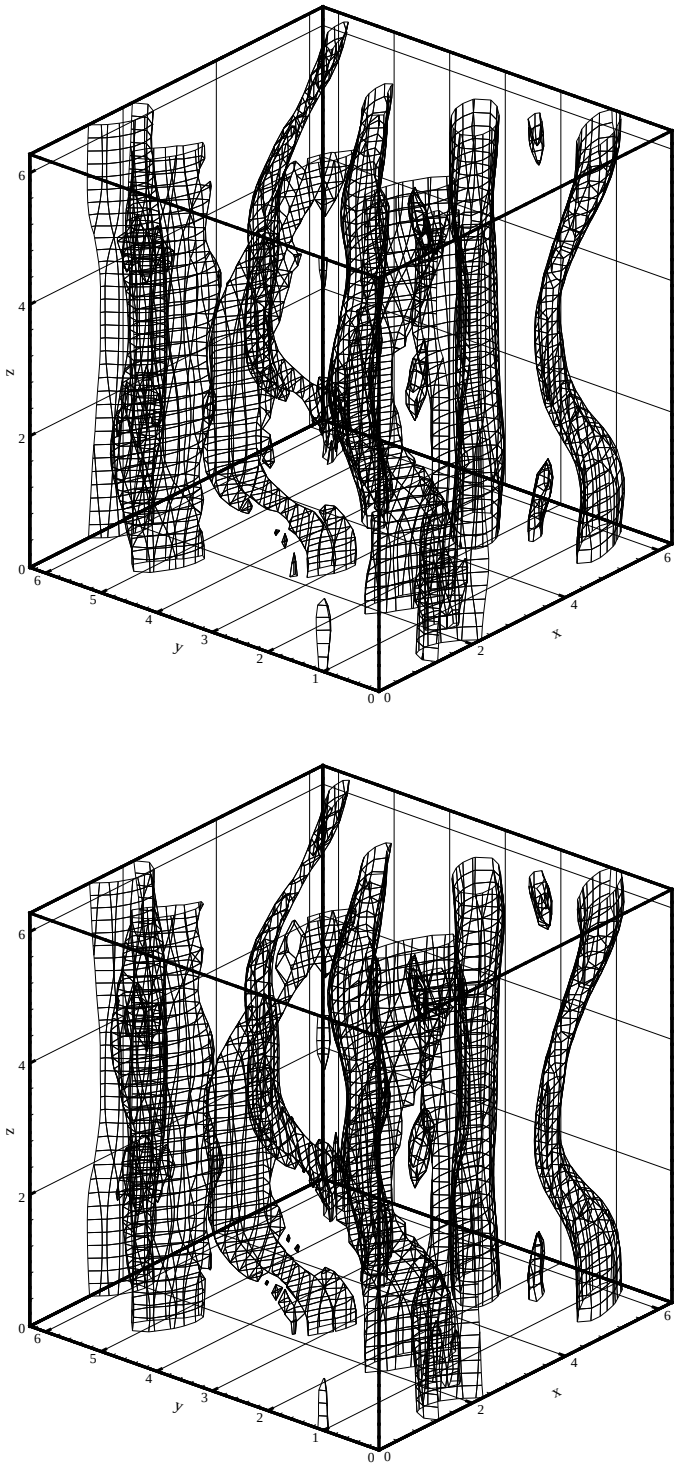

Figure 5.28: Branch bt, $\Omega/\Omega_c = 6.20$, $t = 6.0(\text{top}), 15.0$

5.9 Chaotic Flow

Although we are unable to follow chaotic flow, we know that it occurs due to many Hopf bifurcations. The instantaneous flow shown figure 5.29 was obtained by integrating the partial differential equation in time; we did not follow the many Hopf bifucations to reach this flow. This figure shows how the vortex tubes have been altered by those many Hopf bifurcations. Kolmogorov flow at high Reynolds numbers has been studied by Borue and Orszag [7]. They demonstrate that the flow is isotropic on small scales.

This flow is used in the next chapter to compare the statistics obtained from the other branches we have followed.

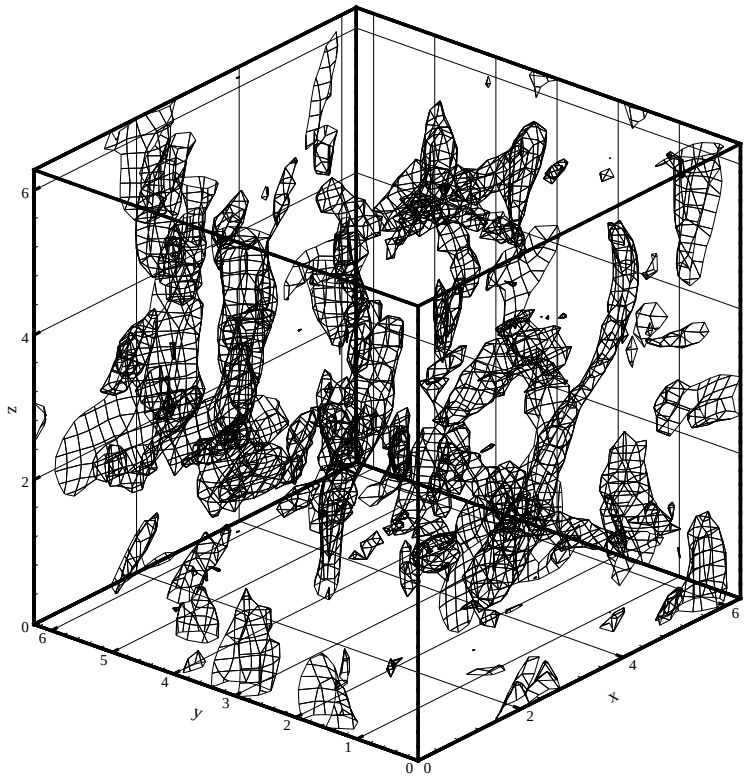

Figure 5.29: Vorticity Isosurface: Chaotic Flow at $\Omega/\Omega_c = 20.0$

We did not observe the regions of meta-stable chaotic flow that were found by Platt et al. at relatively low Reynolds numbers in the range $4.47 \leq \Omega/\Omega_c \leq 4.71$. Their chaotic flow appears to originate from branch V; however, since we found branch V to be stable until

$\Omega/\Omega_c \approx 5.0$, we believe that they were observing transient flow.

Chapter 6 Comparison of Kolmogorov Flow with Turbulence Calculations

Turbulence is said to occur when the kinematic viscosity of a fluid is sufficiently small so that there are observed apparently random small scale fluctuations in the velocity field. We compare the statistics of our steady state flows with those from turbulence calculations. The macroscopic difference between these two types of flows is that the steady state branches we have found are very structured.

A major difference to note while comparing these flows is that turbulence calculations are typically done with an isotropic forcing, whereas Kolmogorov flow has an anisotropic forcing.

The statistics referred to in this chapter as "Chaotic Flow" are the statistics from the instantaneous flow shown in figure 5.29. The "Chaotic Flow" does not give good statistics of turbulent flow; however, it serves as a useful comparison between our flows and turbulent ones. To obtain good statistics of turbulent flows, the averages need to be computed over many eddy turnover times.

6.1 Taylor Reynolds Number

There are two methods for computing the Taylor Reynolds number: by using the longitudinal velocity correlation function or the energy spectrum function. In this section we consider the use of the longitudinal velocity correlation function. The energy spectrum function is considered in the following section.

The statistics of the flow are defined using average values of the appropriate quantities. We define $\bar{u}$ to be the spatial average velocity of the flow:

$$\overline{u} \equiv \frac{1}{|V|} \int_V u dV. \tag{6.1}$$

With this averaging our flow is homogeneous, although it is not isotropic since our forcing is only in one direction.

We calculate this average numerically using the trapezoidal rule:

$$\overline{u} \equiv \frac{1}{N_x N_y N_z} \sum_{m_x, m_y, m_z} u_{m_x m_y m_z}. \tag{6.2}$$

We note that using the trapezoidal rule on periodic functions with equally spaced grid points yields spectrally accurate results.

We use this definition of the average to compute the various statistics of our flows. The root mean squared velocity u' is defined as

$$u' \equiv \sqrt{\overline{u^2}} = \sqrt{\frac{1}{|V|} \int_V u^2 dV}; \tag{6.3}$$

and the longitudinal velocity correlation function in the x-direction is

$$f(r) \equiv \frac{\overline{u(x)u(x+r)}}{\overline{u^2}}. \tag{6.4}$$

Due to our anisotropic forcing, we are also able to define longitudinal velocity correlation functions in the y and z-directions. In the infinite domain the correlation tends to zero as the separation tends to infinity; however, in our case this does not occur due to the periodicity of our domain. To get accurate results in the periodic case, it is desirable that the correlation is small when the separation is not close to being a multiple of the period.

The Taylor Reynolds number is defined as

$$R_\lambda = \frac{u'\lambda}{\nu}, \tag{6.5}$$

where the Taylor Microscale λ is defined by

$$\lambda = \sqrt{-\frac{1}{\frac{d^2 f}{dx^2}(0)}}. \tag{6.6}$$

In our system the kinematic viscosity ν is equal to $1/\Omega$, and therefore we calculate the Taylor Reynolds number as

$$R_\lambda = u'\lambda\Omega. \tag{6.7}$$

Recall that due to the anisotropy of our flow we define three different Taylor Reynolds numbers, one in each of the coordinate directions.

In infinite domains it is also possible to define an integral scale:

$$L \equiv \int_0^\infty f(r)dr. \tag{6.8}$$

This measures the linear extent of the region within which velocities are appreciably correlated. However, this definition does translate into the case of periodic domains. In the next section we use the Energy Spectrum function to define an integral scale.

The velocity correlation for the two-dimensional branch Gt at $\Omega/\Omega_c = 20.0$ is shown in figure 6.1. The correlation can be compared with the figure 6.2, which shows the streamfunction of that solution. We note that the longitudinal velocity correlation function in the y-direction stays close to unity. The Taylor Reynolds numbers computed for all the flows are listed in table 6.1.

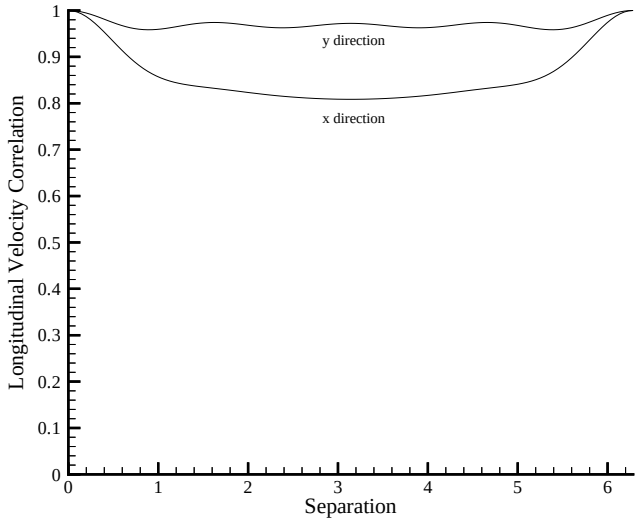

Figure 6.1: Longitudinal Velocity Correlation: Branch Gt, $\Omega/\Omega_c = 20.0$

The velocity correlation for the two-dimensional branch Ht at $\Omega/\Omega_c = 100.0$ is shown in figure 6.3. The streamfunction of this solution is shown in figure 6.4. This flow has a substantially lower velocity correlation compared to branch Gt.

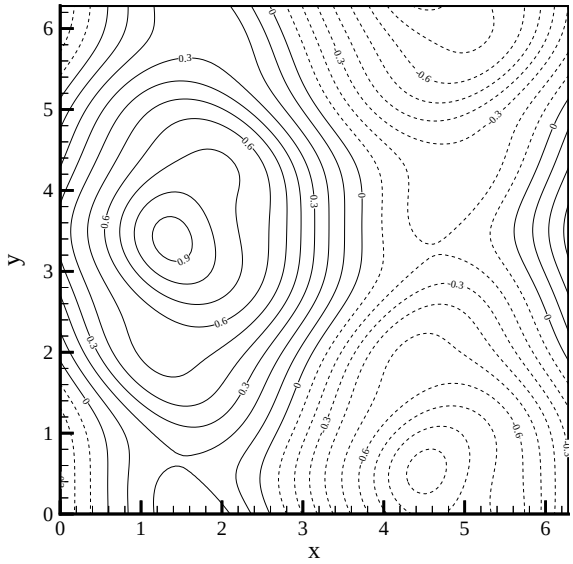

Figure 6.2: Streamfunction: Branch Gt, $\Omega/\Omega_c = 20.0$

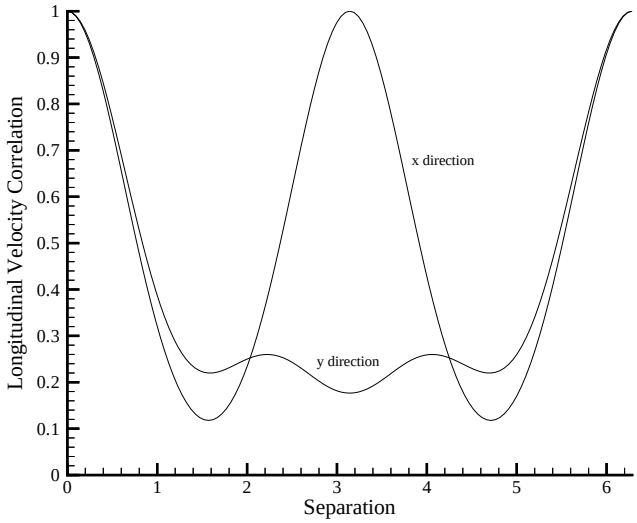

Figure 6.3: Longitudinal Velocity Correlation: Branch Ht, $\Omega/\Omega_c = 100.0$

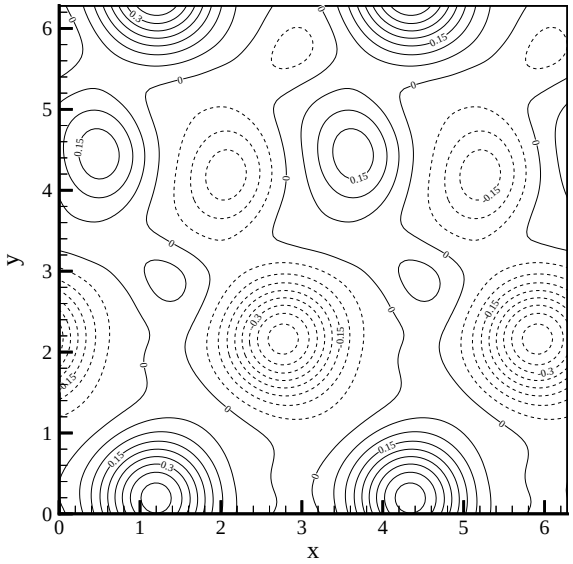

Figure 6.4: Streamfunction: Branch Ht, $\Omega/\Omega_c = 100.0$

In figure 6.5 we show the correlation on the three-dimensional branch Mt, see figure 6.6, at $\Omega/\Omega_c = 10.0$. We note that compared to branch Gt, which branch Mt bifurcates from, the correlation for this branch is significantly lower. Furthermore, the Chaotic flow has an even smaller correlation, as can be seen in figure 6.7.

In table 6.1 we list the Taylor Reynolds numbers for these various flows. Although there are concerns about the accuracy of this method, given that we retain a large degree of correlation, these numbers are in good agreement with those obtained from the Energy Spectrum function; see table 6.2.

	Branch Gt	Branch Ht	Branch Mt	Chaotic
Ω/Ω_c	20.0	100.0	10.0	20.0
R_λ x direction	33.602	70.897	18.427	21.030
R_λ y direction	80.260	79.231	17.736	13.514
R_λ z direction	-	-	1.198	7.622

Table 6.1: Taylor Reynolds numbers computed from the Longitudinal Velocity Correlation Function

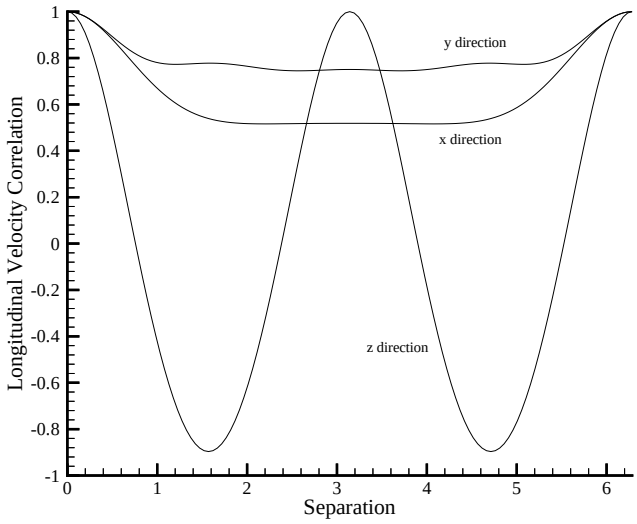

Figure 6.5: Longitudinal Velocity Correlation: Branch Mt, $\Omega/\Omega_c = 10.0$

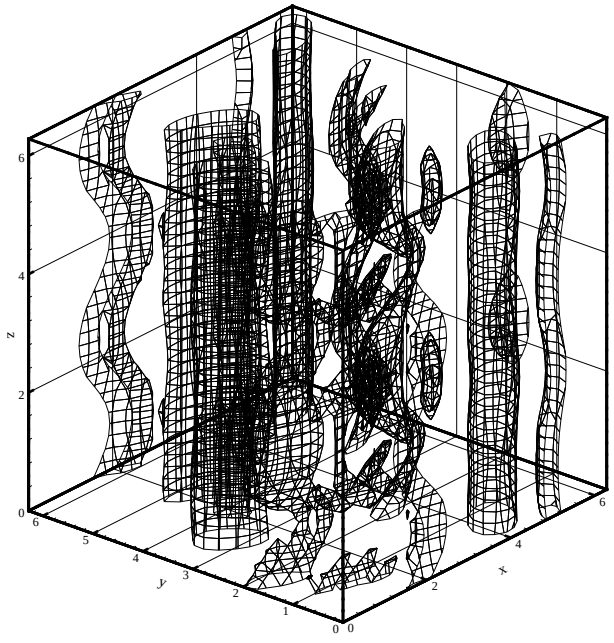

Figure 6.6: Vorticity: Branch Mt, $\Omega/\Omega_c = 10.0$

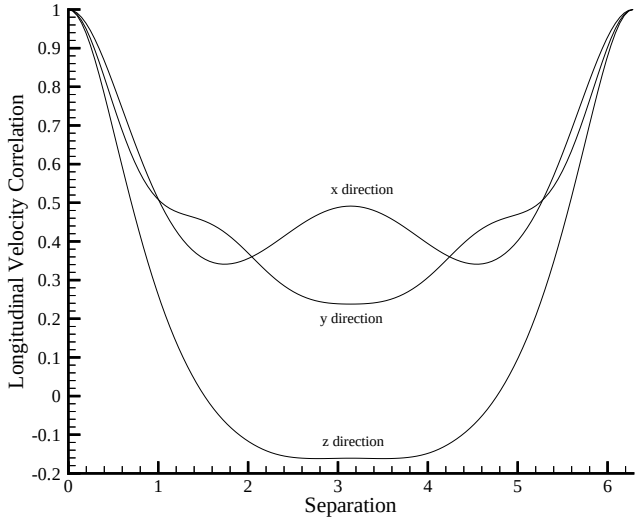

Figure 6.7: Longitudinal Velocity Correlation for Chaotic Flow

6.2 Energy Spectrum

The Energy Spectrum function is also to determine the Taylor Reynolds number of the flow. On an infinite domain the Energy Spectrum function $E(k)$ is a continuous function. However, we follow the standard approach for periodic domains and group the wavenumbers to get

$$E(k) \equiv \frac{1}{2} \sum_{k-1/2<|\hat{k}|<k+1/2} |u_{\hat{k}}|^2. \tag{6.9}$$

Since our Taylor Reynolds number is too low, we are unable to observe the Kolmogorov scale that describes the scaling of the Energy Spectrum function in the inertial range.

Using the Energy Spectrum function we are able to compute various quantities of the flow. The derivations of these equations can be found in Batchelor [5]. The root mean squared velocity is equal to

$$u' = \sqrt{\frac{2}{3} \int_0^\infty E(k) dk}. \tag{6.10}$$

Note that due to the grouping of the wavenumbers, we obtain a different value for the root

mean squared velocity when computing it from the Energy Spectrum function rather than directly from the solution, in 6.3.

We can use the Energy Spectrum function to define two different length scales, the integral scale L:

$$L \equiv \frac{3\pi}{4} \frac{\int_0^\infty k^{-1} E(k) dk}{\int_0^\infty E(k) dk}, \tag{6.11}$$

and the Taylor microscale λ:

$$\lambda \equiv \sqrt{5 \frac{\int_0^\infty E(k) dk}{\int_0^\infty k^2 E(k) dk}}. \tag{6.12}$$

Now in the same manner as before, we define the Taylor Reynolds number by

$$R_\lambda = u' \lambda \Omega, \tag{6.13}$$

where the kinematic viscosity is equal to $1/\Omega$.

Also we can define a Reynolds number based on the integral scale:

$$R_L = u' L \Omega. \tag{6.14}$$

The energy spectrum function for branches Ht at $\Omega/\Omega_c = 100.00$, Mt at $\Omega/\Omega_c = 10.00$ and Chaotic flow are shown in figure 6.8. In table 6.2 we show the Reynolds numbers obtained from those Energy Spectrum functions. Interestingly, we find that the Taylor Reynolds number of the Chaotic flow is smaller than that of branch Mt. This is due to the smaller structures in the Chaotic flow.

	Branch Gt	Branch Ht	Branch Mt	Chaotic
Ω/Ω_c	20.0	100.0	10.0	20.0
u'	0.2629	0.1635	0.2702	0.1701
λ	1.4469	0.7401	0.9041	0.5840
L	2.2252	0.9821	1.7626	0.8356
R_λ	43.036	68.454	13.821	11.236
R_L	66.186	90.843	26.945	16.077

Table 6.2: Reynolds Numbers Computed From the Energy Spectrum Function

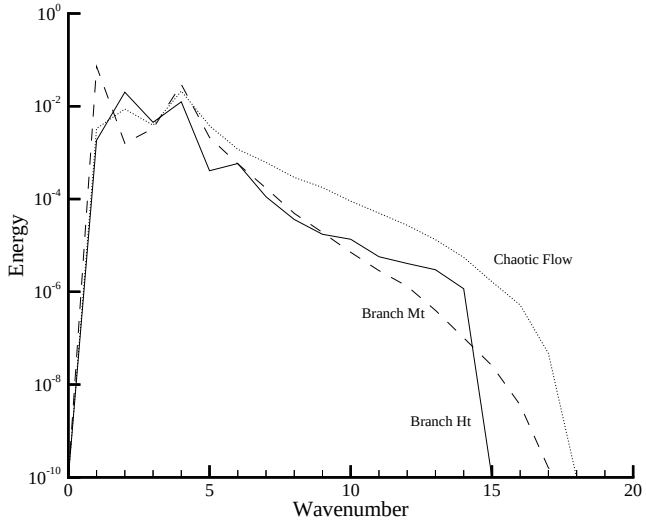

Figure 6.8: Energy Spectrum: Branch Ht, $\Omega/\Omega_c = 100.0$, Branch Mt $\Omega/\Omega_c = 10.0$ and Chaotic Flow

6.3 Distributions of Various Quantities

We now look in detail at the distributions of various quantities in the flows. Due to the number of unstable eigenvectors on the three-dimensional branches, we were unable to follow them to as high a Taylor Reynolds number as would be desired.

First we consider the distribution of the longitudinal velocity gradients. We define the nth-order skewness or, when n is even, flatness in the x-direction F_n^x to be

$$F_n^x \equiv \frac{\overline{\left(\frac{du}{dx}\right)^n}}{\overline{\left(\frac{du}{dx}\right)^2}^{(n/2)}}. \tag{6.15}$$

The skewnesses and flatnesses in the y and z directions are defined similarly.

In three-dimensional isotropic turbulent flow the skewnesses are negative, while the flatnesses are positive. In two-dimensional flow the continuity equation implies that the two skewness in the x and y directions are of equal magnitude but opposite sign. We see in the following tables that the three-dimensional flow also has some positive skewness values; however, they change sign as the flows become more chaotic.

In figures 6.9 - 6.11 we plot flow statistics for the two-dimensional flow of branch Ht at

$\Omega/\Omega_c = 100$ (solid line), the three-dimensional flow of branch Mt at $\Omega/\Omega_c = 10.0$ (dashed line), and the chaotic flow shown in figure 5.29 (dotted line). Following the example of Jiménez, the independent variables are scaled by the root mean squared vorticity ω'.

The probability density function of the longitudinal velocity gradient in the x-direction is shown in figure 6.9. The moments of the distribution of the two-dimensional flows are listed in table 6.3, along with those obtained by Jiménez at $R_\lambda = 62$. The large discrepancy in this table is due to our results being for two-dimensional solutions, and we see better agreement in the later tables when we compare three-dimensional solutions.

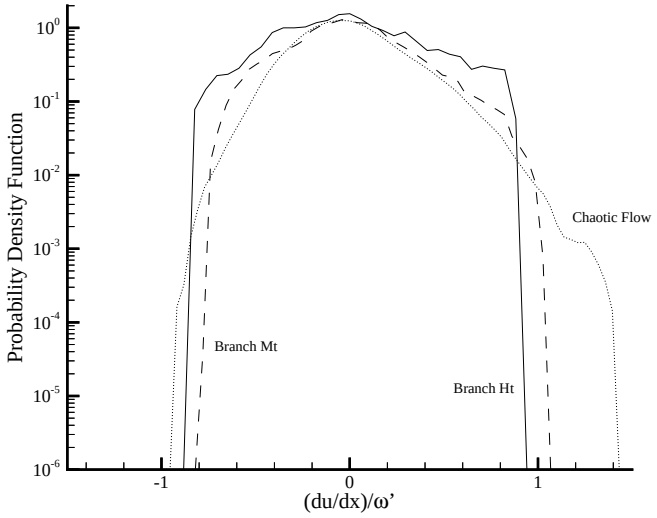

Figure 6.9: One-Dimensional Probability Density Function for the Longitudinal Velocity Gradient

	Jiménez	Branch Gt	Branch Ht
R_λ	61.1	43.036	68.454
$-F_3$	0.495	0.09846	0.2475
F_4	4.6	3.593	2.666
$-F_5$	8.0	0.9257	1.436
F_6	55	18.160	9.784

Table 6.3: Comparison of Turbulence Statistics for Two-Dimensional Flows: Branch Gt at $\Omega/\Omega_c = 20.0$ and Branch Ht at $\Omega/\Omega_c = 100.0$

In tables 6.4 and 6.5 we compare the skewnesses and flatnesses of the three-dimensional

branch Mt and Chaotic flow with those found by Jiménez for turbulent flow. The skewness can also be observed in figure 6.9, especially for the chaotic flow, by noting that the curves are not symmetric since they extend further out to the right on the graph.

Although our Taylor Reynolds number is lower than that of Jiménez, we can still see that our solutions are non-Gaussian, and the magnitudes of the skewnesses and flatnesses are approaching those observed in turbulent flow. We note that the affect of the anisotropic forcing is reduced in the Chaotic flow.

	Gaussian	Jiménez	Current x	Current y	Current z
R_λ		35.1	18.427	17.736	1.198
$-F_3$	0	0.490	0.2847	-0.2238	0.006644
F_4	3.0	4.2	3.159	3.310	3.519
$-F_5$	0	6.5	2.707	-1.896	0.4445
F_6	15	40	15.466	17.095	19.575

Table 6.4: Comparison of Turbulence Statistics for Branch Mt at $\Omega/\Omega_c = 10.0$

	Gaussian	Jiménez	Current x	Current y	Current z
R_λ		35.1	21.030	13.514	7.622
$-F_3$	0	0.490	0.5220	0.06254	0.2333
F_4	3.0	4.2	3.674	3.471	3.250
$-F_5$	0	6.5	5.528	0.9849	2.370
F_6	15	40	26.271	21.143	19.360

Table 6.5: Comparison of Turbulence Statistics for Chaotic Flow

The vorticity histogram, figure 6.10, shows that our steady state solutions have a larger region with high vorticity than the chaotic flow that we are comparing our data with. This appears to be contrary to the findings of Jiménez who shows that as the Taylor Reynolds number of the turbulent flow is increased, the histogram extends further, indicating larger regions of high vorticity.

In figure 6.11 we show the histogram of the volume fraction for the strain. Unlike the vorticity histogram, this histogram behaves in the manner observed by Jiménez. The volume occupied by large strain forces increases as the flow becomes more chaotic.

In figure 6.12 we show the joint probability densities of vorticity verses strain for branch Mt and chaotic flow. The density contours in these joint probability density functions are

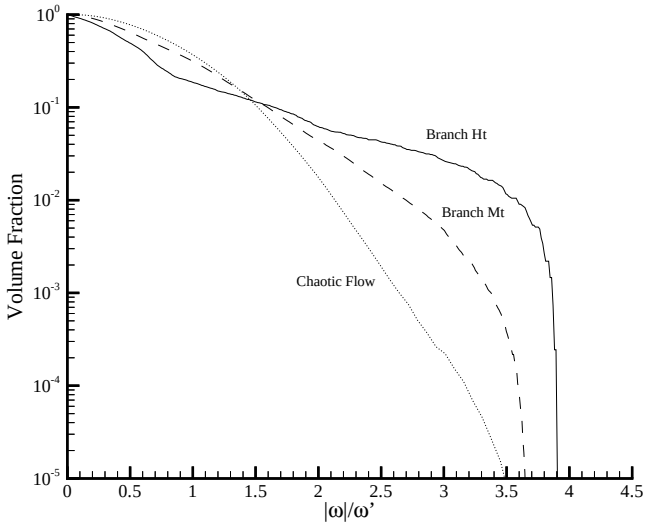

Figure 6.10: One-Dimensional Histogram of the Volume Fraction Occupied by Points Above a Certain Threshold of Vorticity for Branch Mt, $\Omega/\Omega_c = 10.0$, and Chaotic Flow

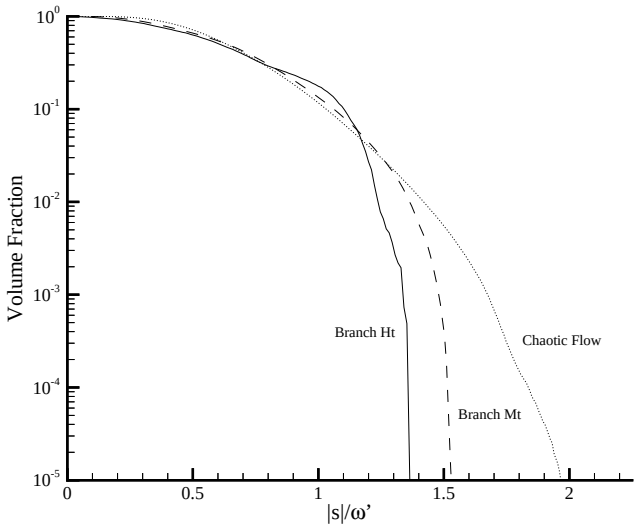

Figure 6.11: One-Dimensional Histogram of the Volume Fraction Occupied by Points Above a Certain Threshold of Strain for Branch Mt, $\Omega/\Omega_c = 10.0$, and Chaotic Flow

spaced logarithmically by a factor of 10.

We note the large difference between these two plots. Branch Mt extends further in vorticity direction; however, the strain is lower than that of the chaotic flow. Also branch Mt drops off much faster than chaotic flow, and we fail to observe the tails on probability density functions that are present in high Taylor Reynolds number turbulent flows.

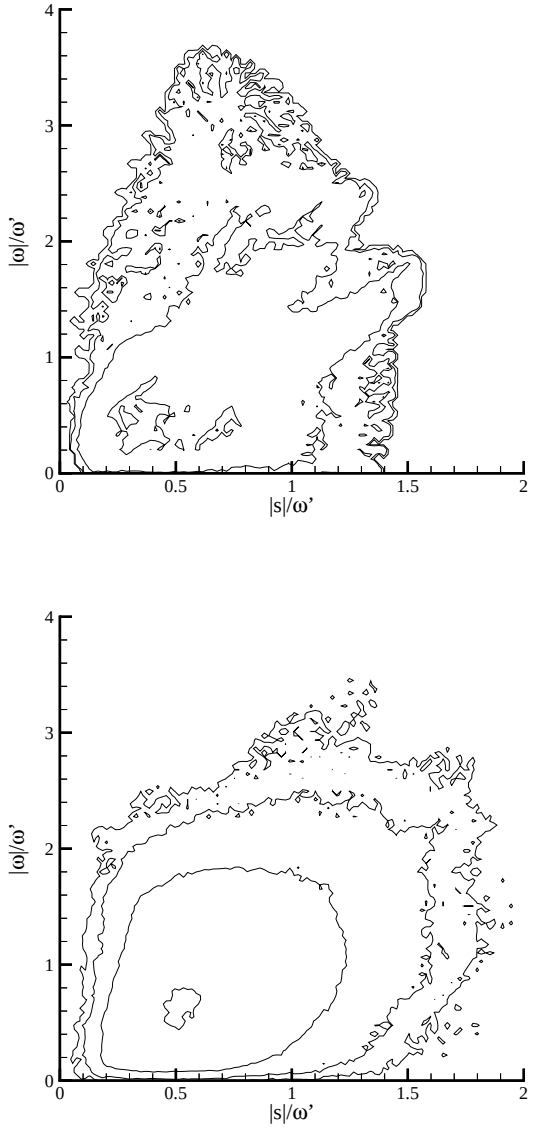

Figure 6.12: Joint Probability Density Function of Vorticity Versus Strain Rate for Branch Mt (Top) and Chaotic Flow. Density Contours Are Spaced Logarithmically by a Factor of 10.

Chapter 7 Flow Between Concentric Rotating Cylinders

We consider the non-dimensionalized incompressible Navier-Stokes equations, which in cylindrical coordinates are

$$\frac{\partial u}{\partial t} + (\mathbf{u}.\nabla)u - \frac{v^2}{r} = -\frac{\partial p}{\partial r} + \frac{1}{R}\left(\nabla^2 u - \frac{u}{r^2} - \frac{2}{r^2}\frac{\partial v}{\partial \theta}\right), \tag{7.1}$$

$$\frac{\partial v}{\partial t} + (\mathbf{u}.\nabla)v + \frac{uv}{r} = -\frac{1}{r}\frac{\partial p}{\partial \theta} + \frac{1}{R}\left(\nabla^2 v + \frac{2}{r^2}\frac{\partial u}{\partial \theta} - \frac{v}{r^2}\right), \tag{7.2}$$

$$\frac{\partial w}{\partial t} + (\mathbf{u}.\nabla)w = -\frac{\partial p}{\partial z} + \frac{1}{R}\nabla^2 w, \tag{7.3}$$

$$\frac{1}{r}\frac{\partial}{\partial r}(ru) + \frac{1}{r}\frac{\partial v}{\partial \theta} + \frac{\partial w}{\partial z} = 0, \tag{7.4}$$

where

$$(\mathbf{u}.\nabla) \equiv u\frac{\partial}{\partial r} + \frac{v}{r}\frac{\partial}{\partial \theta} + w\frac{\partial}{\partial z}, \tag{7.5}$$

$$\nabla^2 \equiv \frac{\partial^2}{\partial r^2} + \frac{1}{r}\frac{\partial}{\partial r} + \frac{1}{r^2}\frac{\partial^2}{\partial \theta^2} + \frac{\partial^2}{\partial z^2}. \tag{7.6}$$

We look for solutions of these equations on a domain between two concentric rotating circular cylinders. This domain is defined with two aspect ratios, the ratio of the cylinder radii, η, and the ratio of the gap width to the axial wavelength, Γ, yielding

$$R_1 \equiv \frac{\eta}{1-\eta} \leq r \leq \frac{1}{1-\eta} \equiv R_2, \tag{7.7}$$

$$0 \leq \theta \leq 2\pi, \tag{7.8}$$

$$0 \leq z \leq \Gamma. \tag{7.9}$$

We assume the ratio of the angular speed of the outer cylinder to the inner cylinder is

given by ω. On the cylindrical surfaces, $r = R_1, R_2$, we impose no slip boundary conditions:

$$u(R_1, \theta, z) = u(R_2, \theta, z) = 0, \tag{7.10}$$

$$v(R_1, \theta, z) = 1, \qquad v(R_2, \theta, z) = \omega, \tag{7.11}$$

$$w(R_1, \theta, z) = w(R_2, \theta, z) = 0, \tag{7.12}$$

where $0 \leq \theta \leq 2\pi$ and $0 \leq z \leq \Gamma$. In the θ and z directions, we have periodic boundary conditions.

Throughout this chapter we set $\eta = 0.875$, $\Gamma = 2.54$ and $\omega = 0$. This allows us to compare our results with the experimental work of Coles [9], and the numerical results of Schröder and Keller [30].

An exact solution for this system when $\omega = 0$ is Couette flow:

$$u = w = 0, \tag{7.13}$$

$$v = \frac{\eta}{1 - \eta^2}\left(\frac{R_2}{r} - \frac{r}{R_2}\right), \tag{7.14}$$

$$\frac{\partial p}{\partial r} = \frac{v^2}{r}. \tag{7.15}$$

7.1 Numerical Implementation

We use the same numerical method of solving the linear system in Newton's method as described in chapter 3 to compute Taylor-Vortex flows. However, the discretization and reduction from a DAE to an ODE is altered slightly to take into account the non-periodic radial boundary conditions.

We improve efficiency by computing solutions on the smaller domain:

$$0 \leq \theta \leq \frac{2\pi}{q}, \qquad q \in \mathbb{N}; \tag{7.16}$$

on which periodic boundary conditions are imposed. The advantages of doing this are that we require less azimuthal modes to get an accurate solution of a flow that has q waves around the cylinder, and there are fewer bad eigenvalues for RPM to detect when computing these solutions. Furthermore, it also allows us to obtain solutions similar to existing ones, but with a different number of waves around the cylinder, by numerically continuing in q.

During this chapter the number that we append to references of Spiral and Wavy Taylor Vortex flows is q which is equal to the number of waves the solution has around the cylinder.

We approximate the velocity and pressure fields with finite Fourier series in the azimuthal and axial direction. The radial direction is discretized using finite differences rather than Chebyshev polynomials since they are simpler to implement and they impose a less stringent time step criterion.

We introduce N_r equally spaced points $\{r_n\}$ in the radial direction at which we approximate the velocity and pressure fields. Furthermore, we use N_θ and N_z basis functions in the azimuthal and axial directions respectively to approximate the velocity and pressure fields. This yields the expansion

$$u(r_n, \theta, z) \equiv \frac{1}{N_\theta N_z} \sum_{k_\theta, k_z} \hat{u}_{nk_\theta k_z} e^{-ik_\theta \theta} e^{-ik_z z}, \tag{7.17}$$

where $-N_\theta/2 \leq k_\theta < N_\theta/2$, and $-N_z/2 \leq k_z < N_z/2$.

The approximations to radial derivatives use centred finite differences in the interior. At the boundaries second order one-sided differences are used. The approximations at the inner boundary are

$$\frac{\partial u}{\partial r} \approx \frac{-3u_0 + 4u_1 - u_2}{2\Delta r}, \qquad \frac{\partial^2 u}{\partial r^2} \approx \frac{-7u_0 + 8u_1 - u_2}{2\Delta r^2}. \tag{7.18}$$

The approximations at the outer boundary are similar.

The azimuthal and axial derivatives are computed in the same way as described in chapter 3. The non-linear terms are evaluated using collocation as described there.

Using these approximations the terms in the r-momentum equation, excluding the pressure, are

$$\begin{aligned}\hat{F}_{nk_\theta k_z} \equiv \frac{1}{R}\Bigg(&\frac{\partial^2 \hat{u}_{nk_\theta k_z}}{\partial r^2} + \frac{1}{r}\frac{\partial \hat{u}_{nk_\theta k_z}}{\partial r} - \frac{k_\theta^2}{r^2}\hat{u}_{nk_\theta k_z} - k_z^2 \hat{u}_{nk_\theta k_z} - \frac{\hat{u}_{nk_\theta k_z}}{r^2} + \frac{2ik_\theta}{r^2}\hat{v}_{nk_\theta k_z}\Bigg) \\ &- col(u, \frac{\partial u}{\partial r})_{nk_\theta k_z} - \frac{1}{r_n} col(v, \frac{\partial u}{\partial \theta})_{nk_\theta k_z} - col(w, \frac{\partial u}{\partial z})_{nk_\theta k_z} + \frac{1}{r_n} col(v, v)_{nk_\theta k_z}. \end{aligned} \tag{7.19}$$

The terms in the other momentum equations and the continuity equation are evaluated similarly.

7.1.1 Integrating the Continuity Equation

We use the continuity equation to compute the radial velocity. For each pair of azimuthal/axial wavenumbers, we have a first order boundary value problem; however, there are two boundary conditions.

We consider different methods of solving this boundary value problem. Firstly we use centred differences which where also used by Keller and Von Sosen [19]. Centred differences yield the following discretization of the continuity equation:

$$\frac{\hat{u}_{n+1,k_\theta k_z} - \hat{u}_{n-1,k_\theta k_z}}{2\Delta r} + \frac{\hat{u}_{nk_\theta k_z}}{r_n} + \frac{ik_\theta \hat{v}_{nk_\theta k_z}}{r_n} + ik_z \hat{w}_{nk_\theta k_z} = 0. \tag{7.20}$$

We note that with centred differences we are able to enforce both boundary conditions, $\hat{u}_{0,k_\theta k_z} = 0$ and $\hat{u}_{N_r,k_\theta k_z} = 0$. The matrices resulting from this discretization are non-singular, but they become more ill-conditioned as the resolution is increased.

By integrating the boundary value problem from one boundary using one-sided differences, we get the trapezoidal rule:

$$\frac{r_{n+1}\hat{u}_{n+1,k_\theta k_z} - r_n \hat{u}_{nk_\theta k_z}}{r_{n+1/2}\Delta r} + \frac{ik_\theta(\hat{v}_{n+1,k_\theta k_z} + \hat{v}_{nk_\theta k_z})}{2r_{n+1/2}} + \frac{ik_z(\hat{w}_{n+1,k_\theta k_z} + \hat{w}_{nk_\theta k_z})}{2} = 0. \tag{7.21}$$

This integration does not enforce both boundary conditions. However, we can integrate from both boundaries which yields two values for the radial velocity: $u_i(r)$ and $u_o(r)$, the radial velocity integrated from the inner and outer boundaries respectively. We consider the cases when in the interior we take either $u_i(r)$, $u_o(r)$, their average $(u_i(r) + u_o(r))/2$, or a weighted average $[(r - r_o)u_i(r) + (r - r_i)u_o(r)]/(r_o - r_i)$. At both boundaries we always set the radial velocity equal to zero.

Tables 7.1-7.3 show the relative errors of the different methods. The exact solution in table 7.1 is Couette flow (7.15), while in tables 7.2 and 7.3 the 'exact' solution is the Richardson extrapolation of two high resolution numerical solutions. The different discretizations also have different constraints on the time step we can take while still maintaining stability.

From these tables we observe that using the one-sided average method to calculate the radial velocity gives the smallest error, particularly with regard to the wavespeed of the wavy Taylor vortices. For Couette flow all the 2-Norm errors are the same because the radial velocity is zero.

Method	2-Norm	Norm Error
Exact Solution	0.566993369875	
Centred Differences	0.567147904071	1.55×10^{-4}
One-Sided Averaged	0.567147904071	1.55×10^{-4}
One-Sided Weighted Average	0.567147904071	1.55×10^{-4}

Table 7.1: Comparison of Different Methods for Integrating the Continuity Equation for Couette Flow, 32 Radial Points, Reynolds Number=150

Method	2-Norm	Norm Error
'Exact' Solution	0.553776604290	
Centred Differences	0.555266256559	1.49×10^{-3}
One-Sided Averaged	0.554255692691	4.79×10^{-4}
One-Sided Weighted Average	0.555544124990	1.77×10^{-3}

Table 7.2: Comparison of Different Method for Integrating the Continuity Equation for Taylor-Vortex Flow, 32 Radial Points, Reynolds Number=150

Method	2-Norm	Wavespeed	Wavespeed Error
'Exact' Solution	0.548840092843	0.0619259124247	
Centred Differences	0.551444646295	0.0626897820008	7.64×10^{-4}
One-Sided Averaged	0.549163307741	0.0619635860646	3.77×10^{-5}
One-Sided Weighted Average	0.551715796450	0.0625491778658	6.23×10^{-4}

Table 7.3: Comparison of Different Method for Integrating the Continuity Equation for Wavy Taylor-Vortex-4 Flow, 32 Radial points, Reynolds Number=200

7.1.2 Computing the Pressure

As in Kolmogorov flow a Poisson equation for the pressure is obtained by taking the divergence of the momentum equations (7.1)-(7.3).

The equation at each interior point in the radial direction is given by

$$\frac{\hat{p}_{n+1,k_\theta k_z} - 2\hat{p}_{nk_\theta k_z} + \hat{p}_{n-1,k_\theta k_z}}{\Delta r^2} + \frac{\hat{p}_{n+1,k_\theta k_z} - \hat{p}_{n-1,k_\theta k_z}}{2r_n\Delta r} - \frac{k_\theta^2}{r_n^2}\hat{p}_{nk_\theta k_z} - k_z^2\hat{p}_{nk_\theta k_z}$$
$$= \frac{\hat{F}_{n+1,k_\theta k_z} - \hat{F}_{n-1,k_\theta k_z}}{2\Delta r} + \frac{\hat{F}_{nk_\theta k_z}}{r_n} - \frac{ik_\theta}{r_n}\hat{G}_{nk_\theta k_z} - ik_z\hat{H}_{nk_\theta k_z}. \quad (7.22)$$

Neumann boundary conditions are obtained by requiring the r-momentum equation to be satisfied on the boundary:

$$\frac{-3\hat{p}_{0k_\theta k_z} + 4\hat{p}_{1k_\theta k_z} - \hat{p}_{2k_\theta k_z}}{2\Delta r} = \hat{F}_{0k_\theta k_z}. \quad (7.23)$$

There is a similar equation for the outer boundary.

Now for each pair of azimuthal/axial wavenumbers, we have an almost tridiagonal system for the pressure. This is solved by LU decomposition. However, when both the azimuthal and axial wavenumbers are zero, the system is singular. For this case we set the variables $\hat{p}_{n00}$ equal to zero, since the θ and z derivatives, which are used in the θ and z-momentum equations respectively, are equal to zero. Additionally the radial derivative of the pressure is not used during our calculation, since we do not determine the radial velocity using the r-momentum equation.

7.1.3 Order of Convergence

In table 7.4-7.6 we show that our solutions are second order accurate in Δr. Note the exact figure in table 7.4 is computed by integrating the analytic solution (7.15), while in tables 7.5 and 7.6 we take 'exact' solution to be the Richardson extrapolation of the two highest resolution solutions.

We observe from table 7.6 that 32 radial points determines the wavespeed with sufficient accuracy. In section 7.3.1 we show that our computed wavespeeds are in good agreement with those from other studies.

Radial Points	2-Norm	Error in 2-Norm
16	0.567611244294	6.18×10^{-4}
32	0.567147904071	1.55×10^{-4}
64	0.567032007527	3.86×10^{-5}
128	0.567003029541	9.66×10^{-6}
Exact	0.566993369875	

Table 7.4: Second Order Convergence for Couette Flow, Re=150

Radial Points	2-Norm	Error
16	0.555755476188	2.0×10^{-3}
32	0.554255692691	5.2×10^{-4}
64	0.553896376391	1.6×10^{-4}
128	0.553778714431	3.9×10^{-5}
'Exact'	0.553740160443	

Table 7.5: Second Order Convergence for Taylor-Vortex Flow, Re=150

Radial Points	Norm	Wavespeed	Wavespeed Error
16	0.550791085190	0.0623586172114	4.3×10^{-4}
32	0.549163307741	0.0619635860646	3.8×10^{-5}
64	0.548920896568	0.0619353308347	9.4×10^{-6}
'Exact'	0.548840092843	0.0619259124247	

Table 7.6: Second Order Convergence for Wavy Taylor Vortex 4 Flow, Re=200

7.2 Bifurcations from Couette Flow

Bifurcations from Couette flow to Taylor-Vortex flow have been calculated both computationally and experimentally.

Meyer-Spasche and Keller [27], as well as Dinar and Keller [11], calculated the bifurcation points for many different Taylor-Vortex flows, with different numbers of vortices in the radial and axial directions, and various aspect ratios.

In figure 7.1 we observe the use of RPM to detect bifurcation points. The small squares represent real eigenvalues, while the small diamonds represent the real part of a complex conjugate pair of eigenvalues. We randomly perturb the solution at the beginning of every continuation step to break the symmetry so that RPM detects all of the bifurcation points. The large symbols indicate the location of the bifurcation points.

Without this random perturbation RPM fails to detect those eigenvalues belonging to eigenvectors which are orthogonal to the solution. This is due to the method we use to find the bad subspace, which examines the iterates of the time-stepping iteration. Therefore, if an eigenvector is not present in the time-stepping iteration, it will not be detected by RPM.

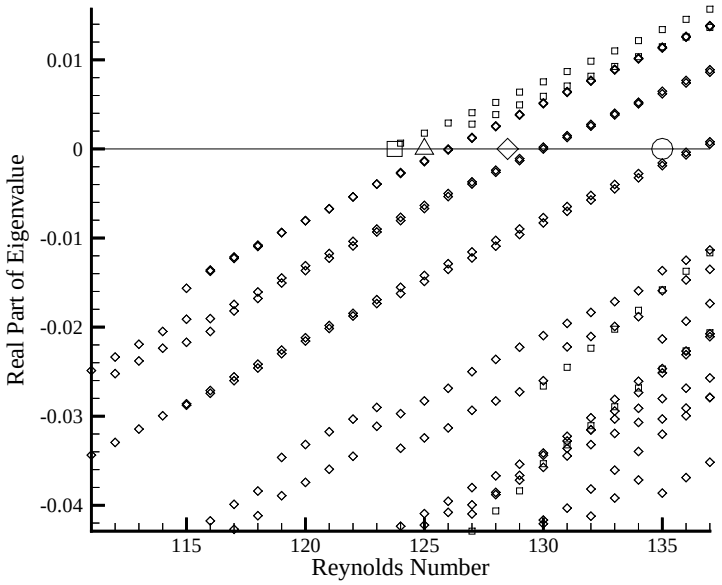

Figure 7.1: Eigenvalues for Couette Flow

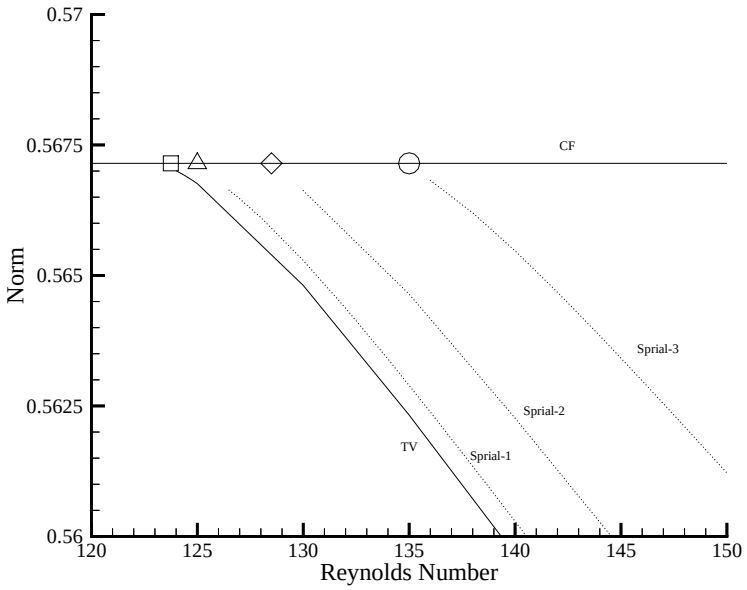

Figure 7.2: Norm vs. Reynolds Number for Taylor Vortices and Spiral Vortices Bifurcating from Couette Flow

Figure 7.1 shows one real eigenvalue appearing at about $Re \approx 124$. This agrees with the bifurcation diagram, figure 7.2, where the Taylor-Vortex flow branch bifurcates from the Couette flow branch at $Re \approx 124$. This eigenvalue was not observed by RPM before it became unstable because at each step we converged to the solution before it was necessary to add that eigenvector. A second eigenvalue appears three continuation steps later. This is the second of the eigenvalues that correspond to the bifurcation of Taylor-Vortex flow.

Additionally there are bifurcations to Spiral Vortices. In experiments these branches are only observed for counter-rotating cylinders, since they are unstable when the outer cylinder is stationary. The spiral vortices bifurcate when two equal pairs of complex conjugate eigenvalues cross the imaginary axis. There are two pairs due to the translation invariance of the solution in the azimuthal and axial directions. The spiral vortex branches are travelling wave solutions. As discussed in section 5.6, the angular speed, ω, of a bifurcating travelling wave branch can be determined from the imaginary component β of the eigenvalue using

$$\omega = \frac{\beta L}{2\pi}, \tag{7.24}$$

where L is the wavelength of the travelling wave solution. In our case when there are k waves around the cylinder $L = 2\pi/k$, we have

$$\omega = \frac{\beta}{k}. \tag{7.25}$$

The bifurcating branches in figure 7.2 are not shown to join the Couette branch, because the Recursive Projection Method fails to give convergence when the eigenvalues of the fixed point iteration are too near to unity. However, we are able to continue close enough to the bifurcation points to observe that the eigenvalues in figure 7.1 do not change sign at the same location as we find the bifurcations points. This is due to the inaccuracy of the unstable subspace of RPM.

The other eigenvalues that can be seen in figure 7.1 correspond to bifurcation to Spiral Vortices with larger pitch angles, and to Taylor Vortices with more vortices in the axial direction.

As shown in table 7.7, the wavespeed estimated using (7.25) is in reasonable agreement with the wavespeed observed from the numerical solution. The accuracy of the predicted wavespeed is limited by the accuracy of the invariant subspace of RPM.

Branch	β	Estimated Wavespeed	Observed Wavespeed
Spiral-1	0.0687	0.0687	0.0684
Spiral-2	0.1388	0.0694	0.0688
Spiral-3	0.2088	0.0696	0.0693

Table 7.7: Comparison of Predicted and Computed Wavespeeds for Spiral Flows

The difference between Taylor-Vortex flow and Spiral-Vortex flow is shown in figure 7.3. In this two-dimensional projection of the velocity field of the spiral flow, the bottom vortex is a sink while the top vortex is a source.

In figure 7.4 we show the pitch angles for different spiral flows. For each spiral branch there is another similar branch that has the spirals going up the cylinder rather than down.

Following Moulic and Yao we observe, see figure 7.5, that the spiral vortex solutions have a net axial flow of fluid. This is defined as

$$\int_0^{\Gamma} \int_0^{2\pi} \int_{R_1}^{R_2} w(r, \theta, z) dr d\theta dz. \tag{7.26}$$

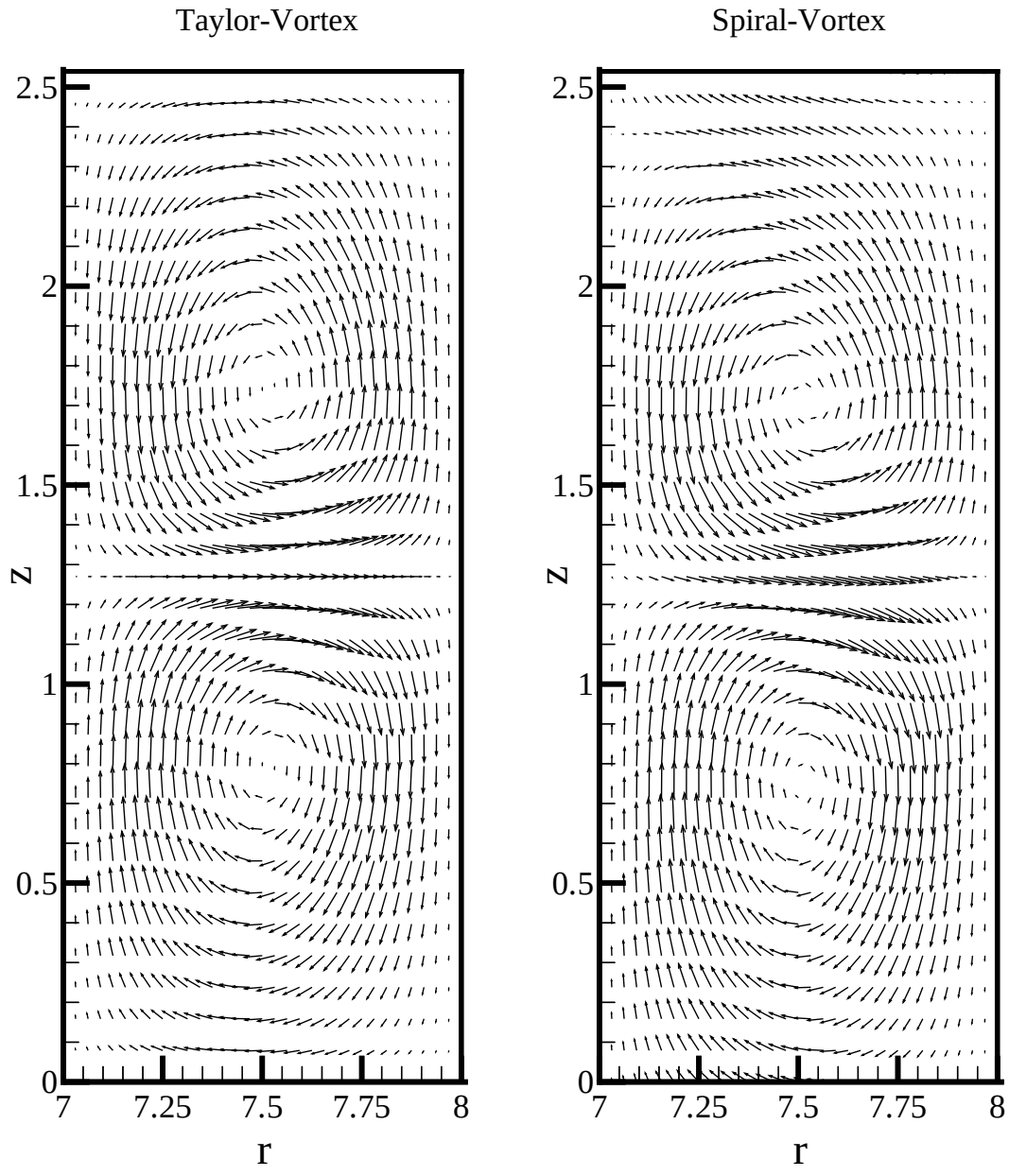

Figure 7.3: Comparison of Taylor-Vortex and Spiral Flow at Reynolds Number 200

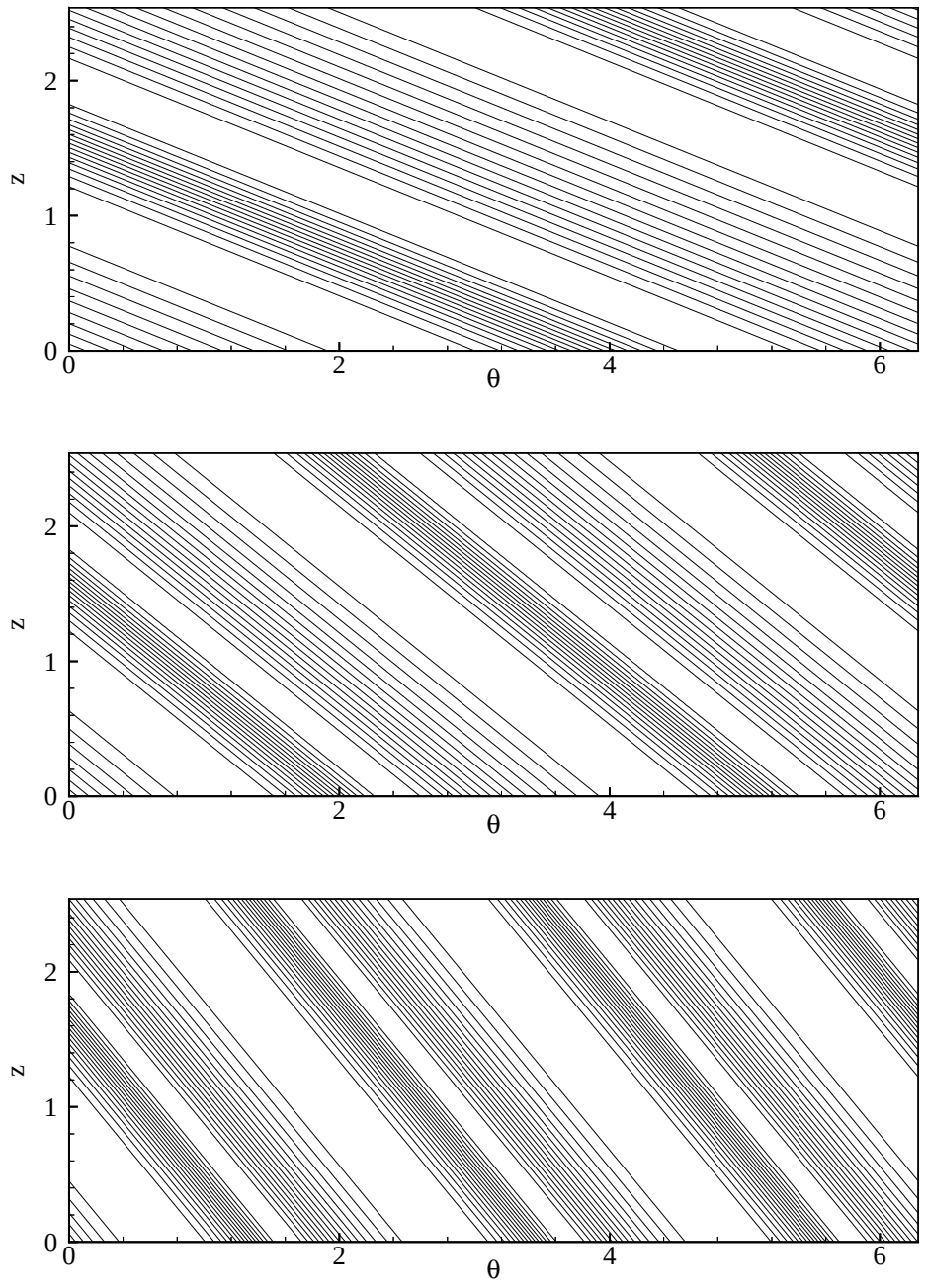

Figure 7.4: Comparison of the Different Spiral Flows: w-Contours at Reynolds Number 200, $r = R_1 + 1/4$

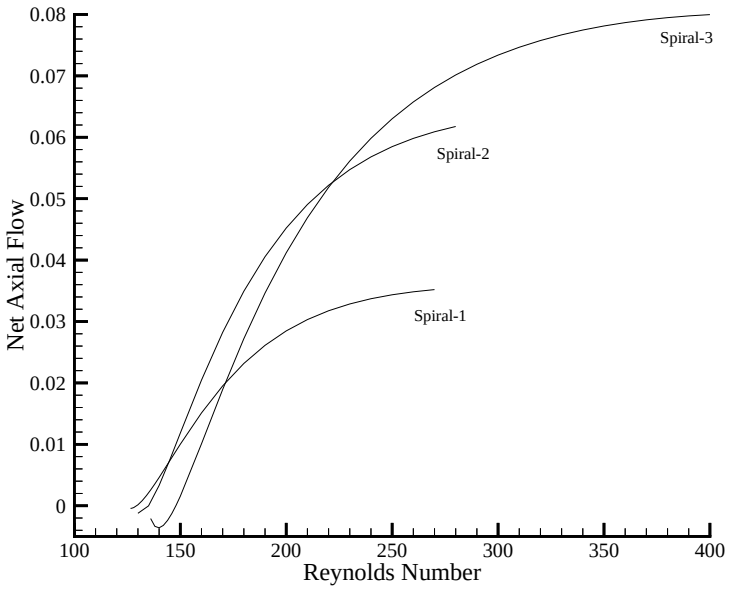

Figure 7.5: Net Axial Flow of Fluid for Spiral Vortices

7.3 Bifurcation to Wavy Vortices

As the Reynolds number is increased there are various symmetry breaking Hopf bifurcations from Taylor Vortex flow, that produce travelling wave solutions. The difference between these bifurcating branches is the number of waves around the cylinder, as shown in figure 7.6. Figure 7.7 shows how the wavy flow, with period $\pi/2$, varies around the cylinder. Figure 7.8 shows that there are vortex tubes in the Wavy Taylor Vortex flow. These tubes remain attached to the walls of the cylinder.

As in the previous section, we again use RPM to detect the bifurcations to wavy vortices. This can also be done while continuing along the Taylor-Vortex and the Spiral-Vortex branches.

We find that there are many Hopf bifurcations along the Taylor-Vortex branch. They each correspond to the bifurcation of a Wavy Taylor Vortex solution branch. The bifurcation diagram for these branches is shown in figure 7.9, while table 7.8 lists the locations of the bifurcation points.

In figure 7.10, we observe that initially after the bifurcation point the wavespeed along

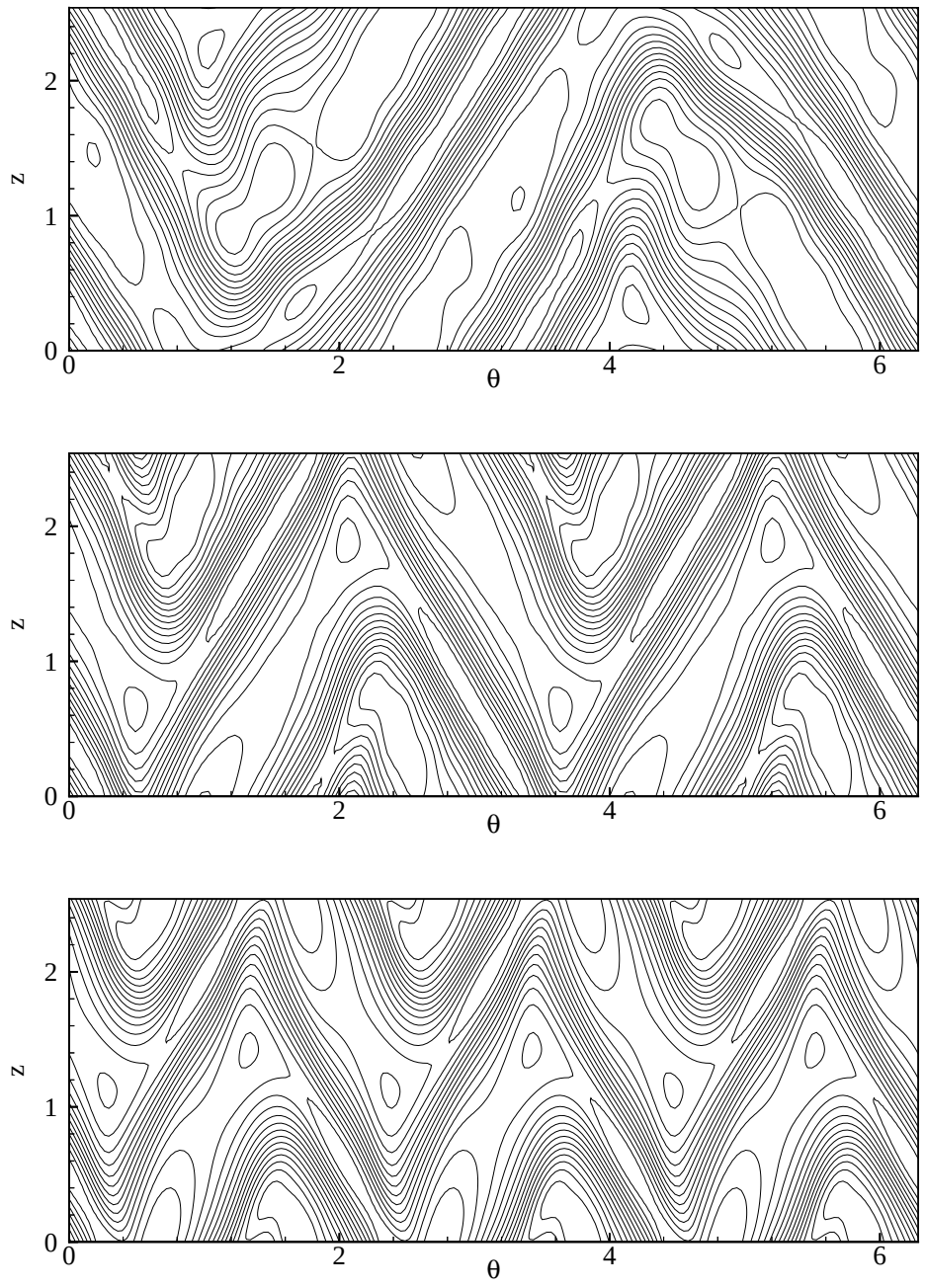

Figure 7.6: Comparison of Different Wavy Taylor Vortex Flows: w-Contours at Reynolds Number 200, $r = R_1 + 1/4$. Top Period is 2π, Middle is π, and Bottom is $2\pi/3$.

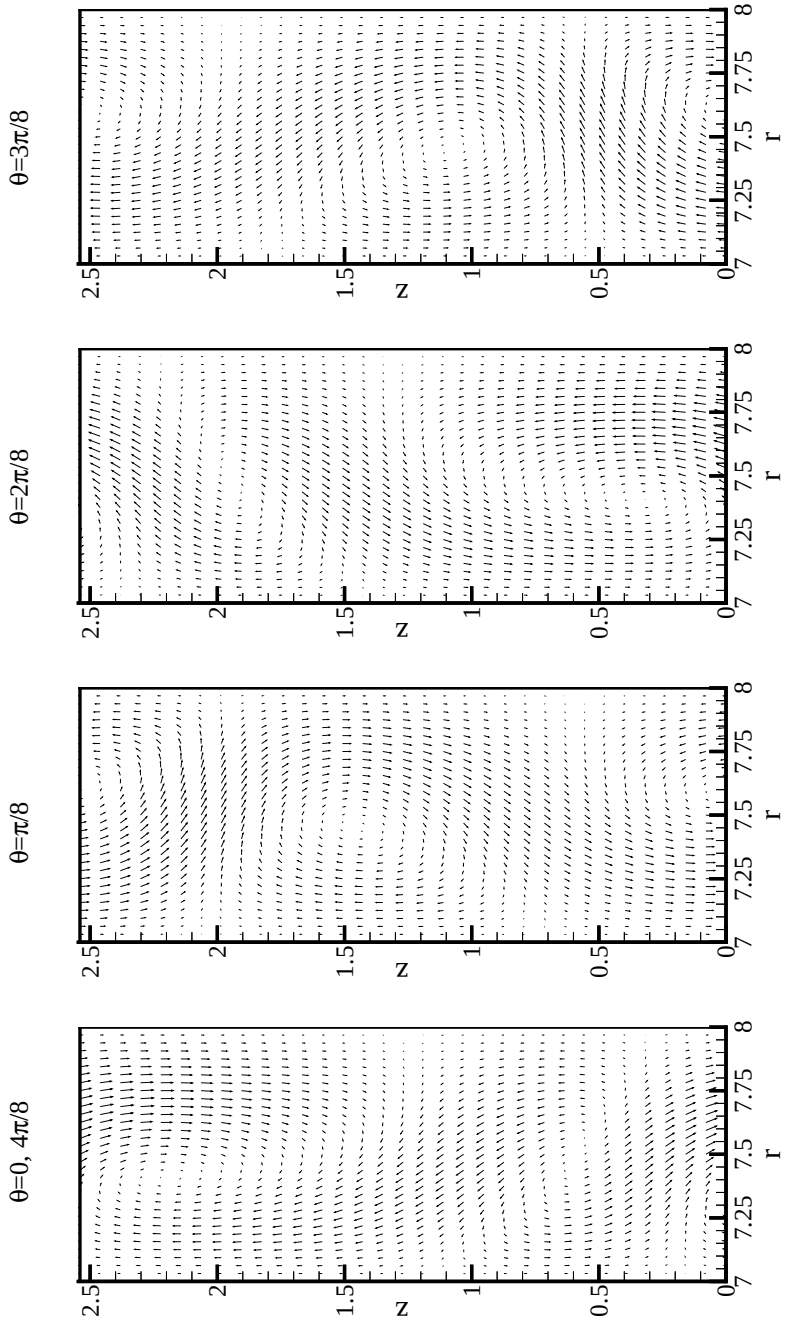

Figure 7.7: Cross Sections of Wavy Taylor Vortex 4 Flow at Various Locations Around the Cylinder, Re=200

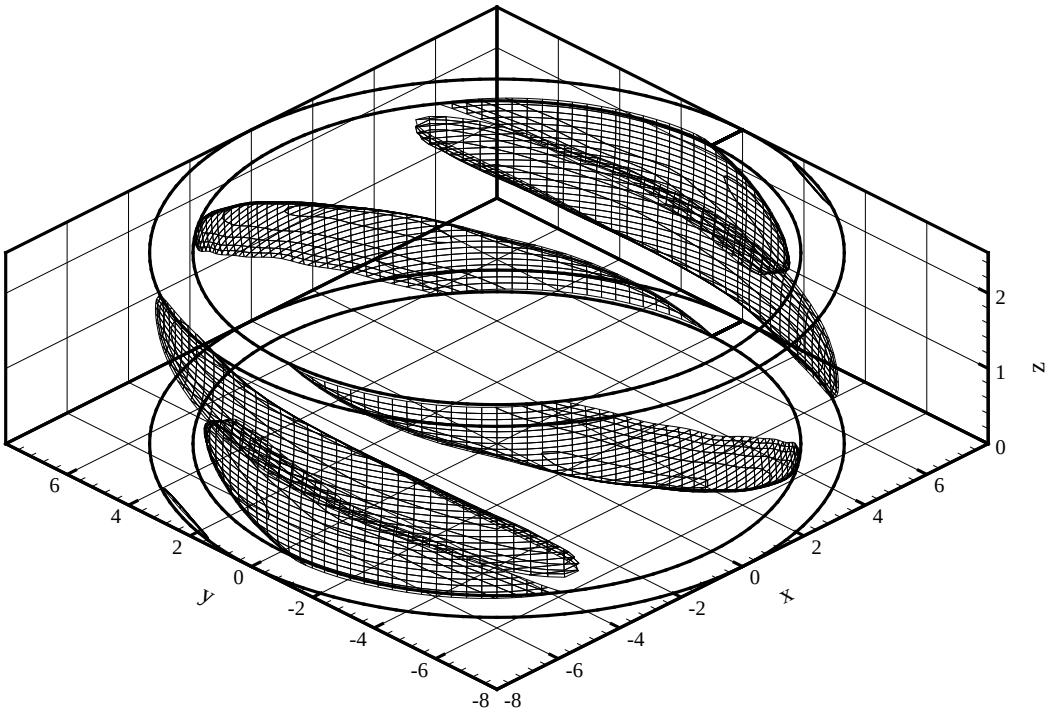

Figure 7.8: Vorticity Isosurface for Wavy Taylor Vortex 1 Flow, Re=200

Branch	Reynolds Number (to 2 d.p.)
WTV-3	143.91
WTV-4	149.41
WTV-5	155.61
WTV-6	162.53

Table 7.8: Bifurcation Points for Wavy Taylor Vortices

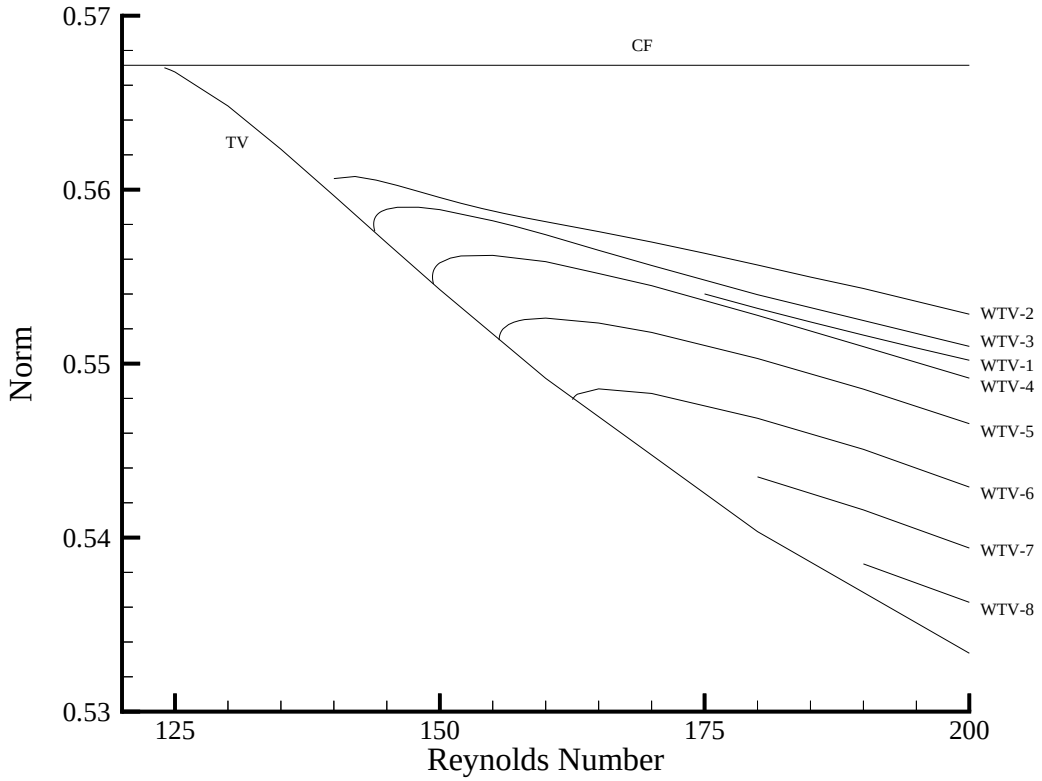

Figure 7.9: Norm of Wavy Taylor Vortex Branches Bifurcating from the Taylor Vortex Branch

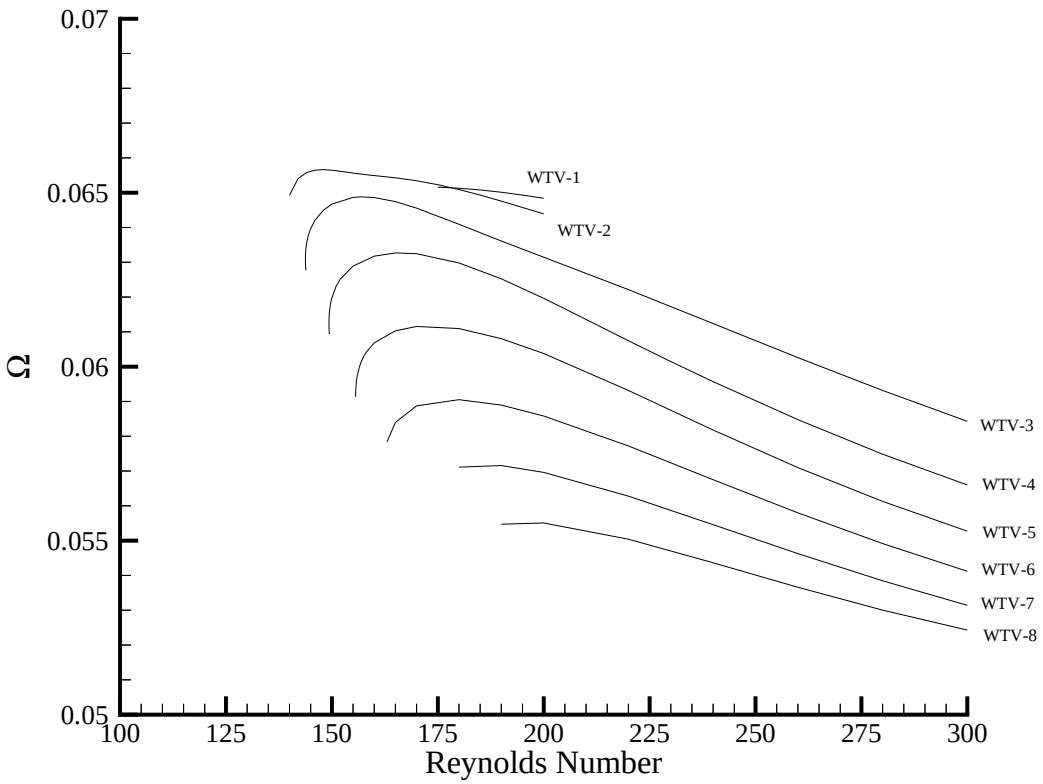

Figure 7.10: Wavespeed vs. Reynolds Number for Wavy Taylor Vortex Flow

the wavy Taylor vortex branch increases as the Reynolds number is increased. However, it shortly reaches a maximum and starts decreasing. Experimentally and analytically it has been shown that, as the Reynolds number is increased, the wavespeed decreases monotonically asymptoting to an η dependent value. However, we have not followed these branches far enough to be able to compare with these results.

There are also Hopf bifurcation points along the Spiral-Vortex flow branches. However, we are so far unable to follow these Wavy-Spiral flows. They are no longer travelling wave solutions as the wavy portion moves at a different speed from the spiral flow.

Figure 7.11 shows some detail of the behaviour of the bifurcated Wavy Taylor Vortex flow branches near their bifurcations. Branches with 3, 4 or 5 waves around the cylinder arise from subcritical Hopf bifurcations. The bifurcating branch has a fold on it close to the bifurcation point. However, branches with 6 (or more) waves around the cylinder come from supercritical Hopf bifurcations. Note that for the 5 wave solution, with 32 points radially, the fold is not detected, but with 64 radial points the fold is barely apparent.

Also note that the fold persists as we increase the resolution. In fact the difference in Reynolds Number between the fold and the bifurcation point increases as the resolution is increased.

The same formula used for spiral flow, (7.25), to determine the wavespeed of the bifurcating travelling waves, is again used to determine the wavespeed of the wavy Taylor vortices.

7.3.1 Comparison of Wave Speeds by Various Authors

Marcus [25] claims that the best way to show the accuracy of a numerical simulation is to compare wave speeds. So we do that with our results and those of King et al. [20], and Schröder and Keller [30].

Table 7.9 shows that our wavespeeds agree with those found by King who discretized radially with Chebyshev polynomials while we used finite differences. The accuracy of our finite difference discretization can be improved by using Richardson Extrapolation. To compare wavespeeds we multiplied ours by the inner radius to agree with their scaling. Recall that η is the ratio of the cylinder radii, and q is the number of azimuthal waves.

In table 7.10 we see that there is a larger difference between the wavespeed from these calculations and those observed by Schröder and Keller. We believe our results are more

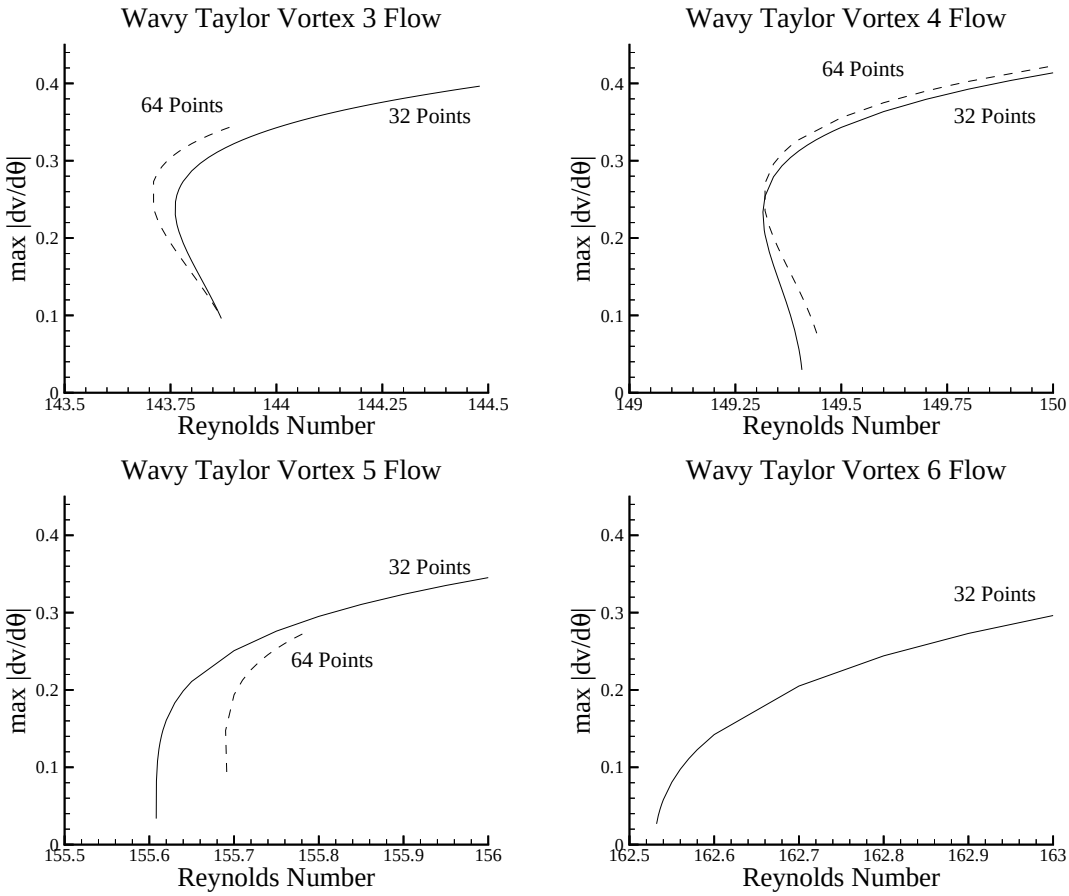

Figure 7.11: Bifurcations to Wavy Taylor Vortex Flows

η	Γ	Re	q	King	Present
0.868	2.40	458	6	0.3443	0.3494
0.868	3.00	458	6	0.3344	0.3385
0.875	3.00	243.5	4	0.401	0.4075
0.875	3.00	243.76	5	0.3893	0.3899
0.875	3.00	243.76	6	0.3757	0.3768
0.875	3.00	348.69	6	0.352	0.3540
0.875	3.00	459.8	6	0.342	0.3460

Table 7.9: Comparison of Wavespeeds with King et al. [20]

accurate since they did not use spectral methods in the azimuthal and axial directions. Furthermore, Schröder and Keller only used 16 grid points in the radial direction.

η	Γ	Re	q	Schröder	Present
0.875	2.54	180	4	0.421	0.4409
0.875	2.54	190	4	0.415	0.4377
0.875	2.54	201	4	0.410	0.4333

Table 7.10: Comparison of Wavespeeds with Schröder and Keller [30]

Chapter 8 Conclusions

From this research we have observed that the Recursive Projection Method provides an excellent method for performing numerical continuation on the incompressible Navier-Stokes equations. We successfully used RPM to calculate many branches of both Kolmogorov and Taylor-Vortex flows. Performance only depends on the structure of the eigenvalues of the differential equation, and on the iterative method used to find the steady state solutions. Therefore, when a good implicit method is used, the efficiency of RPM is unchanged.

Furthermore RPM provides a good basis for augmenting systems, especially with iterative where the bordering algorithm is less efficient. We augmented the Navier-Stokes equations with both a pseudo arc-length and a phase condition. We observed that the phase condition gave accurate results for the wave speed. However, the augmentation method needs to be improved to take into account that the system being satisfied changes when vectors are added to the unstable subspace.

We believe that turbulent flow originates from Kolmogorov flow through a series of bifurcations. We followed a few of these bifurcating branches and observed the existence of worm like structures in Kolmogorov flow at relatively low Reynolds numbers. We believe these transform into the worms that are present in turbulent flow.

To provide more accurate locations of the bifurcation points the accuracy of the eigenvalues provides by RPM needs to be improved. This lack of accuracy prevented us from explaining the hysteresis loop in the wavy Taylor-Vortex solutions which was observed by Coles [9].

One of the drawbacks of using RPM is the number of iterations required to isolate the unstable subspace. The current method can cause convergence problems when continuation is started on a branch with a large number of unstable eigenvectors, or when the dominant eigenvalues are not well separated.

Bibliography

[1] Andereck, C.D., Liu, S.S., Swinney, H.L., Flow Regimes in a Circular Couette System with independently Rotating Cylinders, *J. Fluid Mech.*, 164(1986), pp. 155-183.

[2] Apostol, T.M., Mathematical Analysis, A Modern Approach to Advanced Calculus, *Addison-Wesley*, 1957.

[3] Arnol'd, V.I., Kolmogorov's Hydrodynamic Attractors, *Proc. R. Soc. Lond. A*, 434(1991), pp. 19-22.

[4] Auchmuty, J.F.G., Bifurcating Waves, *Ann. New York Acad. Sci.*, 316(1979), pp. 263-278.

[5] Batchelor, G.K., The Theory of Homogenous Turbulence, *Cambridge University Press*, 1953.

[6] Bondarenko, N.F., Gak, M.Z., Dolzhansky, F.V., Laboratory and Theoretical Models of Plane Periodic Flows, *Atmospheric and Oceanic Physics*, 15(1979), pp. 711-716.

[7] Borue, V., Orszag, S.A., Numerical Study of Three-Dimensional Kolmogorov Flow at High Reynolds Numbers, *J. Fluid Mech.*, 306(1996), pp. 293-323.

[8] Bosek, J., Janovsky, V., A Note on the Recursive Projection Method, *Z. angew. Math. Mech.* 77(1997), pp. S437-S440.

[9] Coles, D., Transition in Circular Couette Flow, *J. Fluid Mech.* 21(1965), pp. 385-425.

[10] Davidson, B.D., Large-Scale Continuation and Numerical Bifurcation For Partial Differential Equations, *SIAM J. Numer. Anal.*, 34(5)(1997), pp. 2008-2027.

[11] Dinar, N., Keller, H.B., Computations of Taylor Vortex Flows Using Multigrid Continuation Methods, *Lecture Notes in Engineering*, 43, (Springer-Verlag, 1989), pp. 191-262.

[12] DOEDEL, E., KELLER, H.B., KERNEVEZ, J.P., Numerical Analysis and Control of Bifurcation Problems (II) Bifurcations in Infinite Dimensions, *Int. J. Bifurcation and Chaos*, 1(4)(1991), pp. 745-722.

[13] FEUDEL, F., SEEHAFER, N., GALANTI, B., RÜDIGER, S., Symmetry-Breaking Bifurcations for the Magnetohydrodynamic Equations with Helical Forcing, *Phys. Rev. E*, 54(3)(1996), pp. 2589-2596.

[14] GOLUBITSKY, M., STEWART, I., Hopf Bifurcation in the Presence of Symmetry, *Arch. Rat. Mech. Anal.*, 87(1985), pp. 107-165.

[15] GOLUBITSKY, M., STEWART, I., Symmetry and Stability in Taylor-Couette Flow, *SIAM J. Math. Anal.*, 17(2)(1986), pp. 249-287.

[16] GOTTLIEB, D., ORSZAG, S.A., Numerical Analysis of Spectral Methods: Theory and Applications, *SIAM*, 1977.

[17] GREEN, J.S.A., Two-Dimensional Turbulance Near the Viscous Limit, *J. Fluid Mech.*, 62(1974), pp. 273-287.

[18] JIMÉNEZ, J., WRAY, A.A., SAFFMAN, P.G., ROGALLO, R.S., The Structure of Intense Vorticity in Isotropic Turbulence, *J. Fluid Mech.*, 255(1993), pp. 65-90.

[19] KELLER, H.B., VON SOSEN, H., New Methods in CFD: DAE and RPM, *First Asian CFD Conference*, 1995.

[20] KING, G.P., LI, Y., LEE, W., SWINNEY, H.L., MARCUS, P.S., Wave speeds in wavy Taylor-vortex flow, *J. Fluid Mech.*, 141(1984), pp. 365-390.

[21] LEONARD, A., WRAY, A., A New Numerical Method for the Simulation of Three-Dimensional Flow in a Pipe, *Eighth International Conference on Numerical Method in Fluid Dynamics*, 1982.

[22] LIBIN, A., SIVASHINSKY, G., Long Wavelength Instability of the ABC-Flows, *Quarterly of Applied Mathematics*, 48(4)(1990), pp. 611-623.

[23] LUST, K., ROOSE, D., Computation and Bifurcation Analysis of Periodic Solutions of Large-Scale Systems, *IMA Preprint Series*, 1536(1998).

[24] Lust, K., Roose, D., Spence, A., Champneys, A.R., An Adaptive Newton-Picard Algorithm with Subspace Iteration for Computing Periodic Solutions, *SIAM J. Sci. Comp.*, to appear.

[25] Marcus, P.S., Simulation of Taylor-Couette flow. Part 1. Numerical methods and comparison with experiment, *J. Fluid Mech.*, 146(1984), pp. 45-64.

[26] Meshalkin, L.D., Sinai, I.G., Investigation of the Stability of a Stationary Solution of a System of Equations for the Plane Movement of an Incompressible Viscous Liquid, *PMM*, 25(6)(1961), pp. 1140-1143.

[27] Meyer-Spasche, R., Keller, H.B., Some bifurcation diagrams for Taylor vortex flows, *Phys. Fluids*, 28(5)(1985), pp. 1248-1252.

[28] Moulic, S.G., Yao, L.S., Taylor-Couette Instability of Travelling Waves with a Continuous Spectrum, *J. Fluid Mech.*, 324(1996), pp. 181-198.

[29] Platt, N., Sirovich, L., Fitzmaurice, N., An Investigation of Chaotic Kolmogorov Flows, *Phys. Fluid A*, 3(4)(1991), pp. 681-696.

[30] Schröder, W., Keller, H.B., Wavy Taylor-Vortex Flows via Multigrid-Continuation Methods, *J. Comp. Phys.*, 91(1990), pp. 197-227.

[31] She, Z.S., Large-Scale Dynamics and Transition to Turbulence in the Two-Dimensional Kolmogorov Flow, *Proc. on Current Trends in Turbulent Research*, AIAA (1998), pp. 374-396.

[32] Shroff, G.M., Keller, H.B., Stablilzation of Unstable Procedures: The Recursive Projection Method, *SIAM J. Numer. Anal.*, 30(4)(1993), pp. 1099-1120.

[33] Sivashinsky, G.I., Weak Turbulence in Periodic Flows, *Physica D*, 17(1985), pp. 243-255.

[34] Tuckerman, L.S., Barkley, D., Bifurcation Analysis For Timesteppers, *Preprint.*

[35] Van de Velde, E., Concurrent Scientific Computing, *Springer-Verlag*, 1994.

[36] Yakhot, V., Sivashinsky, G., Negative-Viscosity Phenomena in Three-Dimensional Flows, *Physical Review A*, 35(1987), pp. 815-820.